SOIL STRUCTURE INTERACTION IN POROELASTIC SOILS

by

Yousef Saleh Al Rjoub

A Dissertation Presented to the
FACULTY OF THE GRADUATE SCHOOL
UNIVERSITY OF SOUTHERN CALIFORNIA
In Partial Fulfillment of the
Requirements for the Degree
DOCTOR OF PHILOSOPHY
(CIVIL ENGINEERING)

May 2007

Acknowledgments

I am indebted to my advisor Prof. Maria Todorovska for her guidance and assistance through all the stages of this thesis work. I am also grateful to Prof. Mihailo Trifunac for the useful discussions and suggestions, and to my Ph.D. dissertation committee members: Prof. Vincent W. Lee, Prof. Hung Leung Wong and Prof. Frank Corsetti for their useful comments.

The financial support from the University of Southern California I received during the course of my studies in the form of Teaching Assistantship from the Civil Engineering Department, Research Assistantship from Prof. Maria Todorovska, and Dissertation Completion Fellowship from the Graduate School is gratefully appreciated.

Finally, I dedicate this work to my mother, the soul of my father, and my family, especially my brother Qasem, for their love and support during my study

Table of Contents

List of Tables

List of Figures

Abstract

This thesis presents an investigation of the effects of water saturation on the effective excitation and system response during building-foundation-soil interaction, using a simple theoretical model. The model consists of a shear wall supported by a rigid circular foundation embedded in a homogenous and isotropic poroelastic half-space. The half-space is fully saturated by a compressible and viscous fluid, and is excited by in-plane wave motion, consisting of plane P and SV waves, or of surface Rayleigh waves. Partial saturation is also considered but in a simplified way. The motion in the soil is described by Biot's theory of wave propagation in fluid saturated porous media. According to this theory, two P-waves (one fast and the other one slow) and one S-wave exist in the medium, which are represent by wave potentials. Helmholtz decomposition and wave function expansion are used to represent the motion in the soil, and a closed form solution of the problem is derived in the frequency domain. Numerical results are presented for the free-field motion, foundation input motion, complex foundation stiffness matrix, and the foundation and building response to incident plane fast P and SV waves, as function of the many model parameters. The presented analysis, which is linear, is of interest for understanding and interpreting the effects of water saturation on the response of the ground and structures to small amplitude (e.g. ambient noise) and to some degree earthquake excitation. An attempt is presented to use this model to explain the observed variation of the apparent frequencies of vibration of Millikan library in Pasadena, California, with heavy rainfall.

Chapter 1: Introduction

1.1 Objective and organization of this thesis

This thesis work presents an analysis of a simple linear model of building-foundation-soil interaction in poroelastic soil excited by in-plane excitation. The objective of this study is to gain insight into the effects of the water saturation on both the response of the soil and of the building and its foundation. Understanding of the effects of water saturation of soils on the seismic response of soils and structures is useful for interpreting observed and predicting the features of response of structures and soils to earthquake, ambient, and forced vibration excitation. It is noted here that, as the model is linear, it cannot represent true nonlinear response of soils and structures to strong earthquake shaking (e.g. soil yielding and liquefaction), but can be helpful in understanding the early smaller amplitude response leading to pore pressure buildup and nonlinear response.

The study is carried out using a simple two-dimensional (2D) model in which the soil is represented by a poroelastic half-space, and the structure is a shear wall supported by a cylindrical embedded foundation. Such a soil-structure interaction model has been considered first for semi-circular foundation embedded in elastic half-space and vertically incident SH waves by Luco (1969). This model was later generalized to obliquely incident SH waves by Trifunac (1972), to semi-elliptical foundations by Wong and Trifunac (1974), and to P, SV and Rayleigh wave excitation by Todorovska and Trifunac (1990) and Todorovska (1993a,b). Todorovska and Al Rjoub (2006a,b) considered such a model in which the seepage force was ignored, and the half-space was fully saturated. In this thesis work, the effects of the seepage force are included, and also of partial saturation, and the emphasis of the analysis is on how the seepage force and the degree of saturation affect the system response. Also, the free field motion is studied in grater detail.

The remaining part of this chapter presents literature review on wave propagation and soil-structure interaction in poroelastic soils. Chapter 2 presents the problem and method of solution. Chapter 3 presents numerical results for: (1) the wave velocities in the soil as function of soil permeability, relative stiffness of the skeleton, frequency and degree of saturation; (2) foundation complex stiffness matrix; (3) the free-field motion due to incident plane fast P and SV waves; (4) the foundation input motion; (5) the system response; and (6) shift of the apparent frequency of a model of the NS response of Millikan library in Pasadena, California, and comparison with its observed frequency shift during heavy rainfall and recovery days following the rainfall. Finally, Chapter 4 presents a summary and the conclusions.

1.2 Literature Review on Wave Propagation in Porous Media

The theory of wave propagation in a fully saturated poroelastic medium by a viscous compressible fluid was postulated by Maurice Biot in a series of papers (Biot, 1956a,b; 1962). While in elastic (one phase) medium two waves exist – one dilatational (P) and one rotational (S) wave, Biot's theory predicted the existence of an additional P-wave in a porielastic (two phase) medium, which is a result of the relative motion of the fluid with respect to the solid. This second P-wave, referred to as the "slow" P wave, is much slower and is much more attenuated and dispersed than the "true" P wave also referred to as the "fast" P wave. The existence of the slow P-wave was experimentally confirmed many years later, in the 1980s (Berrymann, 1980). The theory presented in Biot (1956a) is applicable to lower frequencies for which the flow of the fluid in the pores is Poiseuille. Biot (1956b) presents an extension of that theory to higher frequencies, beyond the critical frequency for which the Poiseuille assumption stops to be valid, but still small enough so that the related wavelengths are still much larger than the size of the pores. Biot (1962) presents an extension to anisotropic media, and media with solid dissipation, and other relaxation effects.

The remaining part of this section reviews literature on wave propagation in a homogeneous or layered poroelastic half-space for incident body and surface waves. This problem is of interest for the work in this thesis because wave motions in such a medium are usually used to represents the "free-field" seismic motions exciting structures on the ground surface or buried at some depth.

The effects of boundaries on wave propagation in fully saturated poroelastic media were studied by Deresiewicz and coworkers in the 1960s by considering plane body and surface waves incident onto a traction free poroelastic half-space. Deresiewicz (1960) considered incident P and SV waves onto a half-space saturated with a nondissipative liquid, Deresiewicz (1961) considered Love waves in a half-space saturated with a viscous liquid, and Deresiewicz and Rice (1962) considered incident plane P and SV waves onto a half-space saturated by a viscous fluid.

Incident plane body waves onto a half-space were considered also by other investigators, with emphasis on different applications (porous rock and soils). For example, Sharma and Gogna (1991) considered incident fast P-wave onto a half-space and showed results for water saturated sandstone. Lin *et al*. (2001, 2005) considered reflection of plane P and SV waves in water saturated porous half-space (assuming invicid fluid) for a wide range of skeleton stiffness, from very stiff (porous rock) to very soft (soft soil), for a range of values of Poisson's ratio and porosity, and for both drained and undrained hydraulic boundary condition on the half-space surface. They also discussed the range of validity of Biot's theory for different types of soils, and showed results for the amplitudes of the surface displacements, strains, rotations, and stresses, and examined the effect of the saturation, and various parameters of the mixture on these quantities. They found that, for undrained (sealed) half-space surface, the peak amplitudes of these characteristics of are smaller than the amplitudes for the elastic case. For a drained (open) half-space surface, they found that these peak amplitudes are smaller than for the elastic case, with the exception of the peak rotations. Ciarleta and Subatyan (2003) also studied the refection of plane waves in a fluid saturated poroelastic half-space but for the general case of a viscous fluid. Their study showed that the refection coefficients and the vibration amplitude in the saturated half-space are smaller than those in an elastic half-space.

Liu *et al.* (2002) studied stress wave propagation in transversely isotropic fluid-saturated porous medium for plane waves and for surface Rayleigh waves, in particular the effects of the fluid viscosity and the anisotropy of the solid skeleton. Their study showed that the fluid viscosity resulted in Rayleigh waves with frequency dependent phase velocity.

Degrande *et al.* (1998) studied harmonic and transient wave propagation in multi-layered dry, saturated and *unsaturated* isotropic poroelastic media, but for small fraction of gas in the fluid and ignoring the effects of the capillary forces. They examined the effect of moving ground water table and partial saturation on wave propagation in a poroelastic layered half-space, and found that air bubbles in the top layer of a saturated half-space affect the P-wave propagation. Partial saturation was considered in a similar way by Yang (2000, 2001, 2002) and Yang and Sato (2000a,b) for incident plane waves in a poroelastic half-space and onto a boundary between two bonded half-spaces, the lower one being elastic and the upper one being *partially* saturated poroelastic. Further, Yang and Sato (2000c) showed that partial saturation in the soil near the surface may explain the significant amplification of the vertical motion observed by a borehole array at Port Island, Kobe, during the 1995 Hyogo-Ken Nanbu (Kobe) earthquake, while the opposite effect was observed for the horizontal motions. In their earlier work, the same authors studied the effects of the flow condition and viscous coupling (i.e. the effect of the seepage force) on reflection of waves from an interface between two half-spaces, the lower one being elastic and the upper one being *fully* saturated poroelastic (Yung and Sato, 1998; Yang, 1999).

In contrast to the previously mentioned work dealing with partial saturation, which used a modified theory for a two phase medium, Carcione *et al.* (2004) simulated wave propagation in partially saturated porous rock *including capillarity pressure effects*. Their model is based on a Biot type theory for a three-phase medium, which predicted the existence of a second slow wave.

Other recent work on wave propagation in fluid saturated poroelastic media includes that of: Liu and Liu (2004), who analyzed the propagation of Rayleigh waves in orthotropic fluid-saturated porous media; Sharma (2004), who studied the propagation of plane harmonic waves in an anisotropic fluid-saturated porous solid; Vashishth and Khurana (2004), who studied the wave propagation in a multilayered anisotropic poroelastic medium; Jinting *et al.* (2004), who studied the refection and refraction of waves in a multi-layered medium composed of ideal fluid, porous medium, and underlying elastic solid, and subjected to incident P wave. Other recent work also includes Edelman (2004a,b), who studied the existence of surface waves along the interface between vacuum and porous medium in the low frequency range. Finally, Liu *et al.* (2005) used the generalized characteristic theory to analyze the stress wave propagation in anisotropic, in particular orthotropic, fluid-saturated porous media.

1.3 Literature Review on Soil Structure Interaction in Porous Media

This section presents a literature review of soil-structure interaction in poroelastic soils. Review of other work on this topic that does not involve poroelasticity is out of the scope of this thesis.

Halpern and Christiano (1986) present compliance matrices for *vertical* and *rocking* motion of a square rigid plate baring on a water-saturated poroelastic half-space for water saturated coarse grained sands (with porosity 0.48, and shear modulus of the skeleton 20 times smaller than the bulk modulus of water). Their results indicate smaller (in absolute value) real and imaginary parts of the compliance (i.e. stiffer soil) for saturated soil as compared to dry soils for both vertical and rocking motions. They also studied the stress distribution along the contact surface carried separately by the solid and by the fluid, and concluded that the magnitude of either one of the component stresses can be grater than the total stress predicted by an equivalent undrained elastic solid model (elastic solid with Poisson ratio 0.5).

Kassir and Xu (1988) studied interaction of a rigid pervious strip foundation bonded to a poroelastic half-space for *horizontal*, *vertical*, and *rocking* motions. They concluded that the influence of the fluid is substantial, and is more pronounced for vertical and rocking motions. Kassir et al. (1989) studied impedances for *vertical* motion of circular footings on a poroelstic half-space. They concluded that, for dense sand, the presence of ground water affects the magnitude and character of the influence functions and should be included in dynamic analysis of surface structures to dynamic loading.

Philippacopoulos (1989) present dynamic stiffness for vertical motion of a rigid disk foundation on a layered poroelastic half-space saturated up to certain depth below the disk. He concludes "the effect due to saturation on the impedance function is generally not significant. Specifically, at low dimensionless frequency (i.e. less than 3) this effect is practically negligible, while at higher dimensionless frequency (i.e. between 3 and 6), the departure from the dry case was about 30%." In the discussion of his results, he states, "the effect of the pore fluid is to generally reduce the stiffness and increase the damping (compared to the dry case). Furthermore, these effects are more pronounced at higher dimensionless frequency and at lower saturation depth-to radius ratio. On the other hand, at low frequencies, the results from both saturated and dry cases agree very well."

This was explained by the fact that “the water has sufficient time to drain and thus avoids carrying stresses imposed by the skeleton.” It is not clear from the discussion to what degree the predicted effects are due to the “layer” effect created by the impedance contrast at the water table level at depth, as compared to the fluid motion.

Bougacha and Tassoulas (1991a,b) developed a finite element technique to solve the dynamic response of a gravity dam. The sediment is modeled as two-phase medium. It is found that the partially saturated sediment leads to a significant decrease in the system fundamental frequency more than fully saturated sediment.

Bougacha et al. (1993a,b) present a computational model and results for dynamic stiffnesses for rigid strip and circular foundations on fluid filled poroelastic stratum over a rigid base for *horizontal*, *vertical*, *rocking* and *torsional* motion, and propose how to estimate the equivalent properties of an elastic soil. They show results for porosity 0.3, Poisson ratio 1/3, and shear modulus of the skeleton such that it results in shear wave velocity of 152 m/s. For torsional loading, they state that the results for a circular disk obtained for the two-phase medium and the equivalent solid are identical, and explain that by the fact that the torsional loading for circular footings transmits only shear waves into the stratum. They conclude that the seepage forces introduce substantial damping at low frequencies in the case of vertical excitation, while their effect on the rocking, and especially on the torsional stiffness and damping coefficients were relatively minor.

Rajapakse and Senjuntichai (1995) present a soil-structure interaction model for rigid strip foundation on a layered half-space, and show results for foundation response to unit vertical and horizontal loads, and vertical impedance for a layered model. They also show results for the pore pressure distribution with depth.

Kassir *et al*. (1996) present the impedances of surface circular footing on a poroelastic half-space, for *rocking* and *horizontal* motions. They conclude that for rocking motion, the presence of pore fluid significantly affects the impedance (both in magnitude and sign), while the influence is marginal for horizontal motion.

Dargush and Chopra (1996) consider circular footings on a half-space or a layer over bedrock, for *horizontal*, *vertical*, *rocking* and *torsional* motion. Their results show that for surface footing on half-space, and for vertical motions, the compliance is larger for dry soil than for poroelastic saturated soil, but the difference is small for small frequencies and high permeability. For low permeability, the compliance is similar for poroelastic and for undrained solid. For surface footing on layered medium, they note a significant influence of the soil layer resonance.

Japon *et al*. (1997) show probably the most comprehensive set of results that shed light on the effects of the pore water on the foundation stiffness for surface foundations. They show impedances for strip foundations resting on a half-space, or on a stratum over rigid or compliant bedrock, for smooth or welded contact, and for *horizontal*, *vertical*, and *rocking* motions. Their results show that the seepage forces stiffen the foundation and increase the damping. For a half-space soil model, their results show that the type of contact condition is only important for the real part of *vertical* stiffness, which is larger for a welded contact and for an impervious foundation. Further, the seepage forces produce an effect of increased stiffness for the whole range of frequencies, and their effect is more pronounced on the imaginary part (i.e. the radiation damping). The added density (from the coupling mass term) produces increase in stiffness, noticeable only when there are no seepage forces. For soil represented as a layer, the *vertical* and *rocking* stiffness tend to the half-space values as the layer depth grows. At smaller frequencies, the foundation stiffness for a layer is larger than that for a half-space, but the difference is small for depth of layer to half width of foundation > 4. Further, the foundation stiffness for a layer is oscillatory about the half-space solution, with increasing frequency and decreasing amplitudes of the oscillations as the depth of layer increases. For vertical motions, the oscillations are related to resonance of the fast P waves in the layer, while for horizontal motions – to the resonance of the SH waves in the layer. Further, they show that the effect of the seepage forces is much more important for a stratum than for half-space, and finally, that the position of the resonant peaks may change substantially with the dissipation coefficient *b*.

Zeng and Rajapakse (1999) studied *vertica*l vibrations of a circular disk on a half-space, and noted an increase in stiffness and radiation damping due to the poroelastic effects.

Bo and Hua (1999) present compliances for a circular rigid disk on a half-space for *vertical* motions. They conclude that the difference in compliance between pervious and impervious foundation decreases with increasing seepage forces. Similarly, Jin and Liu (2000a,b) show such compliances for *horizontal* and for *rocking* motions. For the *horizontal* motions, they conclude that the permeability of the medium has an important effect on horizontal vibrations, and that there is a difference between the compliances for elastic and for saturated half-space. The conclusion for the *rocking* motions is that the difference in compliance between poroelasic and elastic half-space is < 18% and can be neglected. However, these three studies show results for a very limited set of parameters.

Senjuntichai *et al*. (2006) show impedances for axi-symmetric *embedded* foundations in a half-space for *vertical* motions. They study the effects of foundation depth, soil permeability, and foundation shape. Their results show that for cylindrical shape, both the stiffness and the damping increase with increasing foundation depth. Further, there is a notable dependence of the foundation stiffness on the hydraulic boundary condition especially at higher frequencies and for short cylinders, but this effect is much smaller for smaller permeability.

Chapter 2: Theoretical Model

2.1 The Soil-Structure Interaction Model

The simple two-dimensional soil-structure interaction model is shown in Fig. 2.1.1. The structure is represented as a shear beam supported by a circular rigid foundation embedded in a homogeneous and isotropic *poroelastic* half-space. The center of curvature of the foundation is at some point O_1 along the *z*-axis, in general above point O. The shear beam has height *H*, width *W*, and mass per unit length m_{b}. The foundation has width 2*a*, depth *h*, and mass per unit length m_{fnd}. The response of the foundation is described by the horizontal and vertical displacements of point O, Δ and V, and the rotation angle φ (positive clockwise). The building moves as a rigid body, with translations Δ and V, and rotation φ, and also deflects due to elastic deformation (Fig. 2.1.1). The horizontal displacement at the top of the building due to its elastic deformation is $u_{\mathrm{b}}^{\mathrm{rel}}$. The shear wave velocity in the building is $V_{S,\mathrm{b}}$, which implies first mode fixed-base frequency $f_1 = V_{S,\mathrm{b}}/(4H)$. The damping in the building is neglected.

The motion in the half-space is described by the linearized theory of wave propagation in fluid saturated poroelastic media as described by Biot (1956a). The two-phase medium is composed of a solid skeleton, formed by the grains, and fluid occupying completely all voids in the skeleton. The properties of this mixture are defined by the shear modulus and Poisson's ratio of the skeleton μ_{s} and ν_s, the bulk modulus of the fluid K_f, the porosity $\hat{n}$, the mass density of the grains ρ_{gr} comprising the skeleton, and the density of the fluid ρ_{f}, both defined per unit volume of pure grain material and pure

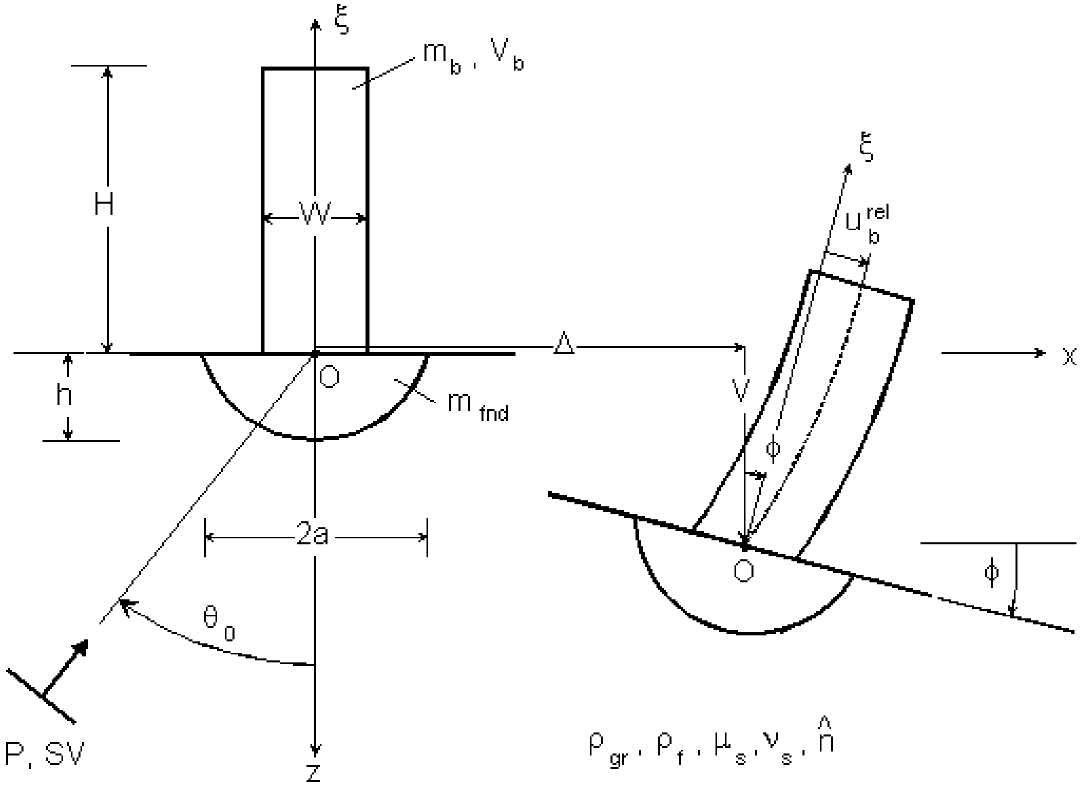

Fig. 2.1.1 The model

fluid. This implies shear wave velocity of the dry mixture $V_{S,\mathrm{dry}} = \sqrt{\mu_s / [(1-\hat{n})\rho_{\mathrm{gr}}]}$. The skeleton and the foundation are perfectly bonded to each other. The motion of the fluid along the contact surface relative to that of the solid is constrained by the drainage condition. It is assumed in this thesis work that the foundation can be either completely permeable, allowing for free drainage of the pore fluid, or completely impermeable. These conditions would affect the foundation complex stiffness matrix, and the foundation driving forces. The half-space surface can also be either perfectly sealed or unsealed, and this would affect the free-field motion (Lin et al., 2001, 2005).

A closed form solution is obtained by: (1) expanding the scattered waves (a perturbation to the free-field motion caused by the presence of the foundation) in a series of outgoing cylindrical waves (represented by Hankel functions in space), (2) expressing the coefficients of this expansion in terms of the (known) coefficients of expansion of the free-field motion and the (unknown) motion of the rigid foundation through the continuity of displacements at the contact surface, and (3) solving for the motion of the foundation from the dynamic equilibrium conditions. In this process, the zero-stress condition on the half-space surface, which is automatically satisfied by the free-field motion, is relaxed for the scattered waves, as in Todorovska and Al Rjoub (2006a). The zero stress condition for the scattered waves can be imposed numerically along finite length of the half-space surface adjacent to the foundation, by some point collocation or a weighted residual method, for example. In the interest of simplicity, and in view of all the other simplifications in this model (e.g., the restriction of the shape of the foundation, the assumption that it is absolutely rigid, the assumption of perfect bond at the contact surface, and finally – the assumption of liner constitutive relations and small displacements, and of homogeneous and isotropic soil), it was decided to relax this condition. De Barros and Luco (1995) compared foundation impedances for a semi-circular foundation in an elastic half-space, when the zero-stress boundary condition is imposed on the scattered waves, and when it is relaxed. Their results show that for horizontal and vertical motions the difference is small (the approximate solution overestimates slightly the damping and the vertical stiffness, while it underestimated slightly the horizontal stiffness at smaller frequencies and overestimates it slightly for higher frequencies). The difference is also small for the coupling terms (between horizontal motion and rocking). The difference is the largest for the rocking motions at low frequencies, especially for the damping coefficient. The approximate solution overestimates the rocking stiffness and underestimates the damping at all frequencies in the range $a_0 = \omega a / V_S < 5$, but the difference becomes progressively smaller as the frequency increases. At $a_0 = 0.5$, the rocking stiffness is overestimated by as much as about 28%, and the damping coefficient is underestimated by as much as 38%, but the shapes of the functions are similar, and the difference rapidly decreases with frequency, especially for the damping coefficient. However, it turns out that the rocking stiffness is not noticeably affected by the fluid in the pores, as shown in the companion paper, and therefore the conclusions of this study are not likely to be affected by this approximation.

2.2 Wave Propagation in Fluid Saturated Poroelastic Medium

The motion in the soil is assumed to be governed by Biot's theory of wave propagation in a fully saturated poroelastic medium (1956a), which was postulated based on the assumption that the motion of the solid matrix is a wave motion, while that of the fluid relative to the solid is a diffusion process described by Darcy's law. Biot (1956a) made the following assumptions:

1. The Reynolds number is less than 2000, which implies that the relative motion of the fluid in the pores is laminar flow.
2. The size of the unit element of the solid-fluid mixture is much smaller than the wavelength of the motions considered.
3. The size of the unit element of the mixture is large compared to the size of the pores.

Then the motion of the solid and that of the fluid is described by the following two coupled equations of motion

$$
\begin{aligned}
&\mu\nabla^2\tilde{u} + \text{grad}\left[\left(\lambda+\mu\right)e + Q\varepsilon\right] = \frac{\partial^2}{\partial t^2}\left(\rho_{11}\tilde{u} + \rho_{12}\tilde{U}\right) + \hat{b}\frac{\partial}{\partial t}\left(\tilde{u} - \tilde{U}\right) \\
&\text{grad}\left[Qe + R\varepsilon\right] = \frac{\partial^2}{\partial t^2}\left(\rho_{11}\tilde{u} + \rho_{12}\tilde{U}\right) - \hat{b}\frac{\partial}{\partial t}\left(\tilde{u} - \tilde{U}\right)
\end{aligned}
\tag{2.2.1}
$$

where

$\tilde{u}$ = displacement vector for the solid-skeleton

$\tilde{U}$ = displacement vector for the pore fluid

$e = div\left(\tilde{u}\right)$

$\varepsilon = div\left(\tilde{U}\right)$

$\rho_{11}, \rho_{12}, \rho_{22}$ = dynamic mass coefficients

$\hat{b}$ = coefficient of dissipation

The coefficient of dissipation $\hat{b}$ depends on the permeability of the skeleton and on the viscosity of the fluid via the relation

$$\hat{b} = \hat{n}^2 \frac{\hat{\mu}}{\hat{k}}$$

where

$\hat{n}$ = porosity

$\hat{\mu}$ = absolute viscosity in units $\mathrm{Pa \cdot s = kg/(m \cdot s)}$

$\hat{k}$ = intrinsic permeability (depends only on the properties of the skeleton) in units m^2

Hence, $\hat{b} / \omega$ has units of mass density.

Helmholtz decomposition to the displacement vector gives

$$\tilde{u} = \mathrm{grad}\left(\phi\right) + \mathrm{curl}\left(\tilde{\psi}\right) \tag{2.2.2a}$$

$$\tilde{U} = \mathrm{grad}\left(\Phi\right) + \mathrm{curl}\left(\tilde{\Psi}\right) \tag{2.2.2b}$$

where ϕ and Φ are the P-wave potentials, and ψ and Ψ are the S-wave potentials for the solid and fluid, respectively. Substitution of eqns (2.2.2a,b) into eqn (2.2.1) leads to the following two sets of equations for the P-wave and S-wave potentials

$$P\nabla^2\phi + Q\nabla^2\Phi = \frac{\partial^2}{\partial t^2}\left(\rho_{11}\phi + \rho_{12}\Phi\right) + \hat{b}\frac{\partial}{\partial t}\left(\phi - \Phi\right)$$
$$Q\nabla^2\phi + R\nabla^2\Phi = \frac{\partial^2}{\partial t^2}\left(\rho_{11}\phi + \rho_{12}\Phi\right) - \hat{b}\frac{\partial}{\partial t}\left(\phi - \Phi\right) \qquad (2.2.3)$$

and

$$\mu\nabla^2\tilde{\psi} = \frac{\partial^2}{\partial t^2}\left(\rho_{11}\tilde{\psi} + \rho_{12}\tilde{\Psi}\right) + \hat{b}\frac{\partial}{\partial t}\left(\tilde{\psi} - \tilde{\Psi}\right)$$
$$0 = \frac{\partial^2}{\partial t^2}\left(\rho_{11}\tilde{\psi} + \rho_{12}\tilde{\Psi}\right) - \hat{b}\frac{\partial}{\partial t}\left(\tilde{\psi} - \tilde{\Psi}\right) \qquad (2.2.4)$$

2.3 Solution for P-waves

For harmonic wave motion, the potentials can be represented as

$$\phi = c_1 e^{i(kx+\omega t)}, \ \Phi = c_2 e^{i(kx+\omega t)} \qquad (2.2.5)$$

$$\psi = c_3 e^{i(kx+\omega t)}, \ \Psi = c_4 e^{i(kx+\omega t)} \qquad (2.2.6)$$

Substitution of eqn (2.2.5) into eqn (2.2.3) leads to the following fourth order differential equation for the P-wave potential in the solid

$$A\phi^4 - B\phi^2 + C = 0 \qquad (2.2.7a)$$

where

$$A = PR - Q^2 \qquad (2.2.7b)$$

$$B = \rho_{11}R + \rho_{22}P - 2\rho_{12}Q - \frac{ib}{\omega}(P + R + 2Q) \qquad (2.2.7c)$$

$$C = \rho_{11}\rho_{22} - \rho_{12}^2 - \frac{ib}{\omega}(\rho_{11} + \rho_{22} + 2\rho_{12}) \qquad (2.2.7d)$$

Further, eqn (2.2.7) can be decomposed into the following two equations

$$\left(\nabla^2 + k_{\alpha,j}^2\right)\phi_j = 0, \quad j=1,2 \qquad (2.2.8)$$

where

$$k_{\alpha,j} = \frac{\omega}{V_{\alpha,j}} \quad ,j\text{=}1,2 \tag{2.2.9a}$$

and

$$V_{\alpha,j} = \sqrt{\frac{2A}{B \mp \left(B^2 - 4AC\right)^{1/2}}} \quad , \quad j\text{=}1,2 \tag{2.2.9b}$$

are the wave numbers and wave velocities of two distinct P-waves (fast and slow) in the solid.

The wave potential for the fluid can be obtained after substituting eqn (2.2.5) into eqn (2.2.3), which gives

$$\Phi = \Phi_1 + \Phi_2 = f_1\phi_1 + f_2\phi_2 \tag{2.2.10}$$

where

$$f_j = \frac{A/V_{\alpha,j}^2 - \rho_{11}R + \rho_{12}Q + (ib/\omega)(Q+R)}{\rho_{12}R - \rho_{22}Q + (ib/\omega)(Q+R)} \quad , \quad j\text{=}1,2 \tag{2.2.11}$$

2.3.1 Solutions for S-waves

Substitutin of eqn (2.2.6) into eqn (2.2.2) leads to the following differential equation for the S-wave potential of the motion of the skeleton

$$\left(\nabla^2 + k_\beta^2\right)\psi = 0 \tag{2.2.12}$$

where

$$k_\beta = \frac{\omega}{V_\beta} \tag{2.2.13a}$$

and

$$V_\beta = \sqrt{\frac{\mu(\rho_{22} - ib/\omega)}{\rho_{11}\rho_{22} - \rho_{12}^2 - (\rho_{11} + \rho_{22} + 2\rho_{12}) * ib/\omega}} \tag{2.2.13b}$$

are the wave number and wave velocity of the shear waves in the skeleton.

The wave potential for the fluid can be obtained as

$$\Psi = f_3\psi \tag{2.2.14}$$

where

$$f_3 = -\frac{(\rho_{12} + ib/\omega)}{(\rho_{22} - ib/\omega)} \tag{2.2.15}$$

2.3.2 Material Constants for the Mixture

The material constants of mixtures can be determined experimentally (Biot and Willis, 1957), or can be derived from the properties of the components. In the dimensionless analysis in this work, the set of input parameters consists of the porosity $\hat{n}$, the Poisson's ratio of the skeleton ν_s, the ratio of the bulk modulus of the fluid and the shear modulus of the skeleton K_f / μ_s, and the ratio of the mass density of the fluid and that of the grains ρ_f / ρ_{gr} (both per unit volume of "pure" material).

The elastic moduli of the mixture μ, λ, R and Q are computed using a simplification (for R and Q) of the formulae proposed by Biot and Willis (1957) based on the assumption that the compressibility of the mixture is much smaller than that of the solid skeleton and of the fluid, and can be neglected, which is a common assumption in soil mechanics (Lin et al., 2005)

$$
\begin{aligned}
&\mu = \mu_s \\
&\lambda = \lambda_s + Q^2 / R \\
&Q = (1-\hat{n}) K_f \\
&R = \hat{n} K_f
\end{aligned}
\tag{2.2.16}
$$

where

$\lambda_s = \dfrac{2v_s}{1-2v_s}\mu_s$ = Lamé constant for the skeleton

For computation of the mass coefficients, ρ_{11}, ρ_{22} and ρ_{12}, the following relations proposed by Berryman (1980) are used (as in Lin et al., 2005)

$$
\begin{aligned}
&\rho_{11} = (1-\hat{n})\rho_{\mathrm{gr}} - \rho_{12} \\
&\rho_{22} = \hat{n}\rho_{\mathrm{f}} - \rho_{12} \\
&\rho_{12} = -\hat{n}(\tau_\alpha - 1)\rho_{\mathrm{f}}
\end{aligned}
\tag{2.2.17}
$$

where

$$\tau_\alpha = 1 + \tau_r \frac{1-\hat{n}}{\hat{n}} \geq 1 = \text{ dynamic tortuosity} \tag{2.2.18a}$$

Tortuosity is a dimensionless macroscopic parameter characterizing the resistance to flow of a fluid in porous medium, in particular the effect that, on microscopic scale, the paths of the fluid particles deviate from a straight line. It depends on the porosity, $\hat{n}$, as well as on the shape of the pores, through the parameter τ_r. It has values $1 \leq \tau_\alpha < \infty$. As $\hat{n} \to 1$ (pure fluid) $\tau_\alpha \to 1$, and as $\hat{n} \to 0$ (pure solid) $\tau_\alpha \to \infty$. For pores formed by spherical grains, as assumed in this work, $\tau_r = 1/2$, and

$$\tau_\alpha = \frac{1}{2}\left(1+\frac{1}{\hat{n}}\right) \tag{2.2.18b}$$

It can be seen from eqn (2.2.17) that the dynamic mass coefficients represent physically mass densities, per unit volume of the mixture. If the coupling term ρ_{12} is neglected, then ρ_{11} and ρ_{22} represent the mass densities of the solid and fluid phases per unit volume of the mixture.

2.3.3 Approximate Treatment of Partial Saturation

Partially saturated soil represents a three-phase medium (mixture of solid, fluid and gas). So far there is no generally accepted theory for wave propagation in such soil medium. In this work, a simplified approach is followed, in which is the theory for a two-phase medium is used, but with reduced bulk modulus of the fluid, as in Yang (2001). Let S_r be the degree of saturation. The relative proportions of the constituent volumes are defined as

$$\hat{n} = V_V / V_t \tag{2.2.19a}$$

$$S_r = V_W / V_V \tag{2.2.19b}$$

where $\hat{n}$ is the porosity of the soil, and V_V, V_W and V_t are respectively the volumes of pores, pore water and the total volume.

In this study, a high degree of saturation is considered > 90%, assuming the embedded air in the pore water is in the form of bubbles uniformly distributed through the fluid. In this case, the bulk modulus of fluid K_f can be written as

$$K_f = \frac{1}{\frac{1}{K_W} + \frac{1 - S_r}{P_a}} \tag{2.2.20}$$

Where K_W is the bulk modulus of pore water and P_a is the absolute fluid pressure.

2.4 The Soil-Structure Interaction Problem

2.4.1 Representation of the Scattered Waves

The scattered waves are represented by a triplet of potentials, ϕ_1^R, ϕ_2^R, and ψ^R, each expanded in Fourier-Bessel series with period 2π, representing outgoing cylindrical waves with origin at point O_1 (see Fig. 2.3.1 showing an excavation in the soil where the foundation is embedded)

$$\begin{aligned}
\phi_1^R &= \sum_{n=0}^{\infty}(A_{1,n}\cos n\theta_1 + B_{1,n}\sin n\theta_1)H_n^{(1)}(k_{P1}r_1)\, e^{-i\omega t} \\
\phi_2^R &= \sum_{n=0}^{\infty}(E_{1,n}\cos n\theta_1 + F_{1,n}\sin n\theta_1)H_n^{(1)}(k_{P2}r_1)\, e^{-i\omega t} \\
\psi^R &= \sum_{n=0}^{\infty}(C_{1,n}\sin n\theta_1 + D_{1,n}\cos n\theta_1)H_n^{(1)}(k_S r_1)\, e^{-i\omega t}
\end{aligned} \tag{2.3.1}$$

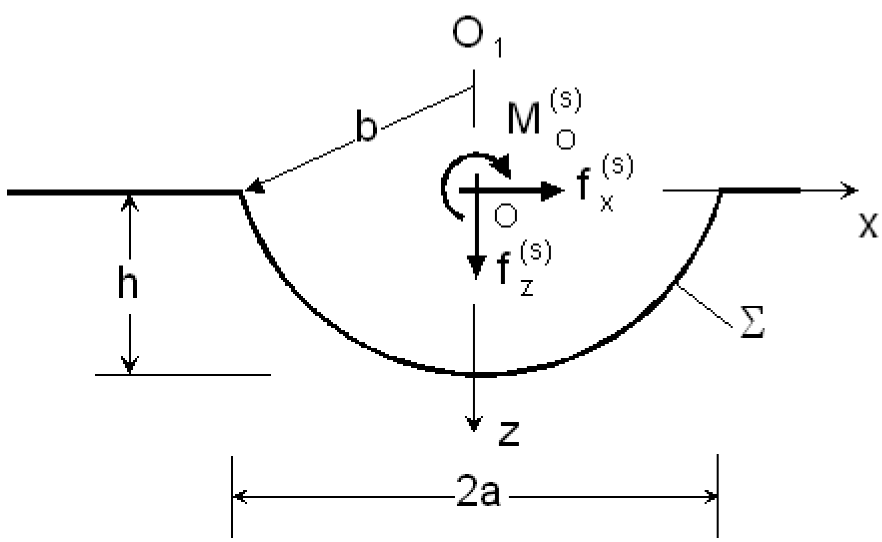

Fig. 2.4.1 The excavation and forces acting on the soil.

The radial and tangential components of the displacements of the skeleton due to these waves are

$$\begin{Bmatrix} u_{r_1} \\ u_{\theta_1} \end{Bmatrix}^R (r_1,\theta_1) = \left\{ \sum_{n=0}^{\infty} \frac{1}{r_1} \begin{bmatrix} D_{11}^{(3)} \cos n\theta_1 & D_{12}^{(3)} \cos n\theta_1 & D_{13}^{(3)+} \cos n\theta_1 \\ D_{21}^{(3)+} \sin n\theta_1 & D_{22}^{(3)+} \sin n\theta_1 & D_{23}^{(3)} \sin n\theta_1 \end{bmatrix} \begin{Bmatrix} A_{1,n} \\ E_{1,n} \\ C_{1,n} \end{Bmatrix} \right.$$
$$\left. + \frac{1}{r_1} \begin{bmatrix} D_{11}^{(3)} \sin n\theta_1 & D_{12}^{(3)} \sin n\theta_1 & D_{13}^{(3)-} \sin n\theta_1 \\ D_{21}^{(3)-} \cos n\theta_1 & D_{22}^{(3)-} \cos n\theta_1 & D_{23}^{(3)} \cos n\theta_1 \end{bmatrix} \begin{Bmatrix} B_{1,n} \\ F_{1,n} \\ D_{1,n} \end{Bmatrix} \right\} e^{-i\omega t} \tag{2.3.2a}$$

and the same components of the displacement of the fluid are

$$\begin{Bmatrix} U_{r_1} \\ U_{\theta_1} \end{Bmatrix}^R (r_1,\theta_1) = \left\{ \sum_{n=0}^{\infty} \frac{1}{r_1} \begin{bmatrix} D_{11}^{(f,3)} \cos n\theta_1 & D_{12}^{(f,3)} \cos n\theta_1 & D_{13}^{(f,3)+} \cos n\theta_1 \\ D_{21}^{(f,3)+} \sin n\theta_1 & D_{22}^{(f,3)+} \sin n\theta_1 & D_{23}^{(f,3)} \sin n\theta_1 \end{bmatrix} \begin{Bmatrix} A_{1,n} \\ E_{1,n} \\ C_{1,n} \end{Bmatrix} \right.$$
$$\left. + \frac{1}{r_1} \begin{bmatrix} D_{11}^{(f,3)} \sin n\theta_1 & D_{12}^{(f,3)} \sin n\theta_1 & D_{13}^{(f,3)-} \sin n\theta_1 \\ D_{21}^{(f,3)-} \cos n\theta_1 & D_{22}^{(f,3)-} \cos n\theta_1 & D_{23}^{(f,3)} \cos n\theta_1 \end{bmatrix} \begin{Bmatrix} B_{1,n} \\ F_{1,n} \\ D_{1,n} \end{Bmatrix} \right\} e^{-i\omega t} \tag{2.3.2b}$$

The radial and tangential components of the stresses in the skeleton due to these waves are

$$\begin{Bmatrix} \tau_{r_1 r_1} \\ \tau_{r_1 \theta_1} \end{Bmatrix}^R (r_1,\theta_1) = \frac{2\mu}{r_1^2} \left\{ \sum_{n=0}^{\infty} \begin{bmatrix} E_{11}^{(3)} \cos n\theta_1 & E_{12}^{(3)} \cos n\theta_1 & E_{13}^{(3)+} \cos n\theta_1 \\ E_{21}^{(3)+} \sin n\theta_1 & E_{22}^{(3)+} \sin n\theta_1 & E_{23}^{(3)} \sin n\theta_1 \end{bmatrix} \begin{Bmatrix} A_{1,n} \\ E_{1,n} \\ C_{1,n} \end{Bmatrix} \right.$$
$$\left. + \begin{bmatrix} E_{11}^{(3)} \sin n\theta_1 & E_{11}^{(3)} \sin n\theta_1 & E_{13}^{(3)-} \sin n\theta_1 \\ E_{21}^{(3)-} \cos n\theta_1 & E_{22}^{(3)-} \cos n\theta_1 & E_{23}^{(3)} \cos n\theta_1 \end{bmatrix} \begin{Bmatrix} B_{1,n} \\ F_{1,n} \\ D_{1,n} \end{Bmatrix} \right\} e^{-i\omega t} \tag{2.3.3a}$$

and the stress in the fluid is

$$s^R\left(r_1,\theta_1\right)=\sum_{n=0}^{\infty}\left[E_1^{(f,3)}\cos n\theta_1 \quad E_2^{(f,3)}\cos n\theta_1\right]\begin{Bmatrix}A_{1,n}\\E_{1,n}\end{Bmatrix}$$
$$\left.+\left[E_1^{(f,3)}\sin n\theta_1 \quad E_2^{(f,3)}\sin n\theta_1\right]\begin{Bmatrix}B_{1,n}\\F_{1,n}\end{Bmatrix}\right\}e^{-i\omega t} \qquad (2.3.3b)$$

where

$$\begin{aligned}
D_{11}^{(l)}\left(r\right)&=-nC_n(k_{P1}r)+k_{P1}rC_{n-1}(k_{P1}r)\\
D_{12}^{(l)}\left(r\right)&=-nC_n(k_{P2}r)+k_{P2}rC_{n-1}(k_{P2}r)\\
D_{13}^{(l)\pm}\left(r\right)&=\pm nC_n(k_S r)\\
D_{21}^{(l)\pm}\left(r\right)&=\mp nC_n(k_{P1}r)\\
D_{22}^{(l)\pm}\left(r\right)&=\mp nC_n(k_{P2}r)\\
D_{23}^{(l)}\left(r\right)&=nC_n(k_S r)-k_\beta rC_{n-1}(k_S r)
\end{aligned} \qquad (2.3.4a)$$

$$D_{ij}^{(f,l)}\left(r\right)=f_j D_{ij}^{(l)}\left(r\right),\quad i=1,2;i=1,2,3 \qquad (2.3.4b)$$

$$C_n(\cdot)=\begin{cases}J_n(\cdot), & l=1\\ Y_n(\cdot), & l=2\\ H_n^{(1)}(\cdot), & l=3\\ H_n^{(2)}(\cdot), & l=4\end{cases} \qquad (2.3.5)$$

$J_n(\cdot)$ and $Y_n(\cdot)$ are the Bessel functions of first and second kind, and $H_n^{(1)}(\cdot)$ and $H_n^{(2)}(\cdot)$ are the Hankel functions of the first and second kind, and f_j is as defined in eqn (2.2.1).

$$
\begin{aligned}
E_{11}^{(l)}(r) &= \left[n^2 + n - \frac{1}{2}(k_{P1}r)^2 \right] C_n(k_{P1}r) - \frac{1}{2}(k_f r)^2 \left(1 + \frac{\lambda}{2} + Q \right) C_n(k_f r) - k_{P1} r C_{n-1}(k_{P1}r) \\
E_{12}^{(l)}(r) &= \left[n^2 + n - \frac{1}{2}(k_{P2}r)^2 \right] C_n(k_{P2}r) - \frac{1}{2}(k_{P2}r)^2 \left(1 + \frac{\lambda}{2} + Q \right) C_n(k_{P2}r) - k_{P2} r C_{n-1}(k_{P2}r) \\
E_{13}^{(l)\pm}(r) &= \mp n\left[-(n+1)C_n(k_S r) + k_S r C_{n-1}(k_\beta r) \right] \\
E_{21}^{(l)\pm}(r) &= \mp n\left[-(n+1)C_n(k_{P1}r) + k_{P1} r C_{n-1}(k_{P1}r) \right] \\
E_{22}^{(l)\pm}(r) &= \mp n\left[-(n+1)C_n(k_{P2}r) + k_{P2} r C_{n-1}(k_{P2}r) \right] \\
E_{23}^{(l)}(r) &= -\left[n^2 + n - \frac{1}{2}(k_S r)^2 \right] C_n(k_S r) - k_S r C_{n-1}(k_S r)
\end{aligned}
\tag{2.3.6a}
$$

$$
\begin{aligned}
E_{11}^{(f,l)}(r) &= \frac{1}{2} S_1 (k_{P1}r)^2 C_n(k_{P1}r) \\
E_{12}^{(f,l)}(r) &= \frac{1}{2} S_2 (k_{P2}r)^2 C_n(k_{P2}r) \\
E_{13}^{(f,l)}(r) &= 0
\end{aligned}
\tag{2.3.6b}
$$

where

$$
S_j = \left(Q + f_j R \right) / \mu, \quad j = 1,2 \tag{2.3.7}
$$

2.4.2 Boundary Conditions at the Contact Surface

The motion of the rigid foundation for incident monochromatic waves is harmonic, and can be written as

$$
\begin{Bmatrix} V \\ \Delta \\ \varphi a \end{Bmatrix} = \begin{Bmatrix} V_0 \\ \Delta_0 \\ \varphi_0 a \end{Bmatrix} \mathrm{e}^{-i\omega t} \tag{2.3.8}
$$

Along the contact surface Σ: $r_1 = b, -\theta_0 \le \theta \le \theta_0$, $\theta_0 = \sin^{-1}(a/b)$ (Fig. 2.3.1), the displacements of the skeleton are constrained by the displacements of the foundation, and the motion of the fluid is constrained by the drainage condition. Perfect bond between the skeleton and the foundation, and perfectly sealed contact (i.e. no drainage of the pore fluid) imply

$$\begin{Bmatrix} u_{r_1} \\ u_{\theta_1} \\ \left(u_{r_1} - U_{r_1}\right) \end{Bmatrix}_{\Sigma}^{ff} + \begin{Bmatrix} u_{r_1} \\ u_{\theta_1} \\ \left(u_{r_1} - U_{r_1}\right) \end{Bmatrix}_{\Sigma}^{R} = \begin{bmatrix} \cos\theta_1 & \sin\theta_1 & (d/a)\sin\theta_1 \\ -\sin\theta_1 & \cos\theta_1 & -b/a + (d/a)\cos\theta_1 \\ 0 & 0 & 0 \end{bmatrix} \begin{Bmatrix} V_0 \\ \Delta_0 \\ \varphi_0 a \end{Bmatrix} \mathrm{e}^{-i\omega t} \quad (2.3.9a)$$

Where the matrix on the right-hand side is the foundation influence matrix. Similarly, perfect bond between the skeleton and the foundation, and unsealed contact (i.e. free drainage of the pore fluid) imply

$$\begin{Bmatrix} u_{r_1} \\ u_{\theta_1} \\ s \end{Bmatrix}_{\Sigma}^{ff} + \begin{Bmatrix} u_{r_1} \\ u_{\theta_1} \\ s \end{Bmatrix}_{\Sigma}^{R} = \begin{bmatrix} \cos\theta_1 & \sin\theta_1 & (d/a)\sin\theta_1 \\ -\sin\theta_1 & \cos\theta_1 & -b/a + (d/a)\cos\theta_1 \\ 0 & 0 & 0 \end{bmatrix} \begin{Bmatrix} V_0 \\ \Delta_0 \\ \varphi_0 a \end{Bmatrix} \mathrm{e}^{-i\omega t} \quad (2.3.9b)$$

The application of these conditions enables expressing the unknown coefficients of expansion of the scattered waves in terms of the known free-field displacements, and the displacements of the foundation. However, this requires expansion of the free-field displacements at $r_1 = b$ in Fourier series of θ_1 with period 2π. This can be done by expanding the potentials in Fourier-Bessel series, and then computing the displacements, similarly as for the scattered waves, but such series converge only for the plane waves, and diverge for the surface waves (Lee and Cao, 1989). Hence, for the surface waves, we expand the displacements at $r_1 = b$ in Finite Fourier series of θ_1, up to $n = N$, which is the truncation index for the expansion of the scattered and plane free-field waves (Lee and Cao, 1989). Let us assume that such expansions are available, with $A_n^{\bullet}$ and $B_n^{\bullet}$ being the Fourier coefficients for the symmetric and anti-symmetric terms. Then

$$\begin{Bmatrix} u_{r_1} \\ u_{\theta_1} \\ \left(u_{r_1} - U_{r_1}\right) \end{Bmatrix}_{\Sigma}^{ff} = \frac{1}{b}\sum_{n=0}^{N}\left\{\begin{Bmatrix} A_n^{u_r}\cos n\theta_1 \\ A_n^{u_\theta}\sin n\theta_1 \\ \left(A_n^{u_r} - A_n^{U_r}\right)\cos n\theta_1 \end{Bmatrix} + \begin{Bmatrix} B_n^{u_r}\sin n\theta_1 \\ B_n^{u_\theta}\cos n\theta_1 \\ \left(B_n^{u_r} - B_n^{U_r}\right)\sin n\theta_1 \end{Bmatrix}\right\} \tag{2.3.10a}$$

and

$$\begin{Bmatrix} u_{r_1} \\ u_{\theta_1} \\ s \end{Bmatrix}_{\Sigma}^{ff} = \frac{1}{b}\sum_{n=0}^{N}\left\{\begin{Bmatrix} A_n^{u_r}\cos n\theta_1 \\ A_n^{u_\theta}\sin n\theta_1 \\ A_n^{s}\cos n\theta_1 \end{Bmatrix} + \begin{Bmatrix} B_n^{u_r}\sin n\theta_1 \\ B_n^{u_\theta}\cos n\theta_1 \\ B_n^{s}\sin n\theta_1 \end{Bmatrix}\right\} \tag{2.3.10b}$$

For the scattered waves

$$\begin{aligned}\begin{Bmatrix} u_{r_1} \\ u_{\theta_1} \\ \left(u_{r_1} - U_{r_1}\right) \end{Bmatrix}_{\Sigma}^{R} = \frac{1}{b}\sum_{n=0}^{N}\Bigg\{&\begin{bmatrix} D_{11}^{(3)}\cos n\theta_1 & D_{12}^{(3)}\cos n\theta_1 & D_{13}^{(3)}\cos n\theta_1 \\ D_{21}^{(3)}\sin n\theta_1 & D_{22}^{(3)}\sin n\theta_1 & D_{23}^{(3)}\sin n\theta_1 \\ D_{11}^{(rel,3)}\cos n\theta_1 & D_{12}^{(rel,3)}\cos n\theta_1 & D_{13}^{(rel,3)}\cos n\theta_1 \end{bmatrix}_{\Sigma}\begin{Bmatrix} A_{1,n} \\ E_{1,n} \\ C_{1,n} \end{Bmatrix} \\ &+\begin{bmatrix} D_{11}^{(3)}\cos n\theta_1 & D_{12}^{(3)}\cos n\theta_1 & D_{13}^{(3)}\cos n\theta_1 \\ D_{21}^{(3)}\sin n\theta_1 & D_{22}^{(3)}\sin n\theta_1 & D_{23}^{(3)}\sin n\theta_1 \\ D_{11}^{(rel,3)}\cos n\theta_1 & D_{12}^{(rel,3)}\cos n\theta_1 & D_{13}^{(rel,3)}\cos n\theta_1 \end{bmatrix}_{\Sigma}\begin{Bmatrix} B_{1,n} \\ F_{1,n} \\ D_{1,n} \end{Bmatrix}\Bigg\}\end{aligned} \tag{2.3.11a}$$

where

$$D_{ij}^{(rel,3)} = D_{ij}^{(f,3)} - D_{ij}^{(3)} \tag{2.3.11b}$$

and

$$
\begin{Bmatrix} u_{r_1} \\ u_{\theta_1} \\ s \end{Bmatrix}_{\Sigma}^{R} = \frac{1}{b}\sum_{n=0}^{N}\left\{\begin{bmatrix} D_{11}^{(3)}\cos\theta_1 & D_{12}^{(3)}\cos\theta_1 & D_{13}^{(3)}\cos\theta_1 \\ D_{21}^{(3)}\sin\theta_1 & D_{22}^{(3)}\sin\theta_1 & D_{23}^{(3)}\sin\theta_1 \\ E_{11}^{(f,3)}\cos\theta_1 & E_{12}^{(f,3)}\cos\theta_1 & E_{13}^{(f,3)}\cos\theta_1 \end{bmatrix}_{\Sigma}\begin{Bmatrix} A_{1,n} \\ E_{1,n} \\ C_{1,n} \end{Bmatrix}\right.
$$

$$
\left.+\begin{bmatrix} D_{11}^{(3)}\cos\theta_1 & D_{12}^{(3)}\cos\theta_1 & D_{13}^{(3)}\cos\theta_1 \\ D_{21}^{(3)}\sin\theta_1 & D_{22}^{(3)}\sin\theta_1 & D_{23}^{(3)}\sin\theta_1 \\ E_{11}^{(f,3)}\cos\theta_1 & E_{12}^{(f,3)}\cos\theta_1 & E_{13}^{(f,3)}\cos\theta_1 \end{bmatrix}_{\Sigma}\begin{Bmatrix} B_{1,n} \\ F_{1,n} \\ D_{1,n} \end{Bmatrix}\right\} \tag{2.3.11c}
$$

After substitution for the appropriate expansions in eqn's (2.3.11a) and (2.3.11b), and matching the terms multiplying the same basis functions (due to the orthogonality of Fourier series), the coefficients of expansion of the scattered field can be expressed in terms of the coefficients of expansion of the free-field motion and the displacements of the foundation. Then for sealed boundary

$$
\begin{Bmatrix} A_{1,n} \\ E_{1,n} \\ C_{1,n} \end{Bmatrix} = \left[D_{\Sigma,\text{sealed}}^{(3)+}\right]^{-1}\left\{-\begin{Bmatrix} A_n^{u_r} \\ A_n^{u_\theta} \\ A_n^{u_r} - A_n^{U_r} \end{Bmatrix} + \left[X^{+}(n)\right]\begin{Bmatrix} V_0 \\ \Delta_0 \\ \varphi_0 a \end{Bmatrix}\right\}, \quad n = 0,\ldots,N
$$

$$
\begin{Bmatrix} B_{1,n} \\ F_{1,n} \\ D_{1,n} \end{Bmatrix} = \left[D_{\Sigma,\text{sealed}}^{(3)-}\right]^{-1}\left\{-\begin{Bmatrix} B_n^{u_r} \\ B_n^{u_\theta} \\ B_n^{u_r} - B_n^{U_r} \end{Bmatrix} + \left[X^{-}(n)\right]\begin{Bmatrix} V_0 \\ \Delta_0 \\ \varphi_0 a \end{Bmatrix}\right\}, \quad n = 0,\ldots,N \tag{2.3.12a}
$$

and for an unsealed boundary

$$
\begin{Bmatrix} A_{1,n} \\ E_{1,n} \\ C_{1,n} \end{Bmatrix} = \left[D_{\Sigma,\text{unsealed}}^{(3)+}\right]^{-1}\left\{-\begin{Bmatrix} A_n^{u_r} \\ A_n^{u_\theta} \\ A_n^{s} \end{Bmatrix} + \left[X^{+}(n)\right]\begin{Bmatrix} V_0 \\ \Delta_0 \\ \varphi_0 a \end{Bmatrix}\right\}, \quad n = 0,\ldots,N
$$

$$
\begin{Bmatrix} B_{1,n} \\ F_{1,n} \\ D_{1,n} \end{Bmatrix} = \left[D_{\Sigma,\text{unsealed}}^{(3)+}\right]^{-1}\left\{-\begin{Bmatrix} B_n^{u_r} \\ B_n^{u_\theta} \\ B_n^{s} \end{Bmatrix} + \left[X^{-}(n)\right]\begin{Bmatrix} V_0 \\ \Delta_0 \\ \varphi_0 a \end{Bmatrix}\right\}, \quad n = 0,\ldots,N \tag{2.3.12b}
$$

where

$$\left[D_{\Sigma,\text{sealed}}^{(3)\pm}\right]=\begin{bmatrix} D_{11}^{(3)} & D_{12}^{(3)} & D_{13}^{(3)} \\ D_{21}^{(3)} & D_{22}^{(3)} & D_{23}^{(3)} \\ D_{11}^{(rel,3)} & D_{12}^{(rel,3)} & D_{13}^{(rel,3)} \end{bmatrix}^{\pm}(n,b)$$
$$\left[D_{\Sigma,\text{unsealed}}^{(3)\pm}\right]=\begin{bmatrix} D_{11}^{(3)} & D_{12}^{(3)} & D_{13}^{(3)} \\ D_{21}^{(3)} & D_{22}^{(3)} & D_{23}^{(3)} \\ E_{11}^{(f,3)} & E_{12}^{(f,3)} & E_{13}^{(f,3)} \end{bmatrix}^{\pm}(n,b) \tag{2.3.13}$$

$$\left[X^{+}(n)\right]=\begin{bmatrix} -1 & 0 & 0 \\ 0 & 0 & 0 \\ 0 & 0 & 0 \end{bmatrix},\quad n=1$$
$$\left[X^{+}(n)\right]=\begin{bmatrix} 0 & 0 & 0 \\ 0 & 0 & 0 \\ 0 & 0 & 0 \end{bmatrix},\quad n\neq 1 \tag{2.3.14a}$$

$$\left[X^{-}(n)\right]=\begin{bmatrix} 0 & 0 & 0 \\ 0 & 0 & -b/a \\ 0 & 0 & 0 \end{bmatrix},\quad n=0$$
$$\left[X^{-}(n)\right]=\begin{bmatrix} 0 & 1 & d/a \\ 0 & 1 & d/a \\ 0 & 0 & 0 \end{bmatrix},\quad n=1 \tag{2.3.14b}$$
$$\left[X^{-}(n)\right]=\begin{bmatrix} 0 & 0 & 0 \\ 0 & 0 & 0 \\ 0 & 0 & 0 \end{bmatrix},\quad n>1$$

2.4.3 Integral of Stresses along the Contact Surface

Next we compute vertical and horizontal forces $f_z^{(s)}$ and $f_x^{(s)}$, and moment about O, $M_0^{(s)}$, which result from all stresses in the soil along the contact surface Σ, and have signs as shown in Fig. 2.3.1. We also introduce a generalized force vector notation for this triplet of forces and moment $\mathbf{F} = \left\{ f_z , f_x , M_0 / a \right\}^T$ and refer to it as *the force*, and generalized displacement vector $\boldsymbol{\Delta} = \left\{ V, \Delta, \varphi a \right\}^T$ and refer to it as *the displacement*. For harmonic excitation, $\boldsymbol{\Delta}$ is also harmonic and can be written as

$$\boldsymbol{\Delta} = \boldsymbol{\Delta}_0 e^{-i\omega t} \tag{2.3.15}$$

where $\boldsymbol{\Delta}_0$ is its complex amplitude.

The resultant force vector, $\mathbf{F}^{(s)}$, is the sum of the force vectors due to the free-field motion and due to the scattered waves, $\mathbf{F}_{ff}^{(s)}$ and $\mathbf{F}_{R}^{(s)}$, and can be computed as follows

$$\begin{aligned}\mathbf{F}^{(s)} &= \mathbf{F}_{ff}^{(s)} + \mathbf{F}_{R}^{(s)} \\ &= \int_{-\theta_0}^{\theta_0} b \begin{bmatrix} -\cos\theta_1 & +\sin\theta_1 \\ -\sin\theta_1 & -\cos\theta_1 \\ -(d/a)\sin\theta_1 & b/a-(d/a)\cos\theta_1 \end{bmatrix} \left\{ \begin{Bmatrix} \tau_{r_1 r_1} + s \\ \tau_{r_1\theta_1} \end{Bmatrix}_{\Sigma}^{ff} + \begin{Bmatrix} \tau_{r_1 r_1} + s \\ \tau_{r_1\theta_1} \end{Bmatrix}_{\Sigma}^{R} \right\} d\theta_1 \end{aligned} \tag{2.3.16}$$

Eqn (2.36) holds for both sealed and unsealed conditions. We note however that, for an unsealed boundary, the total stress in the pore fluid, $s^{ff} + s^{R}$, is actually zero on the boundary, as preset by the drainage condition (see eqn (2.29b)).

Similarly as in Section 2.3.1, we expand the stresses of the free-field motion along the contact surface in Fourier series of θ_1 with period 2π

$$\begin{Bmatrix} \tau_{r_1 r_1} + s \\ \tau_{r_1\theta_1} \end{Bmatrix}_{\Sigma}^{ff} = \frac{2\mu}{b^2} \sum_{n=0}^{N} \left\{ \begin{Bmatrix} (A_n^{\tau_{rr}} + A_n^{s}) \cos n\theta_1 \\ A_n^{\tau_{r\theta}} \sin n\theta_1 \end{Bmatrix} + \begin{Bmatrix} (B_n^{\tau_{rr}} + B_n^{s}) \sin n\theta_1 \\ B_n^{\tau_{r\theta}} \cos n\theta_1 \end{Bmatrix} \right\} e^{-i\omega t} \tag{2.3.17}$$

and substitute in eqn (2.3.16). Then, for the forces due to the free-field motion we get

$$\mathbf{F}_{ff}^{(s)} = \frac{2\mu}{b}\sum_{n=0}^{N}\left\{\left[L^{+}(n)\right]\begin{Bmatrix} A_n^{\tau_{rr}} + A_n^{s} \\ A_n^{\tau_{r\theta}} \end{Bmatrix} + \left[L^{-}(n)\right]\begin{Bmatrix} B_n^{\tau_{rr}} + B_n^{s} \\ B_n^{\tau_{r\theta}} \end{Bmatrix}\right\} e^{-i\omega t} \tag{2.3.18}$$

where

$$\begin{aligned}
\left[L^{+}(n)\right] &= \int_{-\theta_0}^{\theta_0}\begin{bmatrix} -\cos\theta_1\cos n\theta_1 & \sin\theta_1\sin\theta_1 \\ -\sin\theta_1\cos n\theta_1 & -\cos\theta\sin\theta_{11} \\ -(d/a)\sin\theta_1\cos n\theta_1 & \left[b/a-(d/a)\cos\theta_1\right]\sin n\theta_1 \end{bmatrix} d\theta_1 \\
\left[L^{-}(n)\right] &= \int_{-\theta_0}^{\theta_0}\begin{bmatrix} -\cos\theta_1\sin n\theta_1 & \sin\theta_1\cos\theta_1 \\ -\sin\theta_1\sin n\theta_1 & -\cos\theta\cos\theta_1 \\ -(d/a)\sin\theta_1\sin n\theta_1 & \left[b/a-(d/a)\cos\theta_1\right]\cos n\theta_1 \end{bmatrix} d\theta_1
\end{aligned} \tag{2.3.19}$$

Some of the terms of matrices $\left[L^{+}(n)\right]$ and $\left[L^{-}(n)\right]$ are automatically zero (when the integrand is an odd function), and the nonzero ones can be evaluated analytically, which gives

$$\begin{aligned}
\left[L^{+}(n)\right] &= \begin{bmatrix} -I_1(n) & I_4(n) \\ 0 & 0 \\ 0 & 0 \end{bmatrix} \\
\left[L^{-}(n)\right] &= \begin{bmatrix} 0 & 0 \\ -I_4(n) & -I_1(n) \\ -(d/a)I_4(n) & (b/a)I_5(n)-(d/a)I_1(n) \end{bmatrix}
\end{aligned} \tag{2.3.20}$$

The expressions for the integrals $I_1(n)$, $I_4(n)$, and $I_5(n)$ are given in Appendix. Similarly, for the forces from the scattered waves we get

$$\mathbf{F}_{R}^{(s)} = \frac{2\mu}{b}\sum_{n=0}^{N}\left\{\left[L^{+}(n)\right]\left[E_{\Sigma}^{(3)+}(n)\right]\begin{Bmatrix} A_{1,n} \\ E_{1,n} \\ C_{1,n} \end{Bmatrix} + \left[L^{-}(n)\right]\left[E_{\Sigma}^{(3)-}(n)\right]\begin{Bmatrix} B_{1,n} \\ F_{1,n} \\ D_{1,n} \end{Bmatrix}\right\} e^{-i\omega t} \tag{2.3.21}$$

where

$$\left[E_{\Sigma}^{(3)\pm}(n)\right]=\begin{bmatrix} E_{11}^{(3)}+E_{11}^{(f,3)} & E_{12}^{(3)}+E_{12}^{(f,3)} & E_{13}^{(3)}+E_{13}^{(f,3)} \\ E_{21}^{(3)} & E_{22}^{(3)} & E_{23}^{(3)} \end{bmatrix}^{\pm}(n,b) \tag{2.3.22}$$

Further, substituting in eqn (2.3.16) for the coefficients of expansion of the scattered waves from eqn (2.3.12a,b) it follows that for a sealed boundary

$$\begin{aligned}\mathbf{F}_{\mathrm{R}}^{(s)}=\frac{2\mu}{b}\sum_{n=0}^{N}\Bigg\{&\left[L^{+}(n)\right]\left[E_{\Sigma}^{(3)+}(n)\right]\left[D_{\Sigma,\text{sealed}}^{(3)+}\right]^{-1}\left\{-\begin{Bmatrix} A_n^{u_r} \\ A_n^{u_\theta} \\ A_n^{u_r}-A_n^{U_r}\end{Bmatrix}+b\left[X^{+}(n)\right]\begin{Bmatrix} V_0 \\ \Delta_0 \\ \varphi_0 a\end{Bmatrix}\right\} \\ &+\left[L^{-}(n)\right]\left[E_{\Sigma}^{(3)-}(n)\right]\left[D_{\Sigma,\text{sealed}}^{(3)-}\right]^{-1}\left\{-\begin{Bmatrix} B_n^{u_r} \\ B_n^{u_\theta} \\ B_n^{u_r}-B_n^{U_r}\end{Bmatrix}+b\left[X^{-}(n)\right]\begin{Bmatrix} V_0 \\ \Delta_0 \\ \varphi_0 a\end{Bmatrix}\right\}\Bigg\}e^{-i\omega t}\end{aligned} \tag{2.3.23}$$

It is seen that $\mathbf{F}_{R}^{(s)}$ depends both on the displacements from the free-field motion and that of the foundation, and can be written as

$$\mathbf{F}_{\mathrm{R}}^{(s)}=\mathbf{F}_{\text{scat}}^{(s)}+\mathbf{F}_{\Delta}^{(s)} \tag{2.3.24}$$

where

$$\mathbf{F}_{\Delta}^{(s)}=2\mu\left[K^{(s)}\right]\boldsymbol{\Delta} \tag{2.3.25}$$

with

$$\begin{aligned}\left[K^{(s)}\right]=2\mu\sum_{n=0}^{N}\Big[&\left[L^{+}(n)\right]\left[E_{\Sigma}^{(3)+}(n)\right]\left[D_{\Sigma,\text{sealed}}^{(3)+}\right]^{-1}\left[X^{+}(n)\right] \\ &+\left[L^{-}(n)\right]\left[E_{\Sigma}^{(3)-}(n)\right]\left[D_{\Sigma,\text{sealed}}^{(3)-}\right]^{-1}\left[X^{-}(n)\right]\Big]\end{aligned} \tag{2.3.26}$$

and

$$\mathbf{F}^{(s)}_{\text{scat}} = -\frac{2\mu}{b}\sum_{n=0}^{N}\left\{\left[L^{+}(n)\right]\left[E^{(3)+}_{\Sigma}(n)\right]\left[D^{(3)+}_{\Sigma,\text{sealed}}\right]^{-1}\begin{Bmatrix} A^{u_r}_n \\ A^{u_\theta}_n \\ A^{u_r}_n - A^{U_r}_n \end{Bmatrix}\right.$$
$$\left. + \left[L^{-}(n)\right]\left[E^{(3)-}_{\Sigma}(n)\right]\left[D^{(3)-}_{\Sigma,\text{sealed}}\right]^{-1}\begin{Bmatrix} B^{u_r}_n \\ B^{u_\theta}_n \\ B^{u_r}_n - B^{U_r}_n \end{Bmatrix}\right\} e^{-i\omega t} \tag{2.3.27}$$

For an unsealed boundary

$$\left[K^{(s)}\right] = \sum_{n=0}^{N}\Big[\left[L^{+}(n)\right]\left[E^{(3)+}_{\Sigma}(n)\right]\left[D^{(3)+}_{\Sigma,\text{unsealed}}\right]^{-1}\left[X^{+}(n)\right]$$
$$+\left[L^{-}(n)\right]\left[E^{(3)-}_{\Sigma}(n)\right]\left[D^{(3)-}_{\Sigma,\text{unsealed}}\right]^{-1}\left[X^{-}(n)\right]\Big] \tag{2.3.28}$$

and

$$\mathbf{F}^{(s)}_{\text{scat}} = -\frac{2\mu}{b}\sum_{n=0}^{N}\left\{\left[L^{+}(n)\right]\left[E^{(3)+}_{\Sigma}(n)\right]\left[D^{(3)+}_{\Sigma,\text{unsealed}}\right]^{-1}\begin{Bmatrix} A^{u_r}_n \\ A^{u_\theta}_n \\ A^{s}_n \end{Bmatrix}\right.$$
$$\left. + \left[L^{-}(n)\right]\left[E^{(3)-}_{\Sigma}(n)\right]\left[D^{(3)-}_{\Sigma,\text{unsealed}}\right]^{-1}\begin{Bmatrix} B^{u_r}_n \\ B^{u_\theta}_n \\ B^{s}_n \end{Bmatrix}\right\} e^{-i\omega t} \tag{2.3.29}$$

Then the integral of all stresses in the soil along the contact surface is

$$\begin{aligned}\mathbf{F}^{(s)} &= \mathbf{F}^{(s)}_{\text{ff}} + \mathbf{F}^{(s)}_{\text{scat}} + \mathbf{F}^{(s)}_{\Delta} \\ &= \mathbf{F}^{(s)}_{\text{driv}} + \mathbf{F}^{(s)}_{\Delta}\end{aligned} \tag{2.3.30}$$

where

$$\mathbf{F}^{(s)}_{\text{driv}} = \mathbf{F}^{(s)}_{\text{ff}} + \mathbf{F}^{(s)}_{\text{scat}} \tag{2.3.31}$$

The interpretation of these forces and of matrix $\left[K^{(s)}\right]$ is as follows. $\mathbf{F}_{\Delta}^{(s)}$ defined by eqn (2.3.25) is an external force required to move the foundation by displacement $\mathbf{\Delta}$ when there is no free-field motion, and the matrix elating them, $2\mu\left[K^{(s)}\right]$, is the foundation stiffness matrix. This matrix is complex, with its real part representing the stiffness of the foundation, and its imaginary part the radiation damping. $\mathbf{F}_{\text{driv}}^{(s)}$ defined by eqn (2.3.31) is the external force required to hold the foundation in place when it is subjected to the action of the free-field waves. Its reaction is the force with which the free-field motion effectively drives the foundation, and is the generalized foundation driving force. It is different from force $\mathbf{F}_{\text{ff}}^{(s)}$, which is the integral of the stresses of the free-field motion, because of the scattering of waves from the foundation.

2.4.4 Dynamic Equilibrium of the Foundation

The only remaining unknown is the foundation displacement vector, $\mathbf{\Delta}$, which can be determined from the dynamic equilibrium condition for the foundation. Fig. 2.3.2 shows a free-body diagram of the foundation, which is subjected to the forces from the building, $\mathbf{F}^{(b)}$, and the forces from the soil, $\mathbf{F}^{(s)} = \mathbf{F}_{\text{driv}}^{(s)} + 2\mu\left[K^{(s)}\right]\mathbf{\Delta}$.

For small amplitudes of the response, the forces from the building can be represented in terms of the displacement vector, $\mathbf{\Delta}$, as follows (Todorovska, 1993b)

$$\mathbf{F}^{(b)} = m_b\omega^2\left[M_b\right]\mathbf{\Delta} \tag{2.3.32}$$

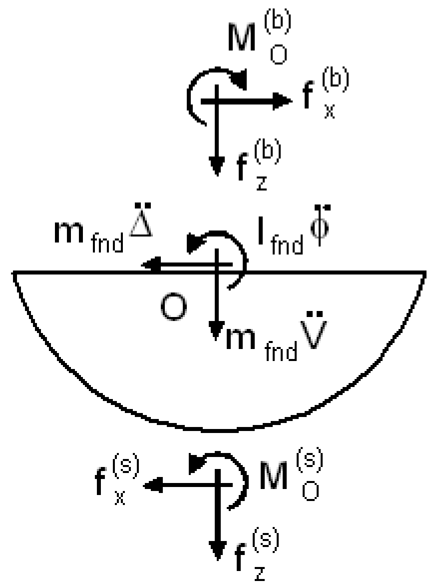

Fig. 2.4.2 Dynamic equilibrium of the foundation.

where $\left[M_b\right]$ is a dimensionless matrix that depends on the building model and characteristics. For a shear beam model, and neglecting the effect of the gravity forces, its entries are

$$
\begin{aligned}
M_{b,11} &= \frac{\tan\left(\omega H / V_{P,b}\right)}{\omega H / V_{P,b}} \\
M_{b,22} &= \frac{\tan\left(\omega H / V_{S,b}\right)}{\omega H / V_{S,b}} \\
M_{b,23} = M_{b,32} &= \frac{-1}{(\omega H / V_{S,b})^2}\left(1 - 1/\cos\left(\omega H / V_{S,b}\right)\right)\frac{H}{a} \\
M_{b,33} &= \left[\frac{1}{(\omega H / V_{S,b})^2}\left(1 - \frac{\tan\left(\omega H / V_{S,b}\right)}{\omega H / V_{S,b}}\right) + \frac{1}{12}(W/H)^2\right]\left(\frac{H}{a}\right)^2
\end{aligned}
\tag{2.3.33}
$$

In eqns (2.3.32) and (2.3.33), m_b is the mass per unit length of the beam, and H and W are its height and width, and $V_{S,b}$ and $V_{P,b}$ are its S and P wave velocities. The dynamic equilibrium of forces acting onto the foundation implies

$$\omega^2 m_{\text{fnd}} \left[M_{\text{fnd}}\right]\mathbf{\Delta} - \mathbf{F}_{\text{driv}}^{(\text{s})} - 2\mu\left[K^{(s)}\right]\mathbf{\Delta} + \omega^2 m_{\text{b}}\left[M_{\text{b}}\right]\mathbf{\Delta} = \mathbf{0} \qquad (2.3.34)$$

where m_{fnd} is the mass of the foundation, $\left[M_{\text{fnd}}\right]$ is the foundation dimensionless mass matrix

$$\left[M_{\text{fnd}}\right] = \begin{bmatrix} 1 & 0 & 0 \\ 0 & 1 & 0 \\ 0 & 0 & I_{\text{fnd},0}/(m_{\text{fnd}}a^2) \end{bmatrix} \qquad (2.3.35)$$

where

$$I_{\text{fnd},0} = \frac{b^2 m_{\text{fnd}}}{\theta_0 - \sin\theta_0\cos\theta_0}\left[\left(\tfrac{1}{2} + \cos^2\theta_0\right)\theta_0 - \tfrac{3}{2}\sin\theta_0\cos\theta_0\right] \qquad (2.3.36)$$

is the mass moment of inertia of the foundation relative to point *O*, and m_{fnd} is the mass per unit length of the foundation. Finally, one can solve for $\mathbf{\Delta}$ by inverting a 3×3 matrix

$$\mathbf{\Delta} = \left[\frac{\omega^2 m_{\text{fnd}}}{2\mu}\left[M_{\text{fnd}}\right] + \frac{\omega^2 m_{\text{b}}}{2\mu}\left[M_{\text{b}}\right] - \left[K^{(s)}\right]\right]^{-1} 2\mu\,\mathbf{F}_{\text{driv}}^{(\text{s})} \qquad (2.3.37)$$

For the purpose of brevity, and without loss of generality, the dynamic moments of the gravity forces were neglected in the above derivations. The expressions including these moments can be found in Todorovska (1993a,b).

2.5 The Free-Field Motion

This section deals with the representation of the free-field motion for incident plane P-wave, incident plane SV-wave, and for a Rayleigh wave in a fully saturated porous half-space, considering the effects of the seepage force (which leads to complex valued and frequency dependent wave velocity in the mixture). The coefficients of the reflected waves of the P- and S-wave potentials of the Rayleigh waves are derived for open (permeable) and sealed (impermeable) hydraulic condition on the half-space boundary, for which the zero stress condition on the half-space surface is Deresiewicz (1960)

$$\begin{Bmatrix} \tau_{yy} \\ \tau_{xy} \\ \sigma \end{Bmatrix}_{y=0} = \begin{Bmatrix} 0 \\ 0 \\ 0 \end{Bmatrix} \qquad \text{open (permeable) boundary} \qquad (2.4.1)$$

and

$$\begin{Bmatrix} \tau_{yy+}\sigma \\ \tau_{xy} \\ u_y - U_y \end{Bmatrix}_{y=0} = \begin{Bmatrix} 0 \\ 0 \\ 0 \end{Bmatrix} \qquad \text{sealed (impermeable) boundary} \qquad (2.4.2)$$

For incident plane waves (P and SV), the derivation presented in this section, which is for the genral dissipative case, follows Deresiewicz and Rice (1962). For the Rayleigh waves, and nondissipative case, the derivation follows Lin et al. (2005).

2.5.1 The Free Field Motion due to Incident P-Wave

Let the excitation consist of a plane fast P-wave incident onto the half-space free surface (Fig. 2.4.1), represented by its potential

$$\phi^i = \exp[i\kappa_\alpha(x\sin\gamma - z\cos\gamma) - i\omega t] \tag{2.4.3}$$

Its interaction with the free surface will generate a triplet of reflected waves, consisting of a fast and slow P-wave and an S-wave, represented by their wave potentials

$$\varphi_f{}^r = K_{1f}\exp[ik_f(x\sin\theta_{\alpha f} + z\cos\theta_{\alpha f}) - i\omega t] \tag{2.4.4a}$$

$$\varphi_s{}^r = K_{1s}\exp[ik_s(x\sin\theta_{\alpha s} + z\cos\theta_{\alpha s}) - i\omega t] \tag{2.4.4b}$$

$$\psi^r = K_2\exp[ik_\beta(x\sin\theta_\beta + z\cos\theta_\beta) - i\omega t] \tag{2.4.4c}$$

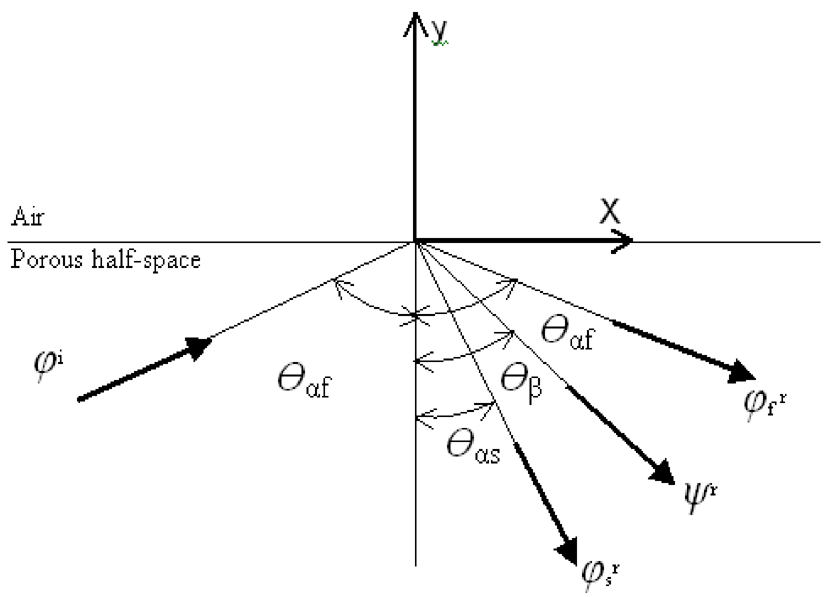

Fig. 2.5.1 Fluid-saturated porous half-space subjected to incident P-wave.

where

k_f the complex wave number of the fast plane P-wave

k_s the complex wave number of the slow plane P-wave

k_β the complex wave number of the shear plane wave

We recall that the wave numbers are in general complex, when the dissipation forces due to the seepage force are considered. These wave numbers can be written in terms of their real and imaginary parts as

$$k_j = \eta_{kr} - i\eta_{ki}, \quad j = f, s, \beta \tag{2.4.5}$$

To ensure dissipation at infinity η_{ki} in eqn (2.4.3) should be positive. In this work, the angles of incident wave and of the reflected waves are taken as in H. Deresiewicz and Rice (1962)

$$\theta_j^k = \arc\tan \frac{\eta_{kr} \sin\theta_k}{\eta_{lr} p_l^{(k)} - \eta_{li} q_l^{(k)} \operatorname{sgn} n_l^{(k)}} \tag{2.4.6}$$

where

θ_j^k is the reflection angle, θ_k the incident angle, and η_{kr}, and η_{li} are the real and imaginary parts of the wave numbers.

$$n_l^{(k)} = \frac{\eta_{kr}\eta_{li} - \eta_{ki}\eta_{lr}}{\eta_{lr}^2 + \eta_{li}^2} \sin\theta_k \tag{2.4.7}$$

The reflection angle sine and cosine for the case of $l \neq k$ can be written as

$$\sin_{l1}^{(k)} = m_l^{(k)} + i n_l^{(k)} \tag{2.4.8}$$

$$\cos_{l3}^{(k)} = p_l^{(k)} i q_l^{(k)} \operatorname{sgn} n_l^{(k)} \tag{2.4.9}$$

where

$$m_l^{(k)} = \frac{\eta_{kr}\eta_{lr} + \eta_{ki}\eta_{li}}{\eta_{lr}^2 + \eta_{li}^2} \sin\theta_k \tag{2.4.10}$$

$$p_l^{(k)}, q_l^{(k)} = \frac{1}{\sqrt{2}}\left[\sqrt{\left(K_l^{(k)}\right)^2 + \left(L_l^{(k)}\right)^2} \pm K_l^{(k)}\right]^{1/2}, \tag{2.4.11}$$

$$K_l^{(k)} = 1 - \left(m_l^{(k)}\right)^2 + \left(n_l^{(k)}\right)^2 \tag{2.4.12a}$$

and

$$L_l^{(k)} = 2 m_l^{(k)} n_l^{(k)} \tag{2.4.12b}$$

To determine the reflection coefficients both boundary conditions at the free surface are taken (open boundary and sealed boundary condition):

For open (permeable) half-space surface, the zero stress condition implies

$$\begin{bmatrix} G_{11,1} & G_{11,2} & -G_{12} \\ -G_{21,1} & -G_{21,2} & G_{22} \\ G_{61,1} & G_{61,2} & 0 \end{bmatrix} \begin{Bmatrix} K_{1f} \\ K_{1s} \\ K_2 \end{Bmatrix} = -a_0 \begin{Bmatrix} G_{11,1} \\ G_{21,1} \\ G_{61,1} \end{Bmatrix} \tag{2.4.13}$$

and for sealed (impermeable) half-space surface

$$\begin{bmatrix} G_{11,1} + G_{61,1} & G_{11,2} + G_{61,2} & -G_{12} \\ -G_{21,1} & -G_{21,2} & G_{22} \\ -(1-f_1)G_{41,1} & -(1-f_2)G_{41,2} & (1-f_3)G_{42} \end{bmatrix} \begin{Bmatrix} K_{1f} \\ K_{1s} \\ K_2 \end{Bmatrix} = -a_0 \begin{Bmatrix} G_{11,1} + G_{61,1} \\ G_{21,1} \\ (1-f_1)G_{41,1} \end{Bmatrix} \tag{2.4.14}$$

where

$$G_{11,1} = -k_{\alpha f}{}^2 (M_1 - 2\sin^2\theta_{\alpha f}) \tag{2.4.15a}$$

$$G_{11,2} = -k_{\alpha s}{}^2 (M_2 - 2\sin^2\theta_{\alpha s}) \tag{2.4.15b}$$

$$G_{12} = k_\beta{}^2 \sin 2\theta_\beta \tag{2.4.15c}$$

$$G_{21,1} = -k_{\alpha f}{}^2 \sin 2\theta_{\alpha f} \tag{2.4.15d}$$

$$G_{21,2} = -k_{\alpha s}{}^2 \sin 2\theta_{\alpha s} \tag{2.4.15e}$$

$$G_{22} = -k_\beta{}^2 \cos 2\theta_\beta \tag{2.4.15f}$$

$$G_{41,1} = ik_{\alpha f} \cos\theta_{\alpha f} \tag{2.4.15g}$$

$$G_{41,2} = ik_{\alpha s} \cos\theta_{\alpha s} \tag{2.4.15h}$$

$$G_{42} = -ik_\beta \sin\theta_\beta \tag{2.4.15i}$$

$$G_{61,1} = -k_{\alpha f}{}^2 S_1 \tag{2.4.15j}$$

$$G_{61,2} = -k_{\alpha s}{}^2 S_2 \tag{2.4.15k}$$

2.5.2 The Free Field Motion due to Incident SV-Wave

Similarly as for the fast incident P-wave, an incident SV wave can be represented by its potential

$$\psi^i = \exp[i\kappa_\alpha(x\sin\gamma - z\cos\gamma) - i\omega t] \tag{2.4.16}$$

and the interaction with the free-surface will generate the reflected fast and slow P-wave and an SV-wave, represented by their potentials

$$\varphi_f{}^r = K_{1f} \exp[ik_f(x\sin\theta_{\alpha f} + z\cos\theta_{\alpha f}) - i\omega t] \tag{2.4.17}$$

$$\varphi_s{}^r = K_{1s} \exp[ik_s(x\sin\theta_{\alpha s} + z\cos\theta_{\alpha s}) - i\omega t] \tag{2.4.18}$$

$$\psi^r = K_2 \exp[ik_\beta (x\sin\theta_\beta + z\cos\theta_\beta) - i\omega t] \tag{2.4.19}$$

The critical angle for the fast P-wave is

$$\theta_{cr} = \sin^{-1}\sqrt{\mu / P + 2Q + R} \tag{2.4.20}$$

The zero stress condition for open (permeable) half-space surface implies

$$\begin{bmatrix} G_{11,1} & G_{11,2} & -G_{12} \\ -G_{21,1} & -G_{21,2} & G_{22} \\ G_{61,1} & G_{61,2} & 0 \end{bmatrix} \begin{Bmatrix} K_{1f} \\ K_{1s} \\ K_2 \end{Bmatrix} = -b_0 \begin{Bmatrix} G^*_{12} \\ G^*_{22} \\ 0 \end{Bmatrix} \tag{2.4.21}$$

and for sealed (impermeable) half-space surface it implies

$$\begin{bmatrix} G_{11,1} + G_{61,1} & G_{11,2} + G_{61,2} & -G_{12} \\ -G_{21,1} & -G_{21,2} & G_{22} \\ -(1-f_1)G_{41,1} & -(1-f_2)G_{41,2} & (1-f_3)G_{42} \end{bmatrix} \begin{Bmatrix} K_{1f} \\ K_{1s} \\ K_2 \end{Bmatrix} = -b_0 \begin{Bmatrix} G^*_{12} \\ G^*_{22} \\ (1-f_3)G^*_{42} \end{Bmatrix} \tag{2.4.22}$$

2.5.3 The Free Field Motion due to Rayleigh-Wave

A Rayleigh in the half-space propagating in the positive x- direction can be represented by its potentials

$$\phi_f = c_f e^{-b_{1f} y} e^{i(kx - \omega t)}$$

$$\phi_s = c_s e^{-b_{1s} y} e^{i(kx - \omega t)} \tag{2.4.23}$$

$$\psi = D e^{-b_2 y} e^{i(kx - \omega t)}$$

where

$$b_{1f} = k\sqrt{1 - \frac{c^2}{V_{\alpha f}^2}} \tag{2.4.24a}$$

$$b_{1s} = k\sqrt{1-\frac{c^2}{V_{\alpha s}^2}} \tag{2.4.24b}$$

$$b_2 = k\sqrt{1-\frac{c^2}{V_{\beta}^2}} \tag{2.4.24c}$$

The zero stress condition for open (permeable) half-space surface implies

$$\begin{bmatrix} G^{**}{}_{11,1} & G^{**}{}_{11,2} & -G^{**}{}_{12} \\ -G^{**}{}_{21,1} & -G^{**}{}_{21,2} & G^{**}{}_{22} \\ G^{**}{}_{61,1} & G^{**}{}_{61,2} & 0 \end{bmatrix} \begin{Bmatrix} b_{1f} \\ b_{1s} \\ D \end{Bmatrix} = \begin{Bmatrix} 0 \\ 0 \\ 0 \end{Bmatrix} \tag{2.4.25}$$

and for sealed (impermeable) half-space surface it implies

$$\begin{bmatrix} G^{**}{}_{11,1} + G^{**}{}_{61,1} & G^{**}{}_{11,2} + G^{*}{}_{61,2} & -G^{**}{}_{12} \\ -G^{**}{}_{21,1} & -G^{**}{}_{21,2} & G^{**}{}_{22} \\ -(1-f_1)G^{**}{}_{41,1} & -(1-f_2)G^{**}{}_{41,2} & (1-f_3)G^{**}{}_{42} \end{bmatrix} \begin{Bmatrix} b_{1f} \\ b_{1s} \\ D \end{Bmatrix} = \begin{Bmatrix} 0 \\ 0 \\ 0 \end{Bmatrix} \tag{2.4.26}$$

where

$$G^{**}{}_{11,1} = 2k^2 - \frac{k^2c^2M_1}{V_{\alpha f}^2} \tag{2.4.27a}$$

$$G^{**}{}_{11,2} = 2k^2 - \frac{k^2c^2M_2}{V_{\alpha s}^2} \tag{2.4.27b}$$

$$G^{**}{}_{12} = -2ik^2\sqrt{1-\frac{c^2}{V_{\beta}^2}} \tag{2.4.27c}$$

$$G^{**}{}_{21,1} = 2ik^2\sqrt{1-\frac{c^2}{V_{\alpha f}^2}} \tag{2.4.27d}$$

$$G^{**}{}_{21,2} = 2ik^2\sqrt{1-\frac{c^2}{V_{\alpha s}^2}} \tag{2.4.27e}$$

$$G^{**}{}_{22} = 2k^2 - \frac{k^2c^2}{V_\beta^2} \tag{2.4.27f}$$

$$G^{**}{}_{61,1} = -\frac{S_1k^2c^2}{V_{\alpha f}^2} \tag{2.4.27g}$$

$$G^{**}{}_{61,2} = -\frac{S_2k^2c^2}{V_{\alpha s}^2} \tag{2.4.27h}$$

For a nontrivial solution, the determinate of the matrices in eqns (2.4.25) and (2.4.26) have to be equal to zero, which gives for open (permeable) half-space surface

$$\begin{aligned}\det &= 4\left(S_2V_{\alpha f}^2 - S_1V_{\alpha s}^2\right)V_\beta^2 + 2\left(S_1V_{\alpha s}^2 - S_2V_{\alpha f}^2\right)c^2 + 2\left(S_1M_2 - S_2M_1\right)V_\beta^2c^2 \\ &+ \left(M_1S_2 - M_2S_1\right)c^4 - 4S_2V_{\alpha f}^2V_\beta^2\sqrt{1-\frac{c^2}{V_{\alpha f}^2}}\sqrt{1-\frac{c^2}{V_{\alpha s}^2}} + 4S_1V_{\alpha s}^2V_\beta^2\sqrt{1-\frac{c^2}{V_{\alpha s}^2}}\sqrt{1-\frac{c^2}{V_{\alpha s}^2}} = 0\end{aligned} \tag{4.2.28}$$

and for sealed (impermeable) half-space surface

$$\det=\left[\begin{array}{l}-\left(1-f_3\right)\left(4V_{\alpha f}^2V_{\alpha s}^2V_\beta^2-2c^2M_1V_{\alpha s}^2V_\beta^2\right)+\left(1-f_2\right)\begin{pmatrix}4V_{\alpha f}^2V_{\alpha s}^2V_\beta^2-2c^2M_1V_{\alpha s}^2V_\beta^2-\\2c^2V_{\alpha f}^2V_{\alpha s}^2+c^4M_1V_{\alpha s}^2\end{pmatrix}\\+\left(1-f_3\right)\left(2S_1c^2V_{\alpha s}^2V_\beta^2\right)+\left(1-f_2\right)\left(-2S_1c^2V_{\alpha s}^2V_\beta^2+S_1c^4V_{\alpha s}^2\right)\end{array}\right]\sqrt{1-\frac{c^2}{V_{\alpha s}^2}}$$
$$+\left[\begin{array}{l}\left(1-f_3\right)\left(4V_{\alpha f}^2V_{\alpha s}^2V_\beta^2-2c^2M_2V_{\alpha f}^2V_\beta^2\right)+\left(1-f_1\right)\begin{pmatrix}4V_{\alpha f}^2V_{\alpha s}^2V_\beta^2-2c^2M_2V_{\alpha f}^2V_\beta^2-\\2c^2V_{\alpha f}^2V_{\alpha s}^2+c^4M_2V_{\alpha f}^2\end{pmatrix}\\-\left(1-f_3\right)\left(2S_2c^2V_{\alpha f}^2V_\beta^2\right)-\left(1-f_1\right)\left(-2S_2c^2V_{\alpha s}^2V_\beta^2+S_2c^4V_{\alpha f}^2\right)\end{array}\right]\sqrt{1-\frac{c^2}{V_{\alpha f}^2}}$$
$$+\left[\left(f_2-f_1\right)4V_{\alpha f}^2V_{\alpha s}^2V_\beta^2\right]\sqrt{1-\frac{c^2}{V_{\alpha f}^2}}\sqrt{1-\frac{c^2}{V_{\alpha s}^2}}\sqrt{1-\frac{c^2}{V_\beta^2}}=0$$

(2.4.29)

Equations (2.4.28) and (2.4.29) are the characteristic equations the solution of which gives the allowable phase velocities of Rayleigh waves, c, for both conditions. Then by substituting the corresponding velocity in eqns (4.2.25) and (4.2.26), the coefficients of the wave potentials can be determined.

2.5.4 Displacements and Stresses due to the Free-Filed Motion

2.5.4.1 Rectangular Coordinates

Once the amplitude coefficients of the wave potentials have been determined, the displacements and stresses in the half-space can be computed. For a given triplet of potentials, the displacements and stresses in rectangular coordinates can be computed using the following relationships

$$\begin{pmatrix} u_x \\ u_y \end{pmatrix}_{y=0} = \begin{bmatrix} G^{**}{}_{31,1} & G^{**}{}_{31,2} & -G^{**}{}_{32} \\ -G^{**}{}_{41,1} & -G^{**}{}_{41,2} & G^{**}{}_{42} \end{bmatrix} \begin{pmatrix} C_f \\ C_s \\ D \end{pmatrix} e^{i(kx-\omega t)} \qquad (2.4.30)$$

and

$$\begin{pmatrix} \tau_{yy} \\ \tau_{xy} \\ \sigma \end{pmatrix}_{y=0} = \mu \begin{bmatrix} G^{**}{}_{11,1} & G^{**}{}_{11,2} & -G^{**}{}_{12} \\ -G^{**}{}_{21,1} & -G^{**}{}_{21,2} & G^{**}{}_{22} \\ G^{**}{}_{61,1} & G^{**}{}_{61,2} & 0 \end{bmatrix} \begin{pmatrix} C_f \\ C_s \\ D \end{pmatrix} e^{i(kx-\omega t)} \qquad (2.4.31)$$

where

C_f, C_s and D are the known coefficients of the wave potentials.

$G^{**}{}_{31,1} = ik$

$G^{**}{}_{31,2} = ik$

$G^{**}{}_{32} = b_2$

$G^{**}{}_{41,1} = b_{1f}$

$G^{**}{}_{41,2} = b_{1s}$

$G^{**}{}_{42} = -ik$

2.5.4.2 Cylindrical Coordinates and Series Expansion along the Contact Surface

To match the displacements and stresses along the contact surface, they have to be represented in Fourier-Bessel series. For the plane waves, the representation can be done easily after expansion of the corresponding wave potentials in Fourier-Bessel series using the addition theorem. For surface waves, however, these series diverge, and the addition theorem cannot be used. This problem can be avoided by computing the displacements and stresses along the contact surface, $r_1 = b$, and then expanding them in finite Fourier series of θ_1, as proposed by Lee and Cao (1989).

The derivations for the inhomogeneous waves are greatly simplified by representing them as plane waves but for a complex reflection angles. These angles are

$$\theta_{\alpha f} = \frac{\pi}{2} - i\phi_{\alpha f}$$

$$\theta_{\alpha s} = \frac{\pi}{2} - i\phi_{\alpha s} \tag{2.4.32}$$

$$\theta_{\beta} = \frac{\pi}{2} - i\phi_{\beta}$$

where $\phi_{\alpha f}$, $\phi_{\alpha s}$, ϕ_{β} are real quantities such that

$$\cosh\phi_{\alpha f} = V_{\alpha f} / c$$

$$\cosh\phi_{\alpha s} = V_{\alpha s} / c$$

$$\cosh\phi_{\beta} = V_{\beta} / c$$

Then the potentials in terms of these complex angles are

$$\phi_f = C_f e^{b_{1f} d} e^{\left(ik_{\alpha f} r_1 \cos\left(\theta_1 - \theta_{\alpha f}\right) - i\omega t\right)}$$

$$\phi_s = C_s e^{b_{1s} d} e^{\left(ik_{\alpha s} r_1 \cos\left(\theta_1 - \theta_{\alpha s}\right) - i\omega t\right)} \tag{2.4.33}$$

$$\psi = D e^{b_2 d} e^{\left(ik_{\beta} r_1 \cos\left(\theta_1 - \theta_{\beta}\right) - i\omega t\right)}$$

Displacements and stresses can be computed in cylindrical coordinates from the potentials using the following relationships

$$u_{r_1} = \frac{\partial \phi_j}{\partial r_1} + \frac{1}{r_1}\frac{\partial \psi}{\partial \theta_1} \tag{2.4.34a}$$

$$u_{\theta_1} = \frac{1}{r_1}\frac{\partial \phi_j}{\partial \theta_1} - \frac{\partial \psi}{\partial r_1} \tag{2.4.34b}$$

and

$$\tau_{r_1 r_1} = \lambda\left(\frac{\partial u_{r_1}}{\partial r_1} + \frac{u_{r_1}}{r_1} + \frac{1}{r_1}\frac{\partial u_{\theta_1}}{\partial \theta_1}\right) + Q\left(\frac{\partial U_{r_1}}{\partial_{r_1}} + \frac{U_{r_1}}{r_1} + \frac{1}{r_1}\frac{\partial U_{\theta_1}}{\partial \theta_1}\right) + 2\mu\frac{\partial u_{r_1}}{\partial r_1} \tag{2.4.35a}$$

$$\tau_{r_1\theta_1} = \mu\left(\frac{\partial u_{\theta_1}}{\partial r_1} + \frac{u_{\theta_1}}{r_1} + \frac{1}{r_1}\frac{\partial u_{r_1}}{\partial \theta_1}\right) \tag{2.4.35b}$$

This gives for the displacements along the canyon rim $r_1 = b$ and for $-\theta_0 \le \theta \le \theta_0$

$$u_{r_1}\left(b,\theta_1\right) = \frac{1}{b}\begin{bmatrix} C_f ik_{\alpha f} b\cos\left(\theta_1 - \theta_{\alpha f}\right)e^{A_f} + C_s ik_{\alpha s} b\cos\left(\theta_1 - \theta_{\alpha s}\right)e^{A_s} - \\ Dik_{\beta} b\sin\left(\theta_1 - \theta_{\beta}\right)e^{A_\beta} \end{bmatrix} e^{-i\omega t} \tag{2.4.36a}$$

$$u_{\theta_1}\left(b,\theta_1\right) = \frac{1}{b}\begin{bmatrix} -C_f ik_{\alpha f} b\sin\left(\theta_1 - \theta_{\alpha f}\right)e^{A_f} - C_s ik_{\alpha s} b\sin\left(\theta_1 - \theta_{\alpha s}\right)e^{A_s} - \\ Dik_{\beta} b\cos\left(\theta_1 - \theta_{\beta}\right)e^{A_\beta} \end{bmatrix} e^{-i\omega t} \tag{2.4.36b}$$

for the solid,

$$U_{r_1}\left(b,\theta_1\right)=\frac{1}{b}\begin{bmatrix} f_1C_f ik_{\alpha f}b\cos\left(\theta_1-\theta_{\alpha f}\right)e^{A_f}+f_2C_s ik_{\alpha s}b\cos\left(\theta_1-\theta_{\alpha s}\right)e^{A_s}- \\ f_3Dik_\beta b\cos\left(\theta_1-\theta_\beta\right)e^{A_\beta} \end{bmatrix}e^{-i\omega t} \tag{2.4.37a}$$

$$U_{\theta_1}\left(b,\theta_1\right)=\frac{1}{b}\begin{bmatrix} -f_1C_f ik_{\alpha f}b\sin\left(\theta_1-\theta_{\alpha f}\right)e^{A_f}-f_2C_s ik_{\alpha s}b\sin\left(\theta_1-\theta_{\alpha s}\right)e^{A_s}- \\ f_3Dik_\beta b\cos\left(\theta_1-\theta_\beta\right)e^{A_\beta} \end{bmatrix}e^{-i\omega t} \tag{2.4.37b}$$

for the fluid. Similarly, the stresses acting on the solid and on the fluid along the canyon rim are

$$\tau_{r_1r_1}\left(b,\theta_1\right)=\begin{bmatrix} \frac{-2\mu}{b^2}C_f\left(k_{\alpha f}b\right)^2\left[1+\frac{\lambda}{2}+\frac{f_1Q}{2}-\sin^2\left(\theta_1-\theta_{\alpha f}\right)\right]e^{A_f}- \\ \frac{2\mu}{b^2}C_s\left(k_{\alpha s}b\right)^2\left[1+\frac{\lambda}{2}+\frac{f_2Q}{2}-\sin^2\left(\theta_1-\theta_{\alpha s}\right)\right]e^{A_s}+ \\ \frac{2\mu}{b^2}D\left(k_\beta b\right)^2\sin\left(\theta_1-\theta_\beta\right)\cos\left(\theta_1-\theta_\beta\right)e^{A_\beta} \end{bmatrix}e^{-i\omega t} \tag{2.4.38a}$$

$$\tau_{r_1\theta_1}\left(b,\theta_1\right)=\frac{2\mu}{b^2}\begin{bmatrix} C_f\left(k_{\alpha f}b\right)^2\sin\left(\theta_1-\theta_{\alpha f}\right)e^{A_f}+C_s\left(k_{\alpha s}b\right)^2\sin\left(\theta_1-\theta_{\alpha s}\right)e^{A_s}+ \\ D\left(k_\beta b\right)^2\left[\frac{1}{2}-\sin^2\left(\theta_1-\theta_\beta\right)\right]e^{A_\beta} \end{bmatrix}e^{-i\omega t} \tag{2.4.38b}$$

and

$$\sigma\left(b,\theta_1\right)=\frac{1}{b^2}\left[-S_1C_f\left(k_{\alpha f}b\right)^2e^{A_f}-S_2C_s\left(k_{\alpha s}b\right)^2e^{A_s}\right]e^{-i\omega t} \tag{2.4.38c}$$

where

$$A_f=b_{1f}d+ik_{\alpha f}r_1\cos\left(\theta_1-\theta_{\alpha f}\right)$$

$$A_s=b_{1s}d+ik_{\alpha s}r_1\cos\left(\theta_1-\theta_{\alpha s}\right)$$

$$A_\beta=b_2d+ik_\beta r_1\cos\left(\theta_1-\theta_\beta\right)$$

Chapter 3: Numerical Results and Analysis

This chapter presents numerical results for: the wave velocities, free-field motion, foundation input motion, foundation stiffness and damping, and system response in the form of a parametric study, with the objective of understanding the effects of the many model parameters. The following Chapter 6 shows results for a model with properties similar to those for Millikan library, attempting to explain the observed effects.

The results were computed using a FORTRAN computer program SSI_POROUS (Todorovska and Al Rjoub, 2006a), which was generalized to work for a dissipative medium (i.e. for a mixture that has finite permeability and is saturated with viscous fluid), and for partially saturated soils. This generalization required computation of Bessel functions of complex arguments, and subroutines from Zhang and Jin (1996) were used. The computer program was written in terms of dimensionless parameters, defined using as reference: length a, material modulus μ_s, and mass density ρ_{gr}. Then, the system response is a function of the following dimensionless parameters: stiffness of the fluid relative to the skeleton, defined through the ratio K_f / μ_s and the Poisson's ratio ν_s; mass density of the skeleton relative to the fluid, defined through the ratio $\rho_{\mathrm{gr}} / \rho_f$ and the porosity $\hat{n}$; mass of the building relative to the mass of the foundation, and mass of the foundation relative to the mass of the replaced soil, through the ratios $m_{\mathrm{b}} / m_{\mathrm{fnd}}$ and $m_{\mathrm{fnd}} / m_{\mathrm{gr}}$, where, $m_{\mathrm{gr}} = A_{\mathrm{fnd}} \rho_{\mathrm{gr}}$ is the mass of the excavated soil (per unit length) if there were no voids, and A_{fnd} is the area of the foundation; the flexibility of the building relative to that of the soil, through the ratio $\varepsilon = (V_{\mathrm{ref}} H)/(V_{S,\mathrm{b}} a)$

$=\left[(\omega H)/V_{S,\mathrm{b}}\right]/\left[(\omega a)/V_{\mathrm{ref}}\right]$ = ratio of the number of wavelength in the shear beam in length H and the number of reference wavelengths in the soil in length a; dimensionless frequency $\eta=\omega a/(\pi V_{\mathrm{ref}})$, where $V_{\mathrm{ref}}=\sqrt{\mu_s/\rho_{\mathrm{gr}}}$ is a reference velocity; foundation shape, through the ratio h/a; and on the type, amplitude and angle of the incident waves.

3.1 Soil Constitutive Properties and Waves Velocities

The wave velocities in the soil and the frequency of motion are fundamental for significance of the effects of the soil-structure interaction. When the effects of the seepage force are considered, the wave velocities depend themselves on the degree of dissipation and also on frequency. Hence, the analysis begins with understanding how the wave velocities depend on frequency and on the soil permeability (for fixed value of viscosity of the fluid), which will help later on, interpret the results for the foundation stiffness and damping.

3.1.1 Input Model Parameters

The following range of the input parameters was considered in the analysis. The pore fluid in this study is water, which has mass density $\rho_w=10^3$ kg/m^3 and bulk modulus $K_w=2.2\times10^9$ Pa, giving bulk wave velocity $\sqrt{K_w/\rho_w}$ =1,483 m/s. For full saturation, $K_f=K_w$ and $\rho_f=\rho_w$. For the mass density of the material of which the grain is made value $\rho_{\mathrm{gr}}=2.7\times10^3$ kg/m^3 was used. The ratio μ/K_f, where $K_f=K_w$ describes the stiffness of the skeleton, which is varied so that μ/K_f = 0.01, 0.1, 1, and 10. The value μ/K_f = 0.01 corresponds to soft soil, μ/K_f = 0.1 to stiff soil, and μ/K_f = 1 and 10 to porous rock (Lin et al., 2001). Only one value of Poisson ratio is considered, ν_s=0.3, and two values of porosity, $\hat{n}$=0.3 and 0.4, which are representative for soils. The dissipation depends on the ratio $\hat{\mu}/\hat{k}$, where $\hat{\mu}$ is the absolute viscosity of the fluid, and $\hat{k}$ is the intrinsic permeability of the skeleton. The absolute viscosity of water at about $25\,^{\circ}\mathrm{C}$ is $\hat{\mu}_w = 0.89\times10^{-3}$ $\mathrm{Pa}\cdot\mathrm{s}$ ($1\,\mathrm{Pa}\cdot\mathrm{s}=1\,\mathrm{N\,s/m^2}$). In this work, a rounded value $\hat{\mu} = \hat{\mu}_w = 10^{-3}$ $\mathrm{N\,s/m^2}$ is used. The intrinsic permeability of the skeleton depends on the type of geologic material. Pervious consolidated geo materials, such as highly fractured rock, and pervious unconsolidated geo materials such as well-sorted gravel and well-sorted sand and gravel, have intrinsic permeability $\hat{k}$ in the range $10^{-6} - 10^{-10}$ m^2. Semi-pervious consolidated geo materials, such as oil reservoir rocks and fresh sandstone, and semi-pervious unconsolidated geo materials, such as very find sand, silt, loess and loam, have $\hat{k}$ in the range $10^{-11} - 10^{-14}$ m^2 (Bear, 1972). Geo materials with $\hat{k}$ in the range $10^{-15} - 10^{-19}$ m^2 are considered to be impervious. In this work, results are shown for $10^{-12} \le \hat{k} \le 10^{-6}$, and also for the case when the effects of the dissipative force are neglected, and the wave velocities are real values (this case is referred to as the "no seepage force" or the "$\hat{k} \to \infty$" case). For dry soil (pores filled with air), the following values are taken: $\rho_{\mathrm{gr}}/\rho_f$=0.001 and K_f/μ_s=0.001, and the dry shear wave velocity is computed as $V_{S,\mathrm{dry}} = \sqrt{\mu_s/[(1-\hat{n})\rho_{\mathrm{gr}}]}$. Another variable of the model is the frequency of motion.

The upper bound of frequency is constrained by the requirements that: (1) the flow of the fluid in the pores is laminar, and (2) the wavelengths are much larger than the size of the pores. The first requirement implies frequency bound $f_t = \dfrac{\pi \hat{\nu}}{4d^2}$, where d is the diameter of the pores, and $\hat{\nu}$ is the kinematic viscosity, which is related to the dynamic viscosity $\hat{\mu}$ and fluid density ρ_f by $\hat{\nu} = \hat{\mu} / \rho_f$ (Biot, 1956a). This implies maximum frequencies $f_t = 10,000$ Hz for $d = 0.01$ mm (silt), $f_t = 100$ Hz for $d = 0.1$ mm (sands), and $f_t = 10$ Hz for $d = 1$ mm (coarse sands to gravel). We consider frequencies not larger than 100 Hz in presenting results for the wave velocities and free-field motions, and dimensionless frequency $\eta \le 5$, where $\eta = \omega a / (\pi V_{\mathrm{ref}}) = (2a) f / V_{\mathrm{ref}}$, and $V_{\mathrm{ref}} = V_{\mathrm{S,dry}}$, and $2a$ is the characteristic dimension for the wave scattering problem and radiation problem. Then for the softest soils considered (μ / K_f =0.01), for which the smallest wave velocity is of the order of 100 m/s, and for $2a$=24 m, which is the value used for the case study (Millikan library), the maximum value of $\eta = 5$ implies highest frequency $f = 20$ Hz, which is low enough for the flow to be laminar.

3.1.2 Wave Velocities for Full Saturation as Function of the Model Parameters

For very small $\dfrac{1}{\omega} \dfrac{\hat{n} \hat{\mu}}{\hat{k}}$, which has dimension of mass density, the seepage force is much smaller than the inertial forces, and its effects are negligible (see eqns (2.2.7c,d)). In that case, the wave velocities are real valued, do not depend on frequency, and are used in this section as reference in showing how much the wave velocities change as result of the seepage force. Table 3.1.1 shows these frequency independent velocities for different combinations of all other input parameters. The S and P –wave velocity of the dry solid is also shown, used as reference in studying the effects of saturation.

Table 3.1.1 Wave velocities for fully saturated soil for the case of no seepage force.

μ / K_f	ν_s	$\hat{n}$	$V_{\mathrm{S,dry}}$ [m/s]	$V_{\mathrm{P,dry}}$ [m/s]	V_{S} [m/s]	V_{Pf} [m/s]	V_{Ps} [m/s]
0.01	0.3	0.3	107.9	201.9	103.6	1,922.4	101.5
0.1	0.3	0.3	314.2	638.5	327.5	1,986.8	310.7
1.0	0.3	0.3	1,078.9	2,018.9	1,033.6	2,620.5	745.0
10.0	0.3	0.3	3,411.8	6,384.6	3,274.7	6,344.7	973.0
0.01	0.3	0.4	116.5	218.1	110.8	1,763.5	131.8
0.1	0.3	0.4	368.5	689.5	350.4	1,831.1	401.5
1.0	0.3	0.4	1,165.3	2,180.4	1,108.2	2,561.0	907.7
10.0	0.3	0.4	3,685.1	6,894.9	3,504.4	6,697.9	1,097.5

Figure 3.1.1 shows the variation of the normalized wave velocities with inverse permeability $1/K$, which is proportional to the seepage force. In this one and all other figures, $K \equiv \hat{k}$, $n \equiv \hat{n}$, the wave velocities are normalized by their respective value for no seepage force ($\frac{1}{\omega}\frac{\hat{n}\hat{\mu}}{\hat{k}}$=0, see Table 3.1.1), and the real parts of the wave velocities are shown on the left hand side, and the imaginary parts are shown on the right hand. In this figure, the different curves correspond to different values of μ / K_f, and the porosity is

$\hat{n} = 0.4$. Parts a) and b) differ in that in part a) all the results are for same absolute frequency, set to $f = 1$ Hz, while in part b), all the results are for same relative frequency, which is the dimensionless frequency set to $\eta = \omega a/(\pi V_{S,\mathrm{dry}})$ set to $\eta = 1$, where the reference length $a = 12$ m. Because $V_{S,\mathrm{dry}}$ is different for each μ / K_f (see

Table 3.1.1), the absolute frequency is different for the different values of μ / K_f, having values $f = 3.76$, 11.9, 37.6 and 118.9 Hz for μ / K_f = 0.01, 0.1, 1 and 10. Part b) is shown because the effects of scattering and radiation depend on the dimensionless frequency rather than on the absolute frequency. The results in Fig. 3.1.1 show that the velocities vary significantly only within a band of values of permeability. Outside this band, they rapidly approach their asymptotic values, which are real valued. The velocity of the fast P-wave is affected little by the seepage force, decreasing only by up to about 5%. The velocity of the slow P-wave is affected most by the seepage force, decreasing to zero for very large seepage force. The velocity of the S-waves reduces by up to about 40% of its value for zero seepage force. A comparison of the results in parts a) and b) shows that, for fixed permeability and *absolute* frequency f, the *change* of the wave velocities with permeability does *not* depend on the relative stiffness of the skeleton, although their absolute values are very much dependent on the relative stiffness of the skeleton (see Table 3.1.1). For fixed relative frequency, $\eta = \omega a/(\pi V_{S,\mathrm{dry}})$, the change of the wave velocities is similar but occurs within a different range of values of $1/K$. The change starts to become significant for smaller permeability for materials with stiffer skeleton.

a)

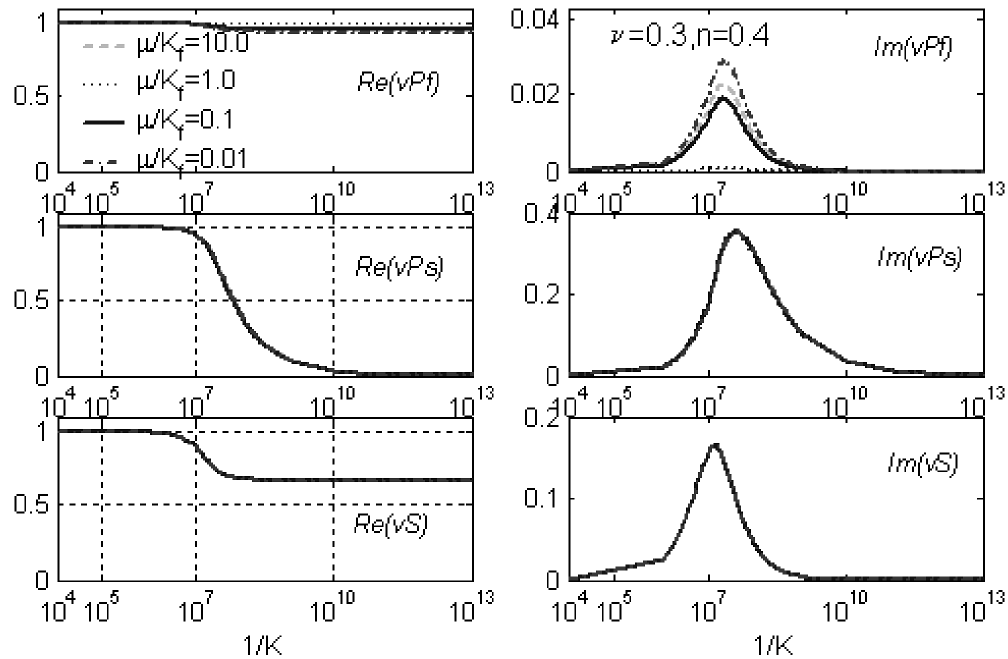

b)

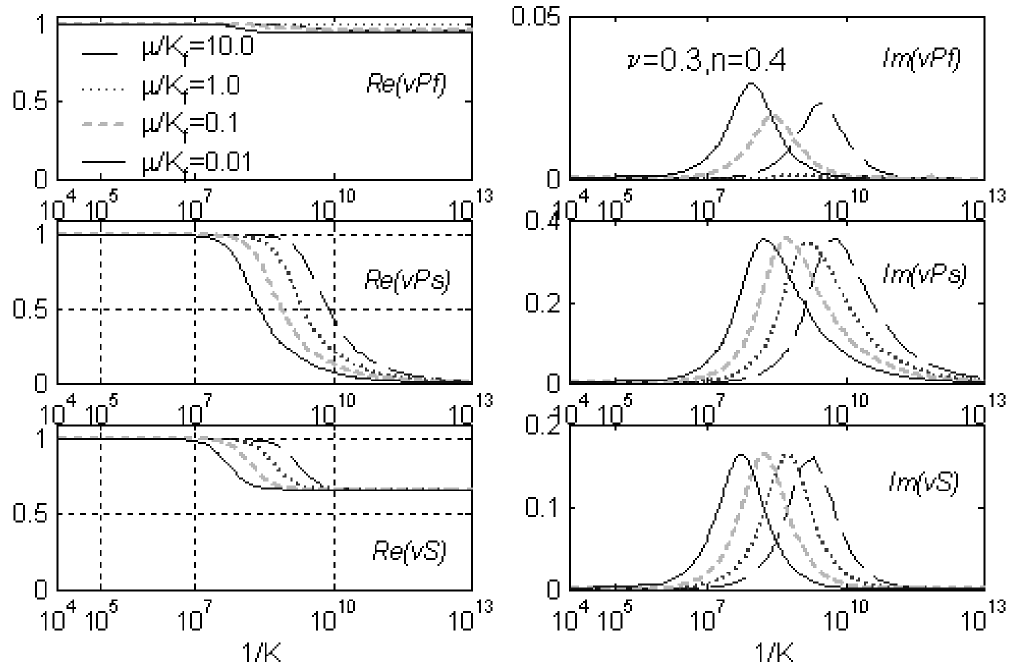

Fig. 3.1.1 Normalized wave velocities of the mixture versus inverse permeability for different values of μ / K_f, and for porosity $\hat{n} =$ 0.4. In part a), the absolute frequency is set to $f = 1$ Hz, and in part b) the relative frequency is set to $\eta = \omega a / (\pi V_{S,\mathrm{dry}}) = 1$, where the reference length $a = 12$ m.

Figure 3.1.2 also shows the variation of the normalized wave velocities with inverse permeability $1/K$, but the different curves correspond to different values of frequency $f = 0.1$, 1, 10 and 100 Hz. In part a), μ / K_f =0.1 (stiff soil), in part b) μ / K_f =0.01 (soft soil), and in both parts the porosity is $\hat{n} =$ 0.4. It can be seen from this figure that, for smaller frequencies of motion, the seepage force starts to affect the wave velocities at smaller $1/K$, i.e. at higher permeability. This trend is as expected, because the effect of the seepage force is through the combination $\hat{n}\hat{\mu}/(\omega\hat{k})$.

Fig. 3.1.3 shows the normalized wave velocities versus frequency f in Hz on a logarithmic scale for different values of inverse permeability $1/K$. As in Fig. 3.1.2, in part a), μ / K_f =0.1 (stiff soil), in part b) μ / K_f =0.01 (soft soil), and in both parts the porosity is $\hat{n} =$ 0.4. It can be seen that the trend of the variation of the normalized wave velocities with increasing frequency is the same as the trend with increasing permeability (see Fig. 3.1.2), which is due to the fact that in Biot's theory, the effect of the seepage force is through the ratio $\hat{n}\hat{\mu}/(\omega\hat{k})$.

a)

b)

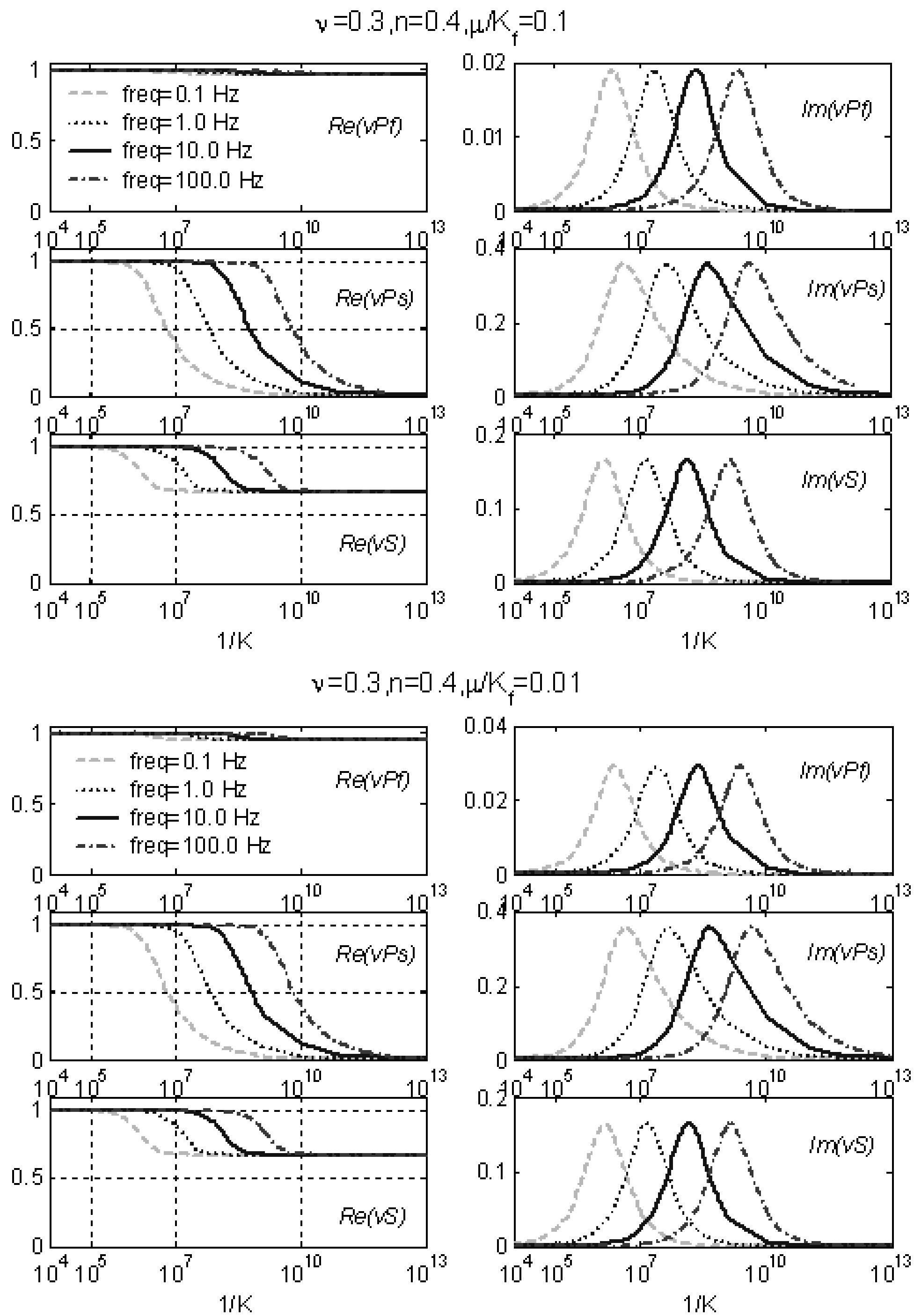

Fig. 3.1.2 Normalized wave velocities of the mixture versus inverse permeability for different values of frequency, $f = 0.1$, 1, 10 and 100 Hz. The porosity is $\hat{n} = 0.4$, and μ/K_{f} =0.1 (part a) and 0.01 (part b).

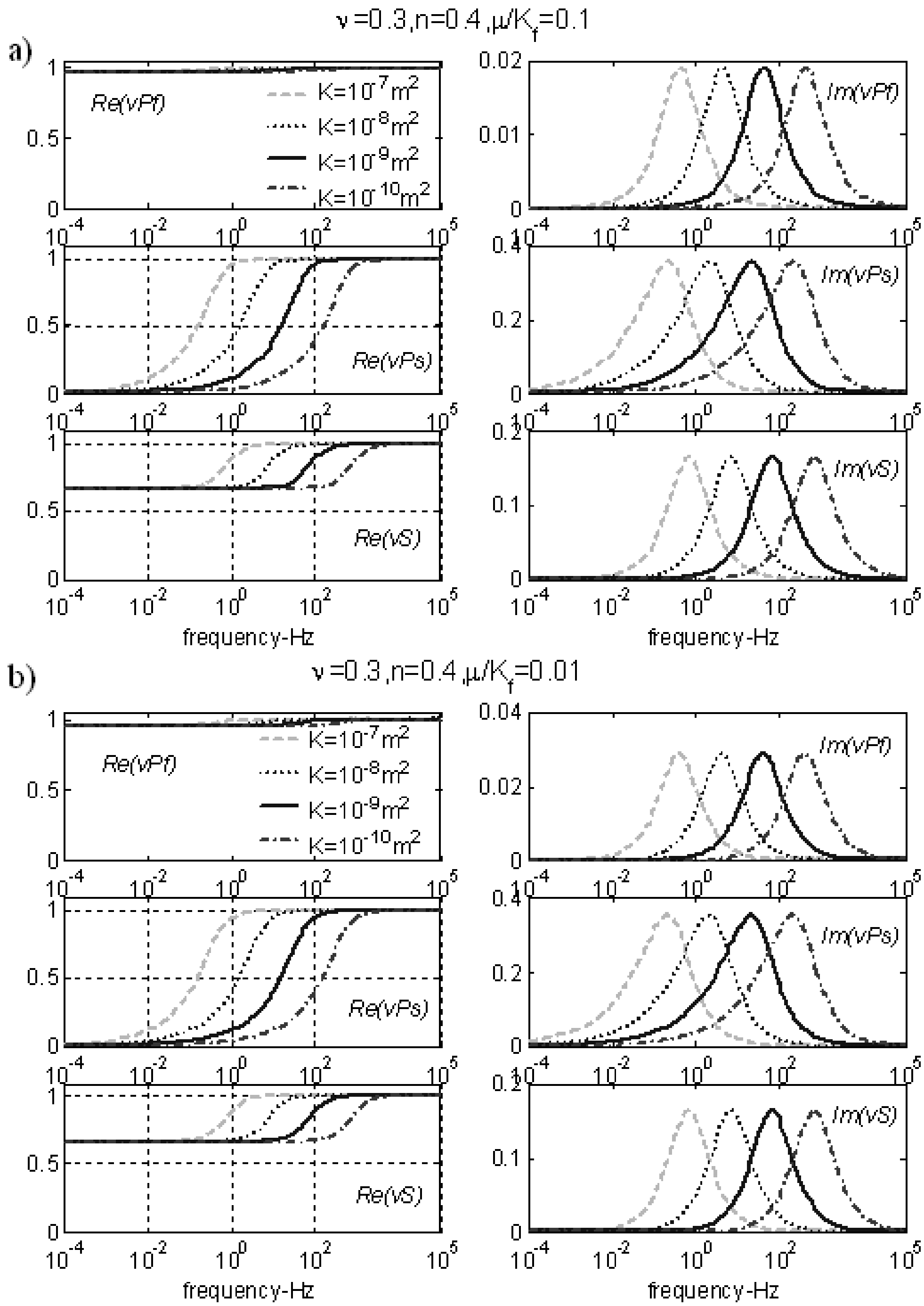

Fig. 3.1-3 Normalized wave velocities versus frequency for different values of permeability. The porosity is $\hat{n} = 0.4$, and μ/K_{f}=0.1 (part a) and 0.01 (part b).

3.1.3 The Effect of Partial Saturation on the Wave Velocities

This section illustrates the variation of the wave velocities of the mixture as function of the degree of saturation, accounted for as described in Section 2.2.3. Fig. 3.1.4 shows the variation of the adjusted bulk modulus of the fluid, $K_f \le K_w$, plotted on a logarithmic scale, as function of the fraction of air in the pores, $1-S_r$, where S_r is the saturation (ratio of the volume of the pore water and the volume of the pores). The different curves correspond to different values of the absolute pore pressure (P_a in eqn (2.2.20)), which takes values 0.2, 0.6 and 1 MPa. It can be seen that the modified bulk modulus reduces rapidly as the saturation becomes partial even for very small fraction of air. Fig. 3.1.5 shows the variation of the modulus of the (complex) velocities of the fast and slow P-wave versus $1-S_r$, for porosity $\hat{n}=0.4$, and $\mu / K_w = 0.01$ (soft soil). It can be seen that both wave velocities decrease rapidly with increasing fraction of air content, the velocity of the fast P-wave approaching the P-was velocity in the dry solid (about 200 m/s, see Table 3.1.1), and the velocity of the slow P-wave approaching zero. In this model, which is used only for very high degrees of saturation ($S_r > 90\%$), the effects of the saturation on the mass densities is ignored, and hence, the shear wave velocity does not depend on the degree of saturation.

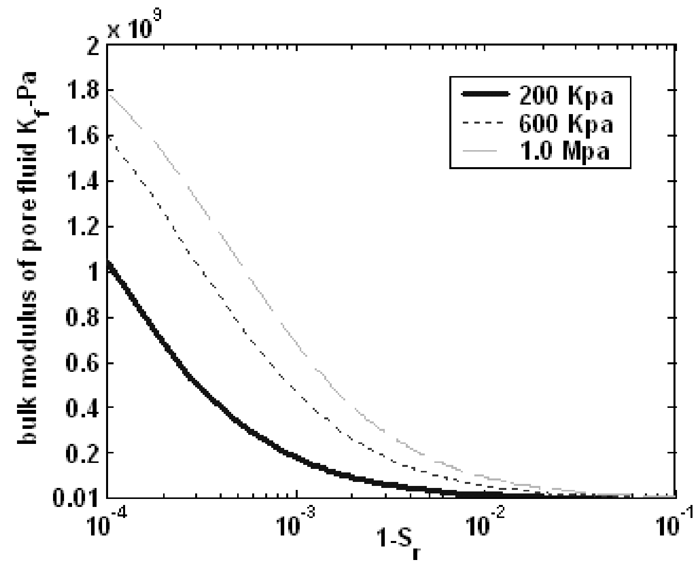

Fig. 3.1.4 Modified bulk modulus of the pore fluid versus fraction of air, $1-S_r$.

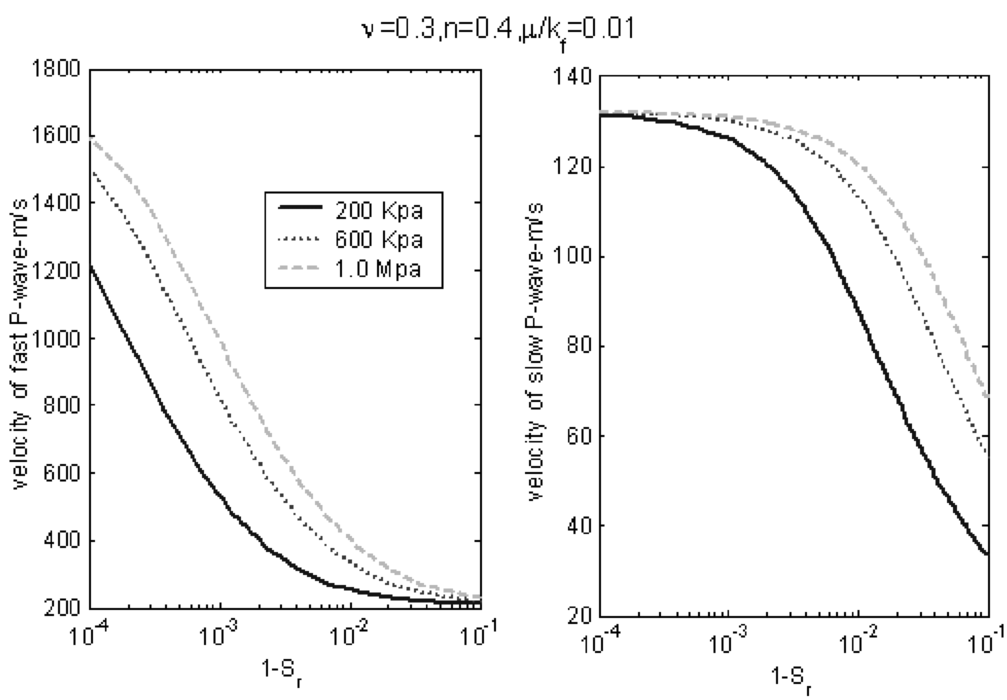

Fig. 3.1.5 Modified velocities of fast and slow P-waves versus fraction of air, $1-S_r$, for porosity $\hat{n}=0.4$ and $\mu/K_w=0.01$ (soft soil).

3.2 Foundation Complex Stiffness Matrix

This section shows results for the real and imaginary part of the foundation impedance matrix, where the real part describes the foundation stiffness, and the imaginary part is related to the damping due to radiation of energy from a vibrating foundation. Section 3.2.1 shows results for fully saturated soils, and Section 3.2.2 for partially saturated soils. In all figures, the Poisson's ratio is $\nu = 0.3$, the porosity is $\hat{n} = 0.4$, and the dimensionless frequency is defined with respect to the shear wave velocity of the dry solid, $\eta = \dfrac{\omega a}{\pi V_{s,dry}}$, which is independent of the state of saturation. Results are shown only for "stiff" and "soft" soils, i.e. for $\mu / K_f = 0.1$ and 0.01, because the effects of the pore water are more significant for solids with relatively soft skeleton.

3.2.1 Foundation Complex Stiffness Matrix for Fully Saturated Soils

Figure 3.2.1 shows results for $\mu / K_f = 0.1$, for different values of permeability. Part a) shows results for permeable (open) foundation-soil interface, and part b) for impermeable (sealed) interface. It is noted here that the hydraulic condition on the half-space surface does not affect the results, as the effect of the free surface on the scattered waves from the foundation was neglected in the development of the model. In each part, the plots on the left show the real part and those on the right show the imaginary part of the corresponding foundation stiffness matrix coefficient, and the three rows of plots show respectively $K_{11} = K_{22}$ (horizontal and vertical stiffness which are equal for this model for a semi-circular foundation), K_{33} (rocking stiffness), and K_{23} (coupling term

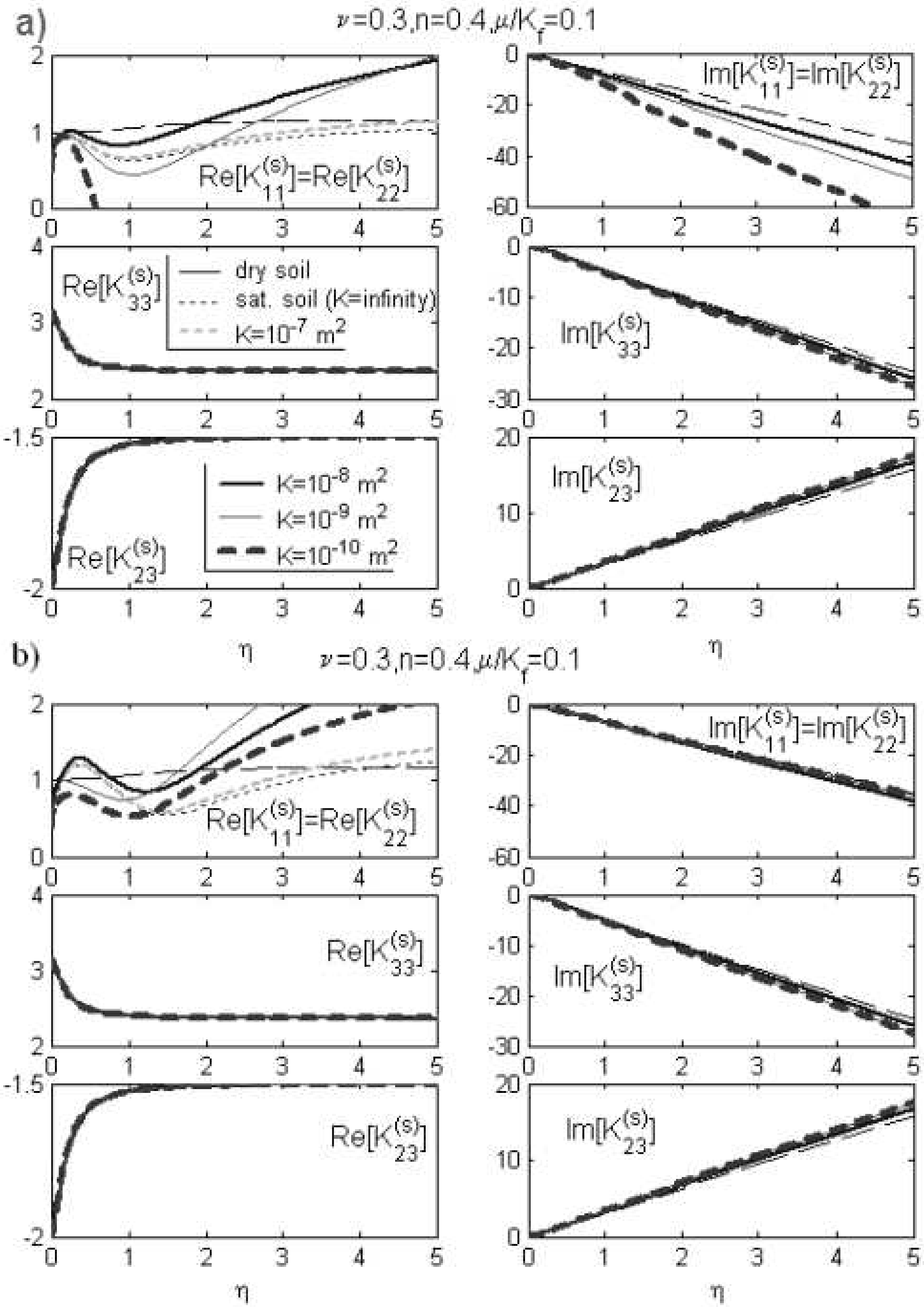

Fig. 3.2.1 Foundation dynamic stiffness coefficients for different values of skeleton permeability, and for porosity $\hat{n} = 0.4$ and $\mu / K_f = 0.1$. Pat a) shows results for permeable (open), and part b) for impermeable (sealed) contact surface.

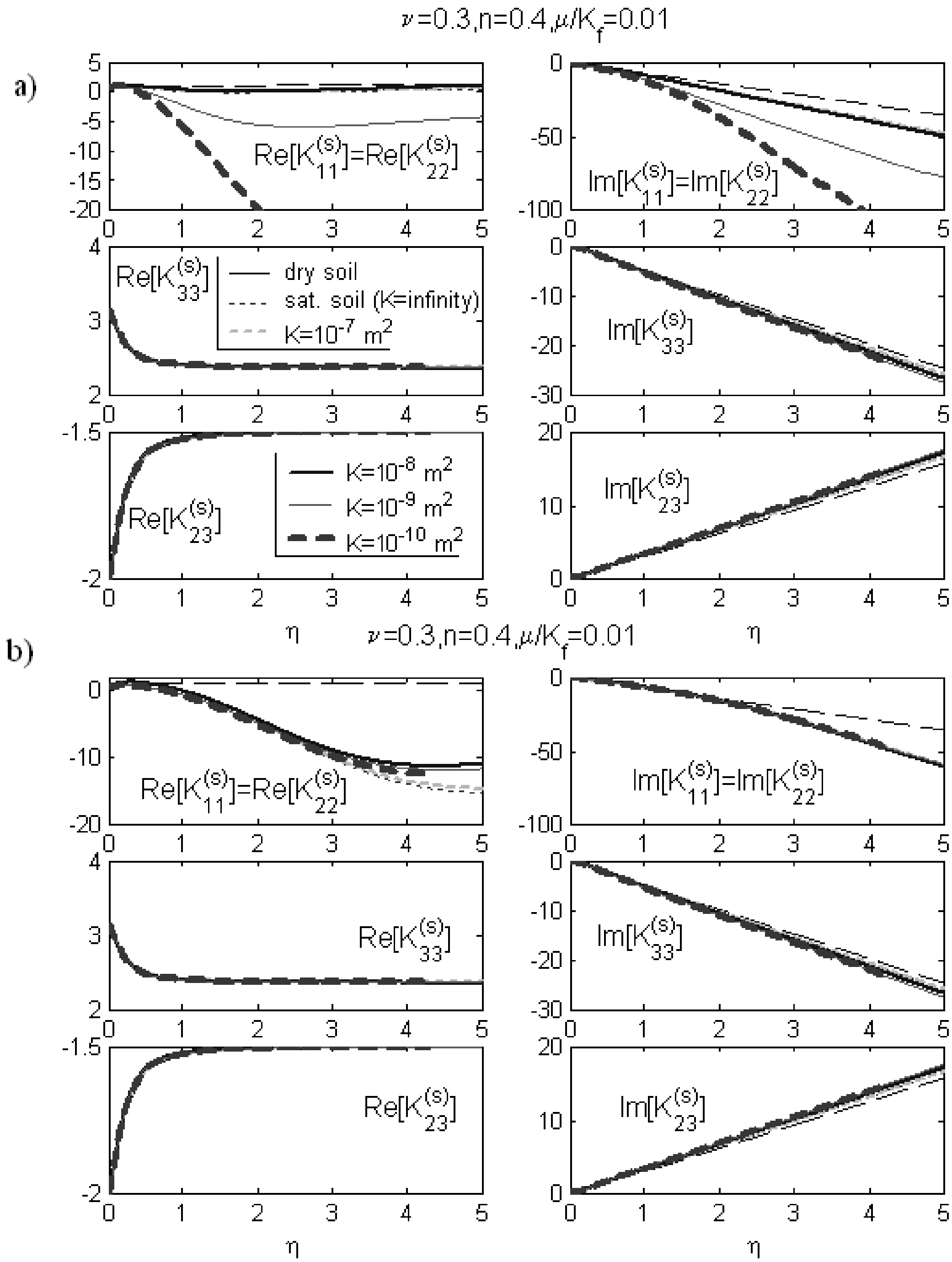

Fig. 3.2.2 Foundation dynamic stiffness coefficients for different values of skeleton permeability, and for porosity $\hat{n} = 0.4$ and $\mu / K_f = 0.01$. Pat a) shows results for permeable (open), and part b) for impermeable (sealed) contact surface.

between horizontal and rocking motions). Similarly, Fig. 3.2.2 shows results for $\mu / K_f = 0.01$ (soft soil). The results are discussed in what follows.

A noted in Todorovska and Al Rjoub (2006b) the effect of saturation for this shape of embedded foundation is such that it affects significantly both the horizontal and the vertical stiffness, while the effect on the rocking and coupling stiffness coefficients is very small. This can be explained by the fact that the rocking motion of the foundation results only in shear deformations in the soil and motion of soil tangent to the contact surface, which does not cause flow of fluid perpendicular to the foundation-soil interface (hence pressure from the fluid onto the foundation). What is different in this thesis from the study in Todorovska and Al Rjoub (2006b) is that the effects of the seepage force are considered, which, as noted in Section 3.1 lead to complex valued wave velocities in the soil, and also the effects of partial saturation. Hence, in this thesis work, the emphasis is on analyzing the effects of finite permeability and partial saturation.

Todorovska and Al Rjoub (2006b) explained the trend of the effect of the pore water as increasing the stiffness of the foundation for small frequencies for which the water moves in phase with the solid, but the effects reverses for high enough frequency, when the pore water moves in the opposite direction of the solid, and it reduces the foundation stiffness. For very stiff skeleton (e.g. rock) the effect is very small, while for some very soft soils, the window of frequencies where there would be an increase of stiffness may be very small for the increase to be noticeable. The presence of a dissipative force is expected to increase the dynamic stiffness of the foundation. Figures 3.2.1 and 3.2.2 shows that the horizontal and vertical stiffness (real part of $K_{11} = K_{22}$) do increase with decreasing permeability (i.e. with increasing seepage force), but only up to a certain value of permeability. For smaller permeability than that value, the foundation stiffness *decreases with further decrease of permeability*, but *only for smaller* η, and for large enough η it exceeds the stiffness for larger values of permeability. This change in the trend can be explained by the dependency of the wave velocities both on frequency and permeability.

To observe better and explain these effects, the next four figures, 3.2.3 through 3.2.6, show in part a) enlarged plots of $K_{11}= K_{22}$ versus η from Figs 3.2.1 and 3.2.2, and in part b) they show the variation of the wave velocities with dimensionless frequency η. Again, the real parts of both complex stiffness coefficients and velocities are shown on the left hand side, and the imaginary parts are shown on the right hand side. Figures 2.2.3 and 2.2.4 show results for $\mu / K_f = 0.1$, respectively for permeable and impermeable soil-foundation interface. Figures 2.2.5 and 2.2.6 show the same cases and quantities but for $\mu / K_f = 0.01$. It can be seen from these figures that, for fixed frequency, the wave velocities are larger for more permeable materials. For given permeability, the wave velocities increase with increasing η, and their value and rate of the increase are different in different frequency intervals. For higher permeability, the wave velocities reach their high frequency asymptote, which is their value for zero seepage force. Hence, for saturated realistic soils (with finite permeability and nonzero viscosity) and for the frequencies of interest in earthquake engineering, the variation of the foundation stiffness with frequency is governed by two competing mechanisms, one through the flow of fluid through the pores which affects the wave velocities, and the other one via the associated wave phenomena (scattering and diffraction), which depend on the relative size of the foundation and the wavelength of the incident waves.

A comparison of the foundation stiffness for different hydraulic condition at the interface shows that, for smaller η, when the pore water moves in phase or nearly in phase with the skeleton, it's the *stiffening is larger for an impermeable foundation* than for permeable one. For the foundation damping it is the opposite – *the damping is larger a permeable foundation*, and it is larger for less permeable soils. The foundation damping is also larger for softer soils than for stiff soil.

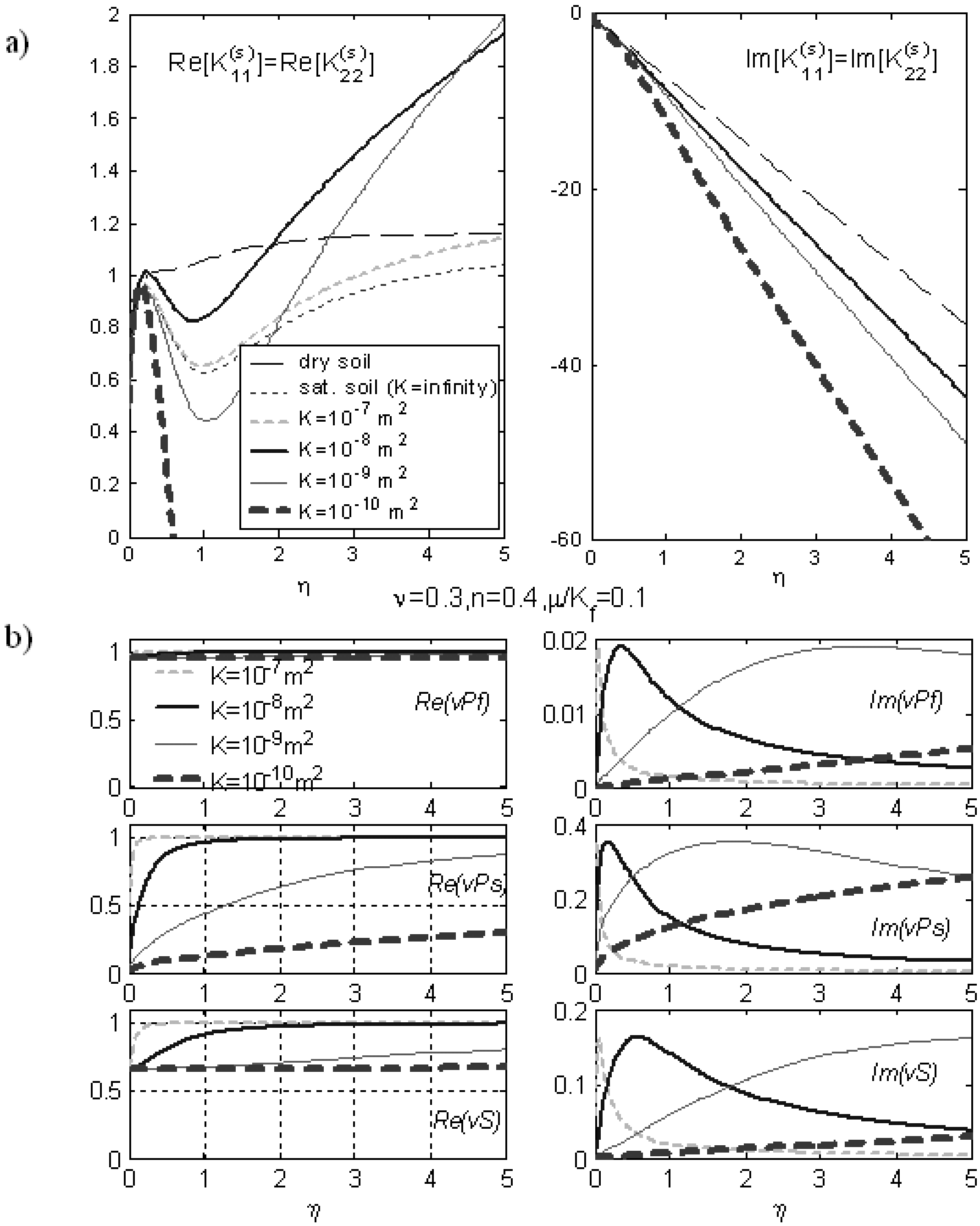

Fig. 3.2.3 Comparison of variations of horizontal/vertical foundation complex stiffness (part a)) and variations of the complex wave velocities (part b)) with dimensionless frequency eta for different values of permeability, for porosity $\hat{n} = 0.4$ and $\mu / K_f = 0.1$, and for p ermeable (open) contact surface.

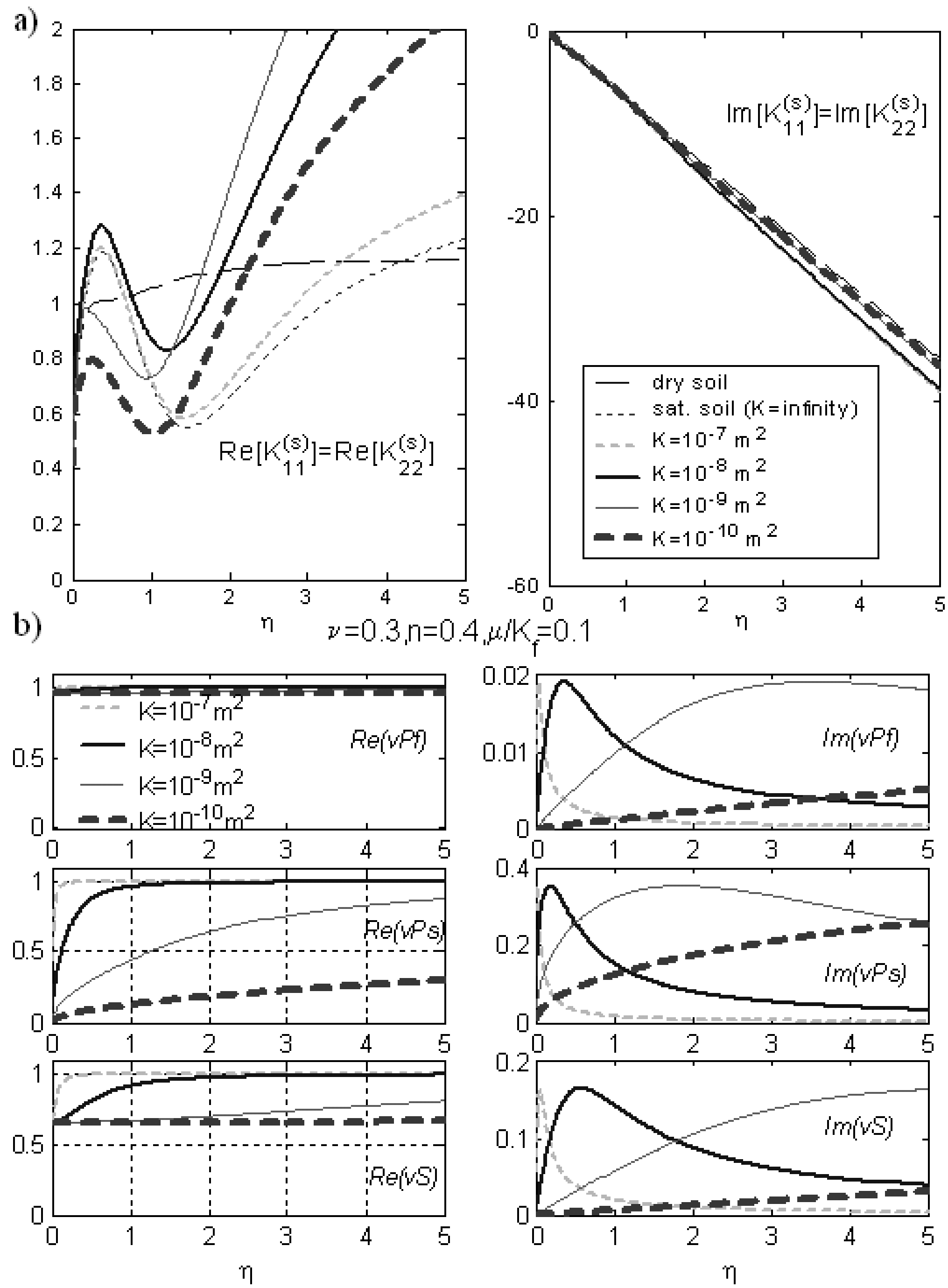

Fig. 3.2.4 Same as Fig. 3.2.3 but for impermeable (sealed) contact surface.

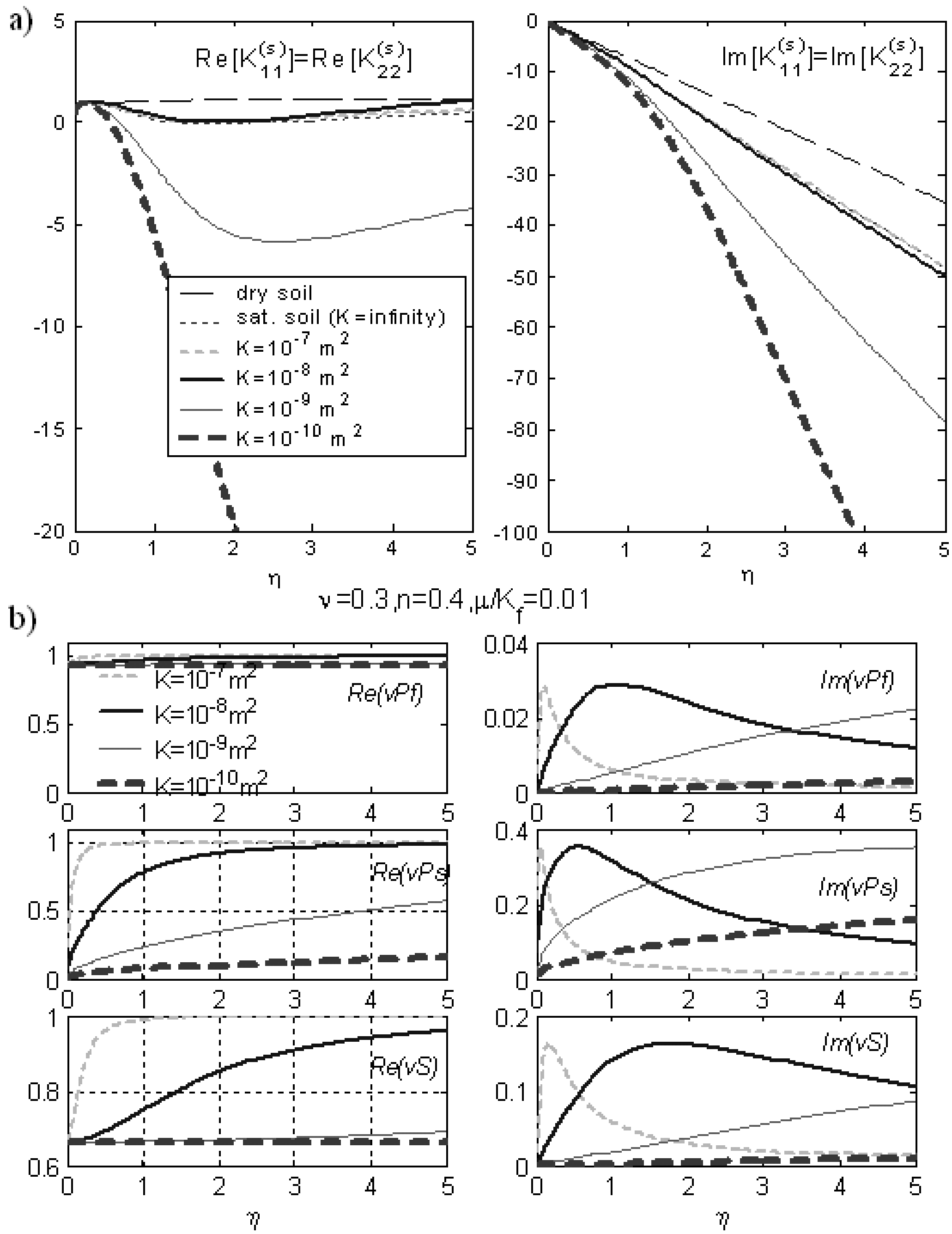

Fig. 3.2.5 Comparison of variations of horizontal/vertical foundation complex stiffness (part a)) and variations of the complex wave velocities (part b)) with dimensionless frequency eta for different values of permeability, for porosity $\hat{n} = 0.4$ and $\mu / K_f = 0.01$, and for permeable (open) contact surface.

a)

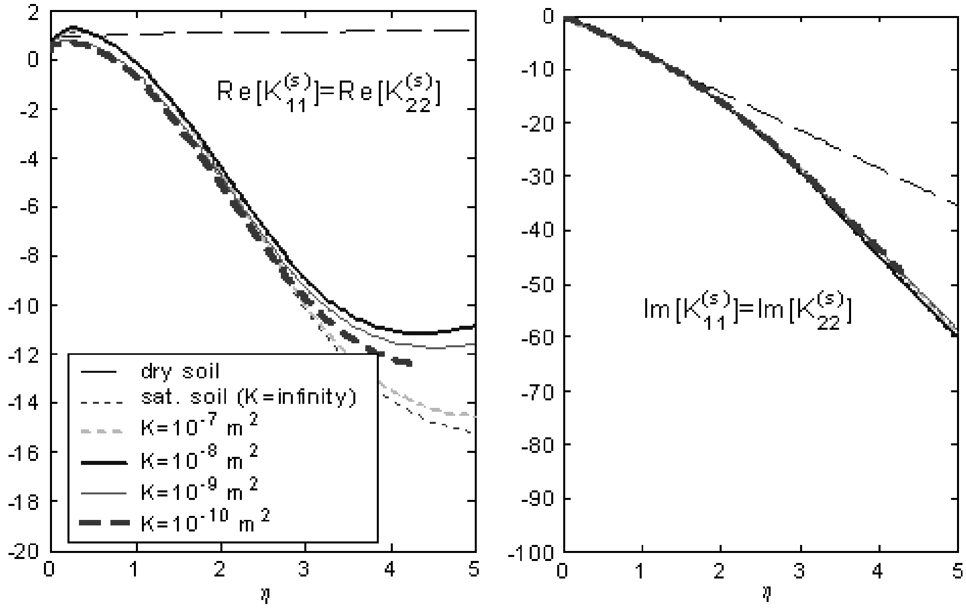

b)

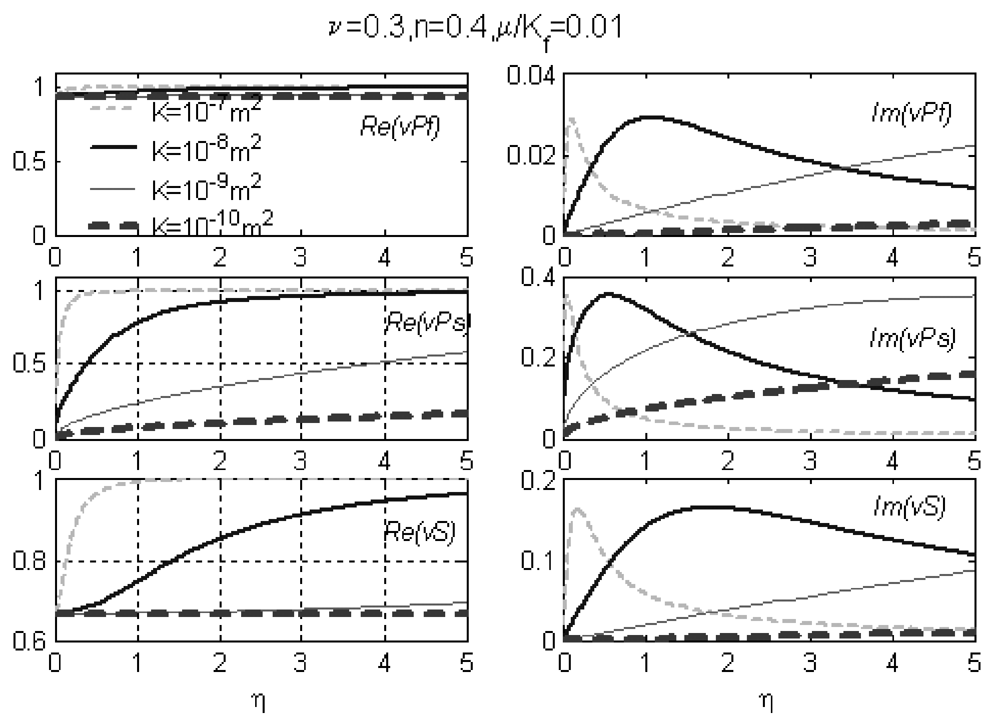

Fig. 3.2.6 Same as Fig. 3.2.5 but for impermeable (sealed) contact surface.

3.2.2 Foundation Complex Stiffness Matrix for Partially Saturated Soils

Figures 3.2.7 and 3.2.8 show results for partially saturated stiff and soft soil respectively ($\mu / K_f = 0.1$ and 0.01). The different curves correspond to dry soil, fully saturated soil and partially saturated soil with saturation $S_r = 99\%$ and 90%. It can be seen that the results for the partially saturate soils are very close to those for dry soil even for such high saturation ratios.

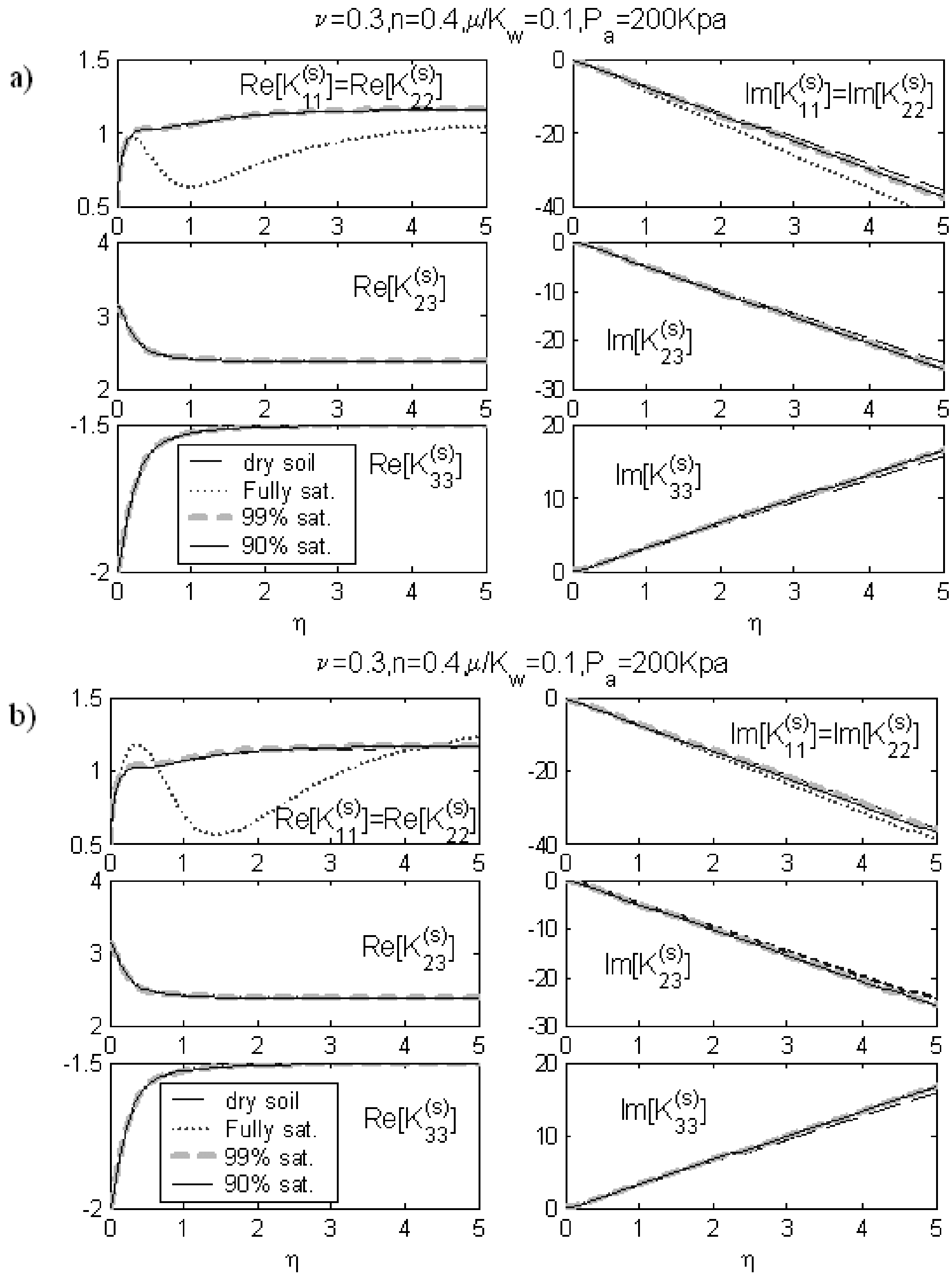

Fig. 3.2.7 Effect of degree of saturation on the foundation complex stiffness for porosity $\hat{n} = 0.4$ and $\mu / K_w = 0.1$, and for permeable (open, part a)) and impermeable (sealed, part b)) contact surface.

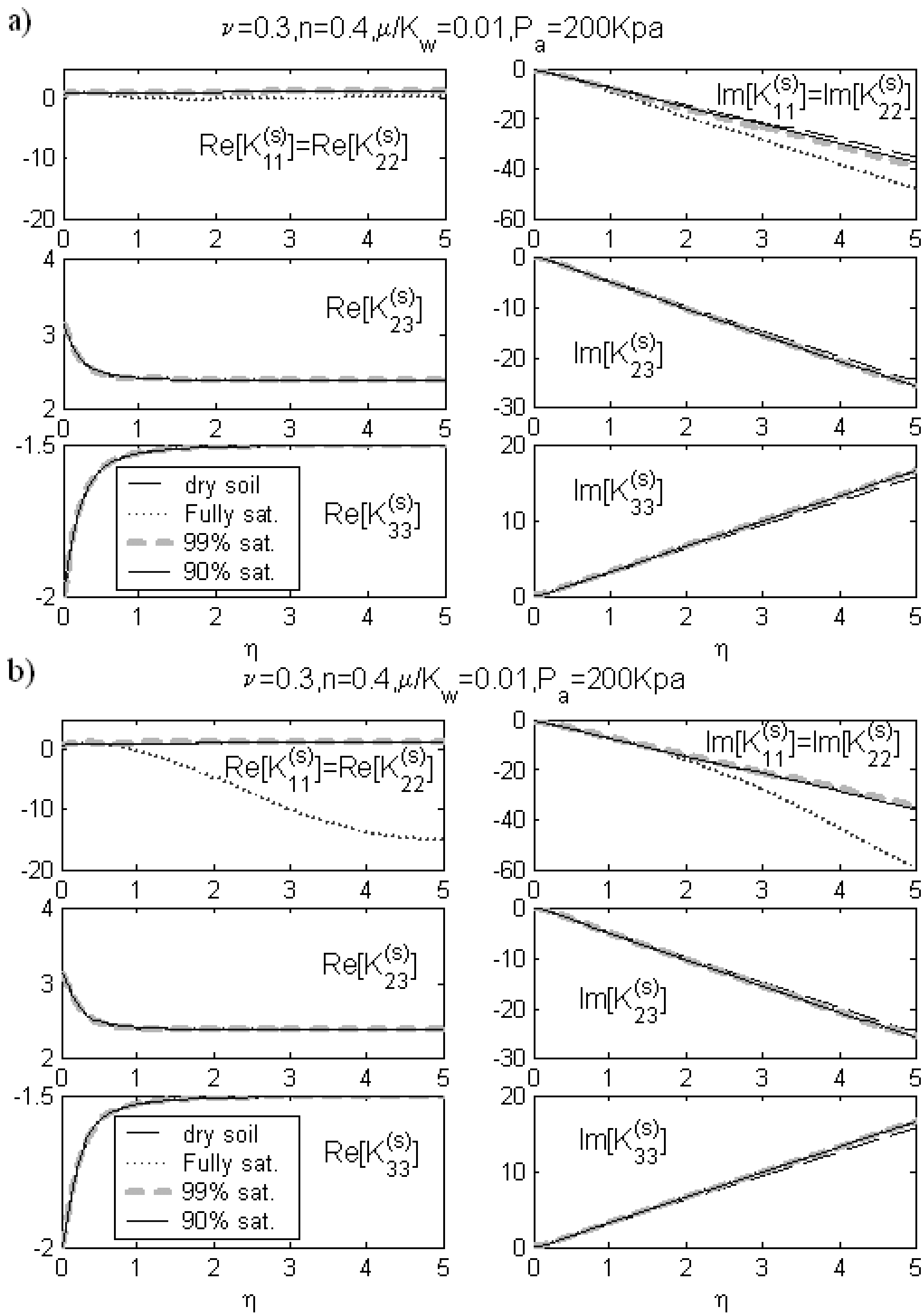

Fig. 3.2.8 Same as Fig. 3.2.7 but for $\hat{n} = 0.4$ and $\mu / K_w = 0.01$.

3.3 Free-Field Motion

Free-field motion is the motion of the half-space not affected by the presence of structures. It is of interest for the problem analyzed in this thesis because it represents the excitation of the soil-structure system. This motion is modified by the scattering of waves from the soil-foundation interface, and radiation of waves by the vibrating foundation. Its modification due to scattering only is referred to as foundation input motion, which asymptotically approaches the free-field motion for wavelengths much longer than the size of the foundation. Hence, understanding of the free-field motion helps understand the foundation input motion. In what follows, results are shown for the free-field motion on the surface of a porous half-space that is fully or partially saturated, and due to incident plane fast P-wave and incident plane SV-wave. Incident slow P-wave is not considered because it attenuates very fast, and hence is not likely to be a carrier of any significant energy from the earthquake source. Locally generated slow P-waves, however, are considered. The results are presented in the form of the magnitudes of the (complex) coefficients of the reflected waves from the half-space surface, and the magnitudes of the (complex) horizontal and vertical displacements on the surface of the half-space. In all the results presented in this section, the Poisson's ratio is $\nu = 0.3$ and the porosity is $\hat{n} = 0.4$.

3.3.1 Incident Plane Fast P-wave

3.3.1.1 Incident P-wave and Fully Saturated Soil

Figures 3.3.1.1 and 3.3.1.2 show variations of the reflection coefficients' amplitudes (left) and surface displacement amplitudes (right) due to an incident plane fast P-wave with unit displacement amplitude, versus the angle of incidence, for different values of permeability $\hat{k} = 10^{-6}$, 10^{-8} and 10^{-10} m^2. The case when the effects of the seepage force are neglected is also shown, as the case $\hat{k} \to \infty$, as well as the dry soil case. These two figures differ in the stiffness of the skeleton. In Fig. 3.3.1.1 $\mu / K_f = 0.1$ (stiff soil) and in Fig. 3.3.1.2 $\mu / K_f = 0.01$ (soft soil). Parts a) and b) differ in the hydraulic boundary condition at the surface. Part a) corresponds to a permeable half-space and part b) to an impermeable half-space. The frequency is set to $f = 1$ Hz.

The results in Figs 3.3.1.1 and 3.3.1.2 show that, at $f = 1$ Hz, the horizontal displacements of the saturated soil decrease with decreasing permeability, are affected very little by the type of hydraulic boundary conditions, and are always and significantly smaller than those of the dry soil. The vertical displacements for permeable half-space are practically not affected by the saturation for all values of permeability considered. For impermeable half-space, vertical displacements are larger for saturated soil, and decrease with decreasing permeability, approaching the dry soil displacements. The difference is the largest for vertical incidence.

Figs 3.3.1.3 and 3.3.1.4 also show variations of the reflection coefficients' amplitudes and surface displacement amplitudes due to an incident plane fast P-wave with unit displacement amplitude, versus the angle of incidence, but for different values of frequency $f = 0.1$, 1, 10 and 100 Hz. The case when there is no seepage force is also shown. In both figures, $\mu / K_f = 0.01$ (soft soil), and they differ only in the value of permeability. In Fig. 3.3.1.3 $\hat{k} = 10^{-7}\mathrm{m}^2$ and in Fig. 3.3.1.4 $\hat{k} = 10^{-10}\mathrm{m}^2$. Figure 3.3.1.3 shows that, for (larger) permeability of $\hat{k} = 10^{-7}\mathrm{m}^2$, the horizontal surface displacements are the smallest for $f = 0.1$, and they approach their values for no seepage force as the frequency increases. Figure 3.3.1.4 shows that, for less permeable soils, with permeability of $\hat{k} = 10^{-10}\mathrm{m}^2$, the horizontal displacements are considerably smaller for the cases with finite permeability, then for the "no seepage force" case, even for $f = 100$ Hz. The vertical displacements, for permeable half-space, vary insignificantly with frequency (for the range considered) and are practically the same as for the "no seepage force" case even for the less permeable soil ($\hat{k} = 10^{-10}\mathrm{m}^2$).

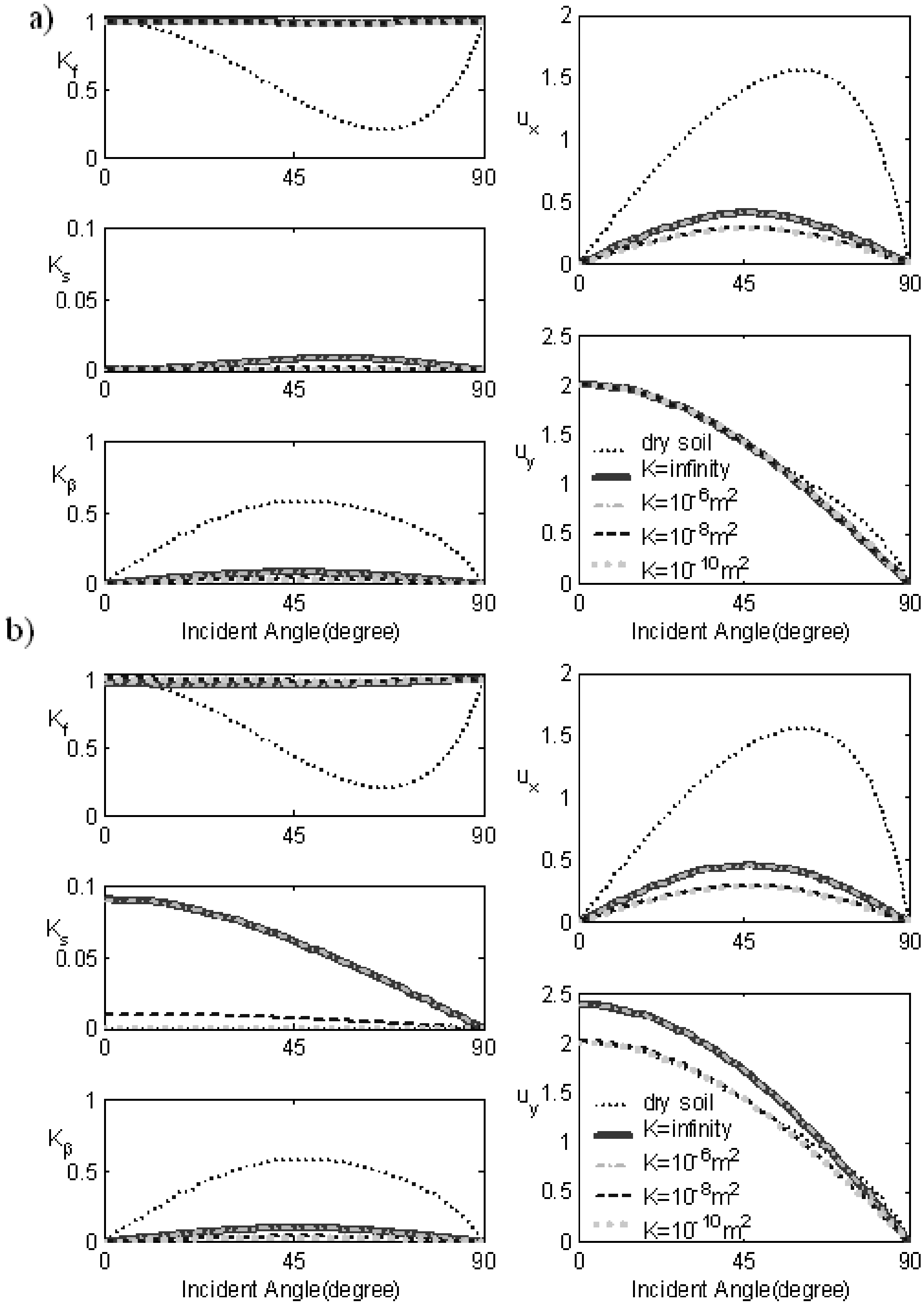

Fig. 3.3.1.1 Free-field motion due to unit displacement plane fast P-wave versus incident angle, for different values of permeability. a) Permeable, b) impermeable half-space. Left: amplitudes of the reflection coefficients. Right: amplitudes of the surface displacements. The input parameters are: porosity $\hat{n} = 0.4$, $\mu / K_f = 0.1$, and the frequency is set to $f = 1$ Hz.

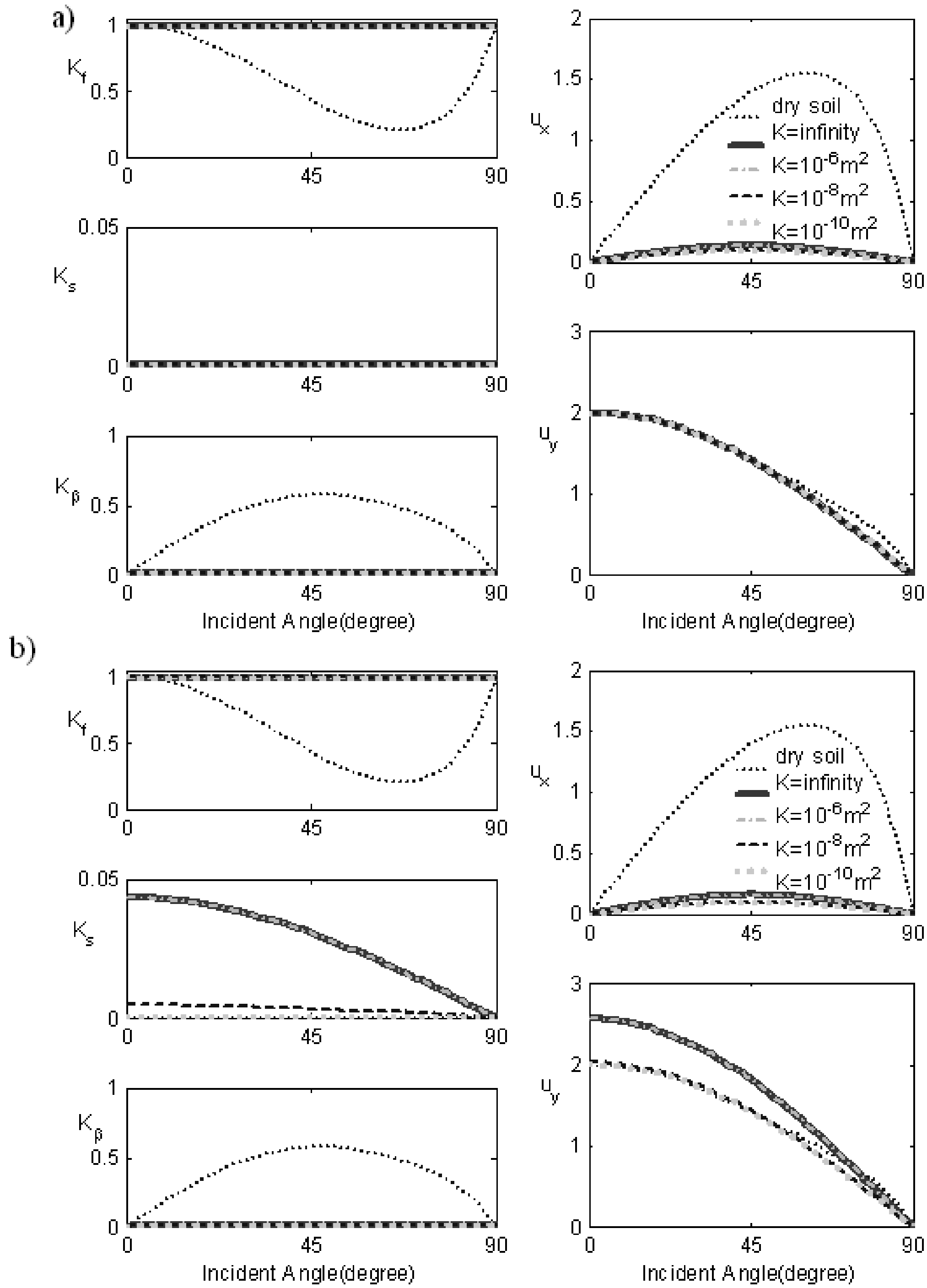

Fig. 3.3.1.2 Same as Fig. 3.3.1.1 but for $\mu / K_f = 0.01$.

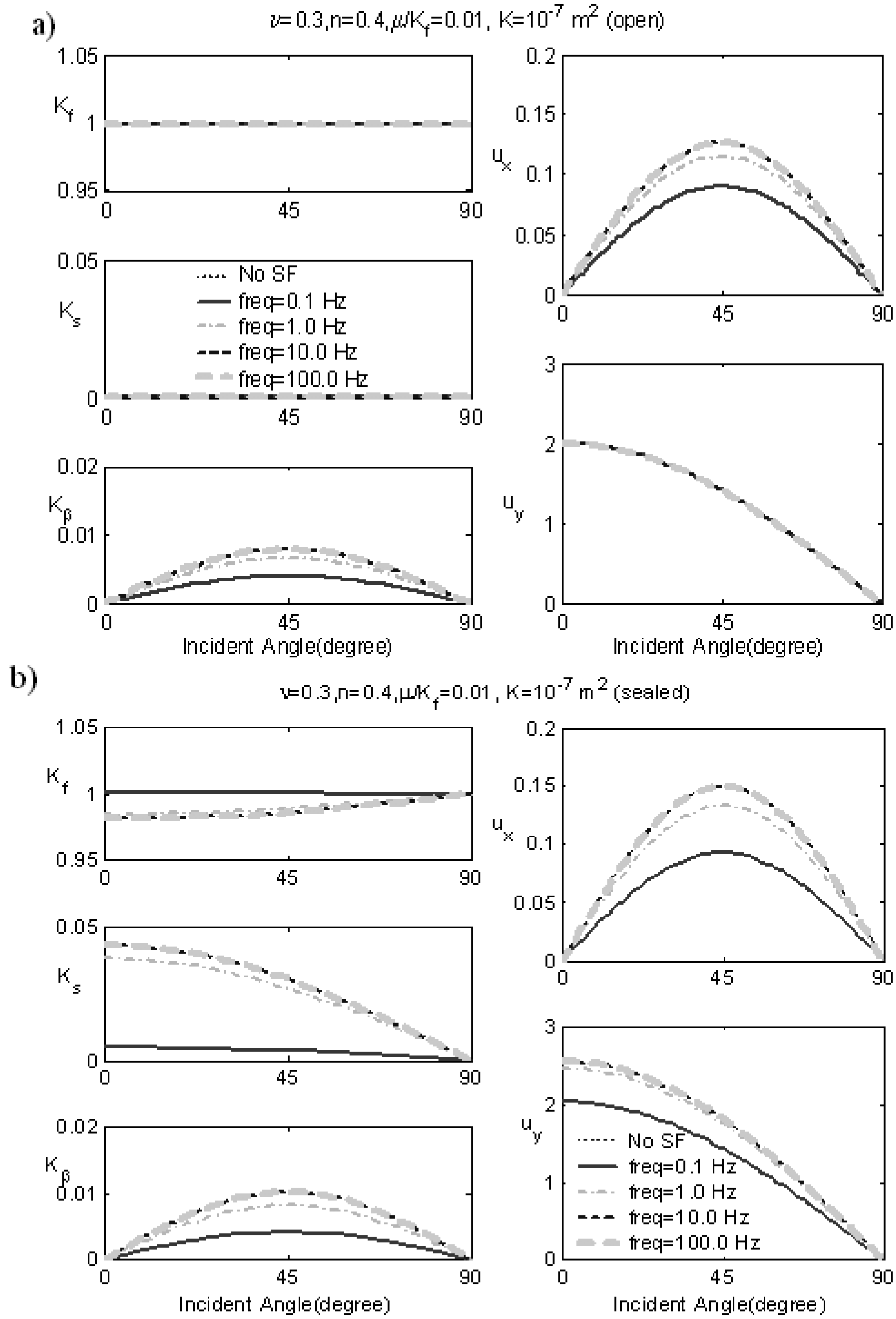

Fig. 3.3.1.3 Free-field motion due to unit displacement plane fast P-wave versus incident angle, for different values of frequency. a) Permeable, b) impermeable half-space. The input parameters are: porosity $\hat{n}=0.4$, $\mu / K_f = 0.01$, and permeability $\hat{k}=10^{-7}\,\mathrm{m}^2$.

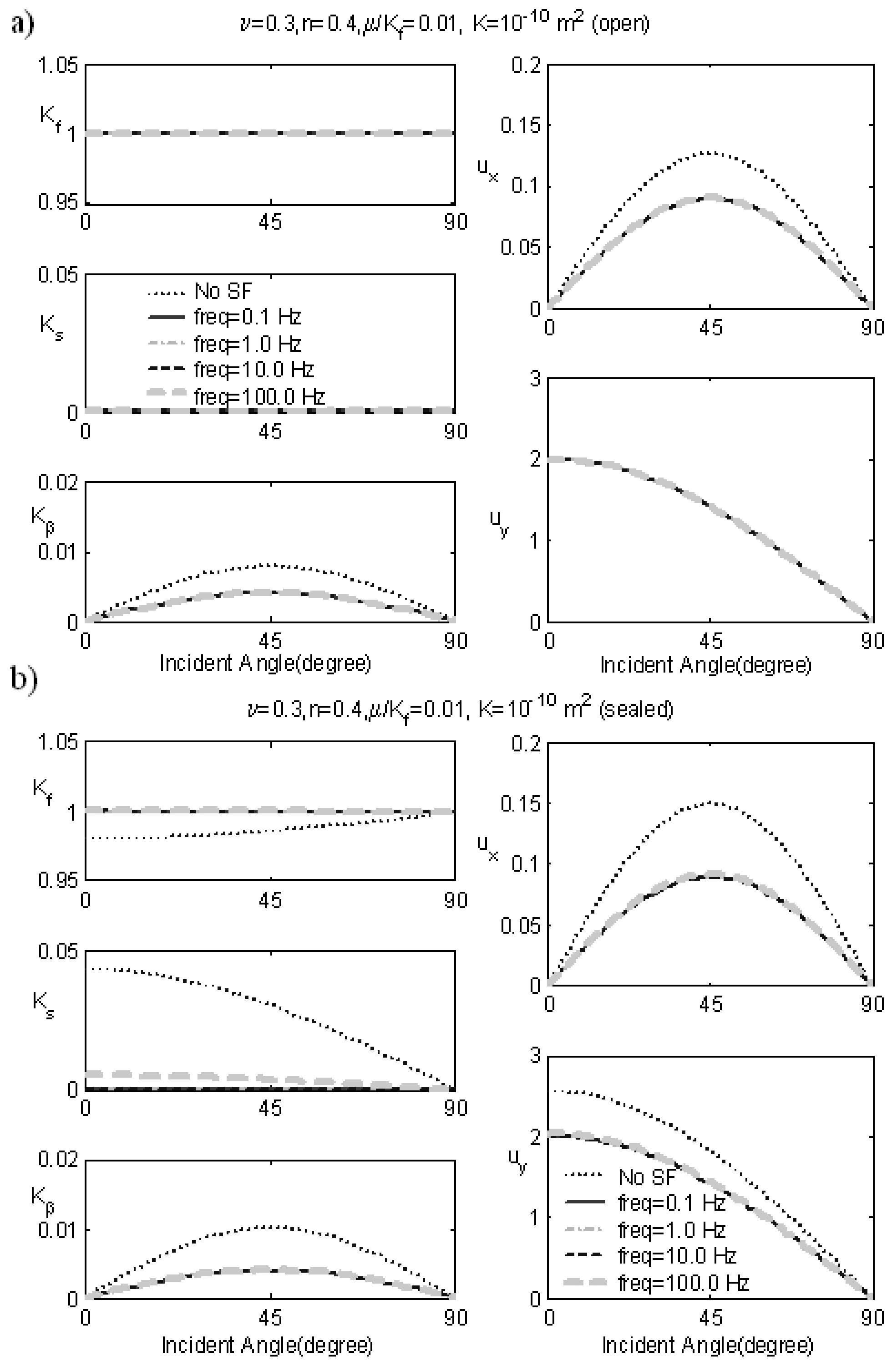

Fig. 3.3.1.4 Same as Fig. 3.3.1.3 but for permeability $\hat{k} = 10^{-10}\,\mathrm{m}^2$.

3.3.1.2 Incident P-wave and Partially Saturated Soil

Similarly as the previous figures, Figs 3.3.1.5 and 3.3.1.6 show variations of the reflection coefficients' amplitudes (left) and surface displacement amplitudes (right) due to an incident plane fast P-wave with unit displacement amplitude, versus the angle of incidence, for different values of saturation $S_r = 100$, 99 and 90%. The effects of the seepage force are neglected, and hence, the results are not dependent on frequency. These two figures differ only in the stiffness of the skeleton. In Fig. 3.3.1.5 $\mu / K_f = 0.1$ (stiff soil) and in Fig. 3.3.1.6 $\mu / K_f = 0.01$ (soft soil). Parts a) and b) differ in the hydraulic boundary condition at the surface. Part a) corresponds to a permeable half-space and part b) to an impermeable half-space. Fig. 3.3.1.5 shows that, for stiff soil, the horizontal displacements are very similar for 90 and 99% saturation, and are significantly larger than for 100% saturation, for both permeable and impermeable half-space. The vertical displacements, for permeable half-space are practically the same for all three levels of saturation, but for impermeable half-space are significantly larger for 100% saturation than for the partial saturation, the difference being the largest for vertical incidence. Fig. 3.3.1.6 shows that, for stiff soil, as far as the effect of the degree of saturation is concerned, the results differ from those for stiff soil only in that the horizontal motions are much more sensitive to the degree of saturation, being almost an order of magnitude larger for 90% saturation than for 100% saturation.

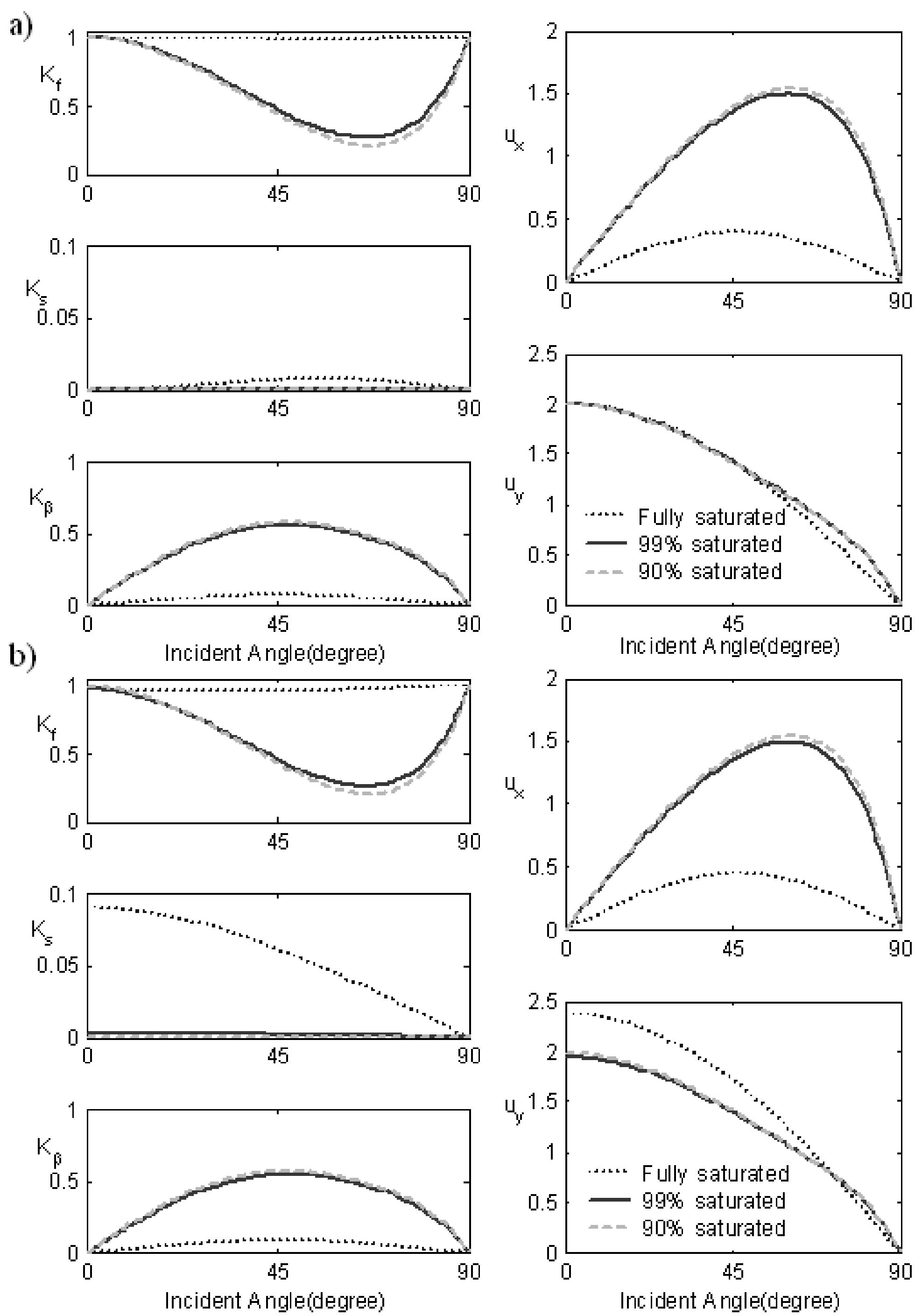

Fig. 3.3.1.5 Free-field motion due to unit displacement plane fast P-wave versus incident angle, for different levels of saturation. a) Permeable, b) impermeable half-space. The input parameters are: porosity $\hat{n} = 0.4$, $\mu / K_f = 0.1$, and frequency $f = 1$ Hz. The effects of the seepage force are neglected.

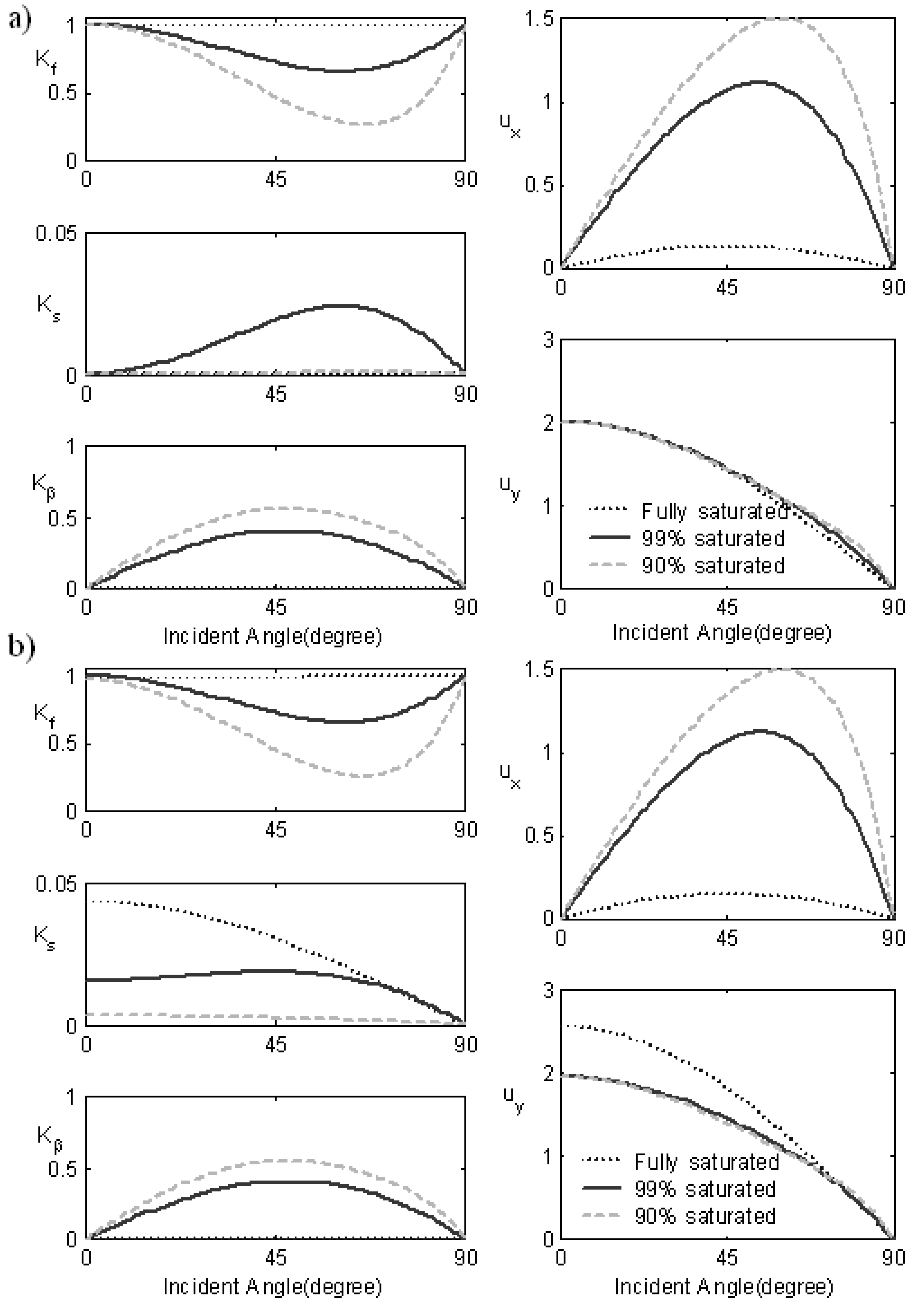

Fig. 3.3.1.6 Same as Fig. 3.3.1.5 but for $\mu / K_f = 0.01$.

3.3.2 Incident Plane SV-wave

3.3.2.1 Incident SV-wave and Fully Saturated Soil

Figures 3.3.2.1 through 3.3.2.4 show results for the free-field motion due to an incident plane SV-wave onto a half-space for the same parameters as Figs 3.3.1.1 through 3.3.1.4. It can be seen that for vertical incidence, the horizontal displacement on the surface always approaches 2, and the vertical displacement approaches zero. As the incident angle approaches 90°, both the vertical and horizontal displacements approach zero. For 45° incidence, and for permeable half-space, the horizontal displacements are always zero, while for impermeable half-space, they are not necessarily zero but are small. It can be seen that the surface displacements for incident SV wave are not very sensitive to the hydraulic boundary condition. A comparison with the results for incident P-wave shows that, for incident SV-wave, both the horizontal and vertical surface displacements are more sensitive to the variations of permeability and frequency, i.e. are affected more by the seepage force, than for incident P-wave. For frequency set to $f = 1$ Hz, the maximum displacement amplitudes (over all incident angles) are significantly larger for larger seepage force than for "no seepage force" (see Figs 3.3.2.1 and 3.3.2.2), but as the frequency increases, they decrease and approach the values for "no seepage force". A comparison of the fully saturated and dry soil cases shows that the maximum horizontal displacements (over all incident angles) are larger for the dry soil, while the vertical displacements are larger for the saturated soil, and for smaller permeability.

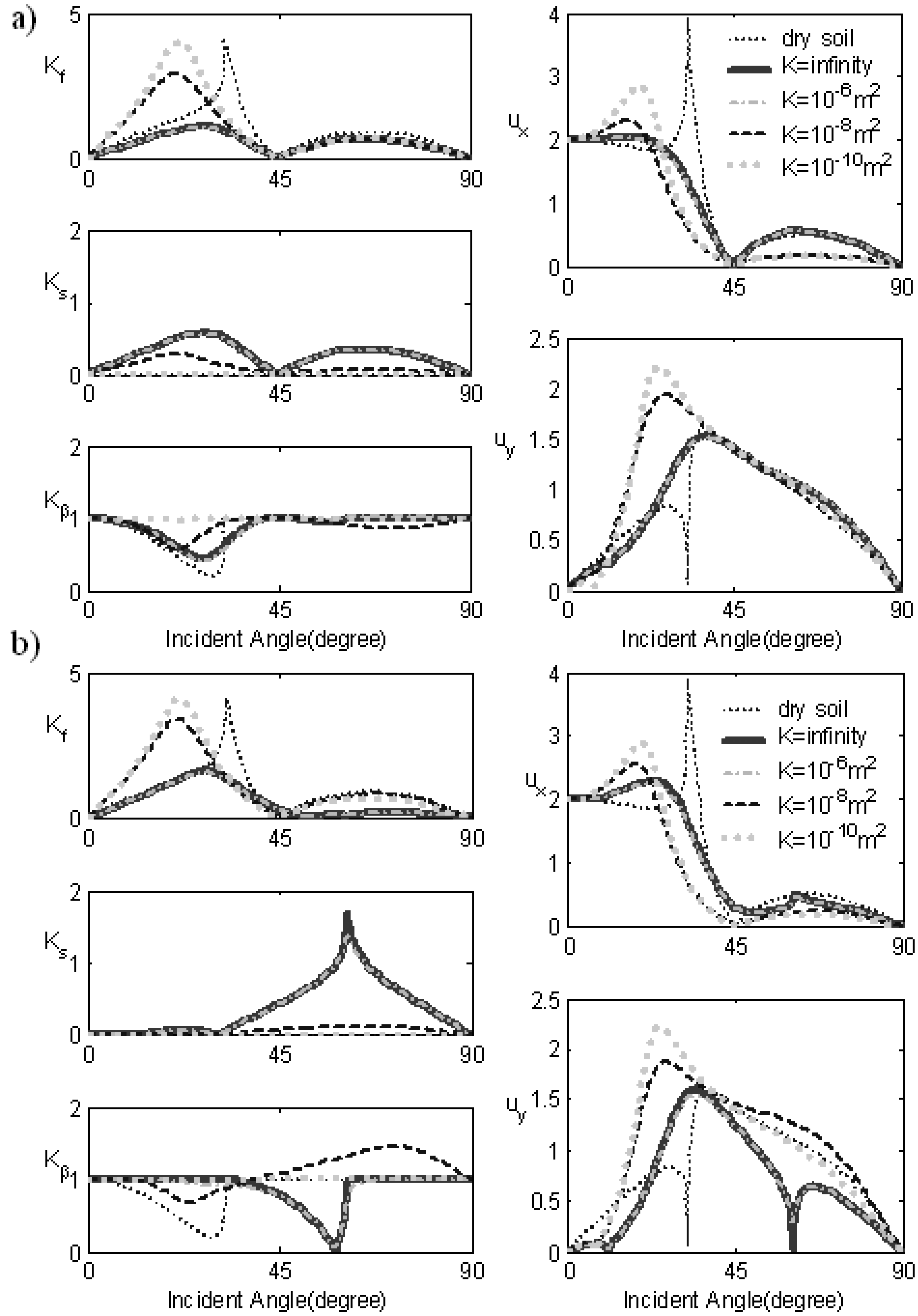

Fig. 3.3.2.1Free-field motion due to unit displacement plane SV-wave versus incident angle, for different values of permeability. a) Permeable, b) impermeable half-space. Left: amplitudes of the reflection coefficients. Right: amplitudes of the surface displacements. The input parameters are: porosity $\hat{n} = 0.4$, $\mu / K_f = 0.1$, and the frequency is set to $f = 1$ Hz.

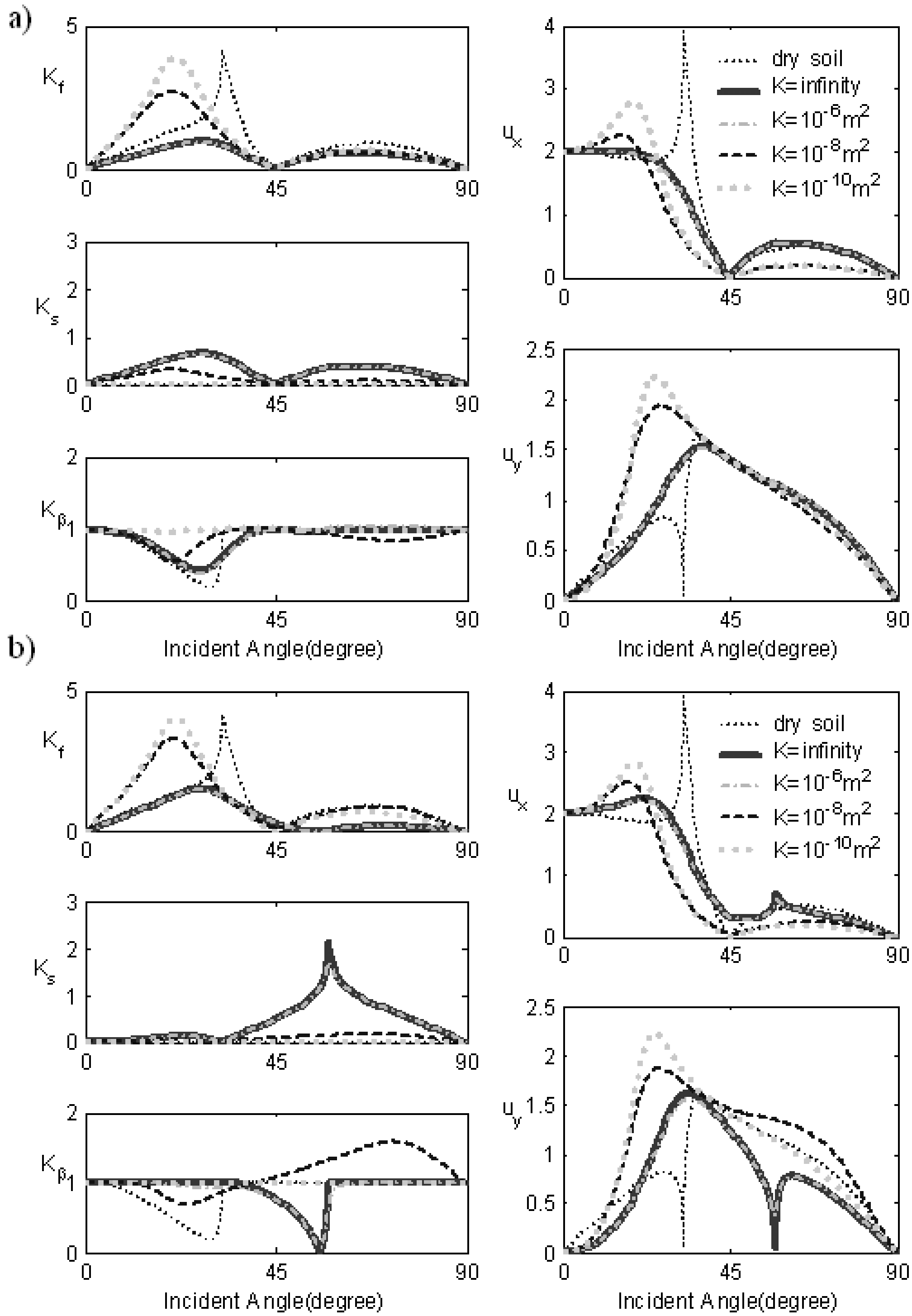

Fig. 3.3.2.2 Same as Fig. 3.3.2.1 but for $\mu / K_f = 0.01$.

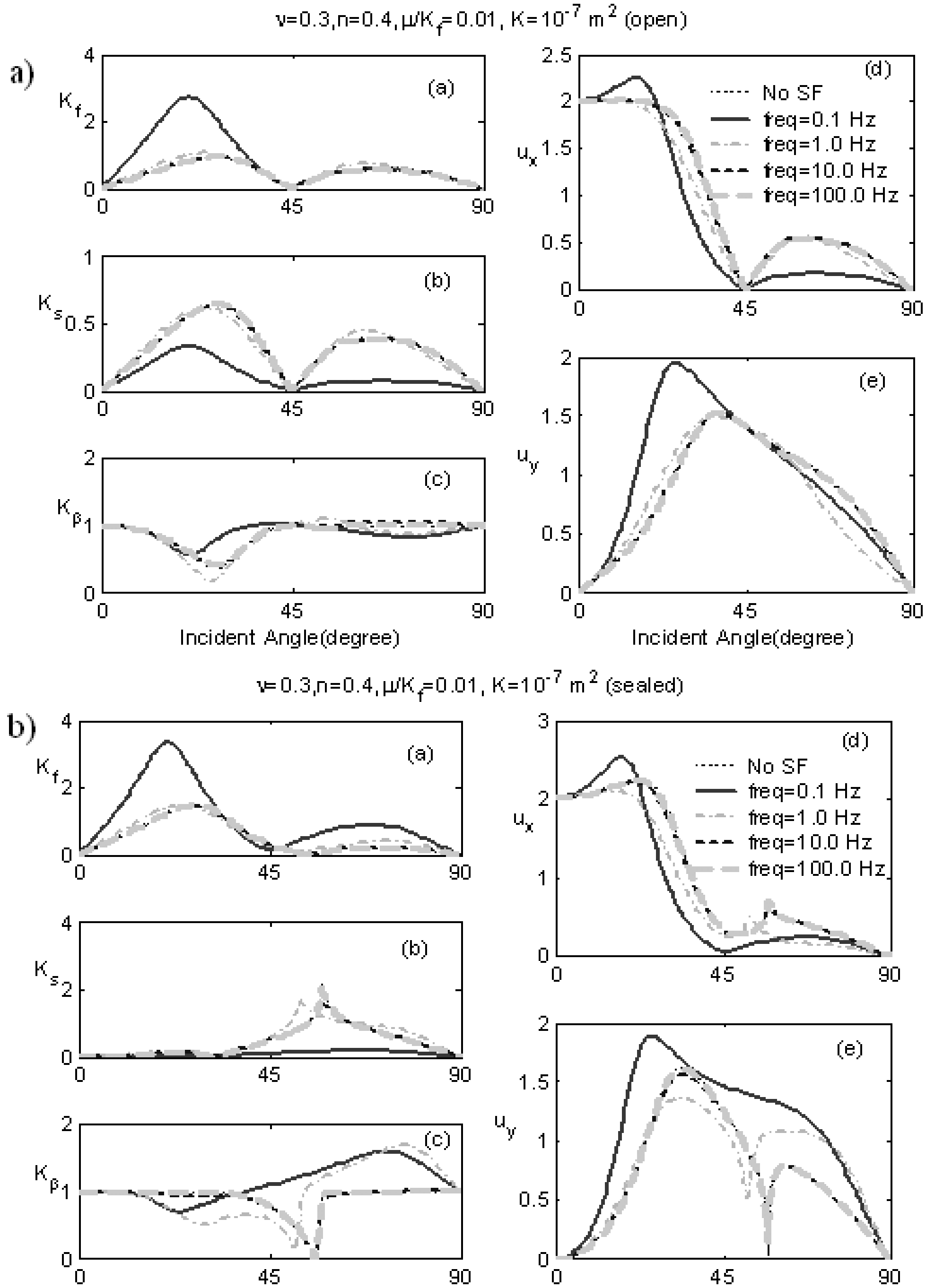

Fig. 3.3.2.3 Free-field motion due to unit displacement plane SV-wave versus incident angle, for different values of frequency. a) Permeable, b) impermeable half-space. The input parameters are: porosity $\hat{n} = 0.4$, $\mu / K_f = 0.01$, and permeability $\hat{k} = 10^{-7}\,\mathrm{m}^2$.

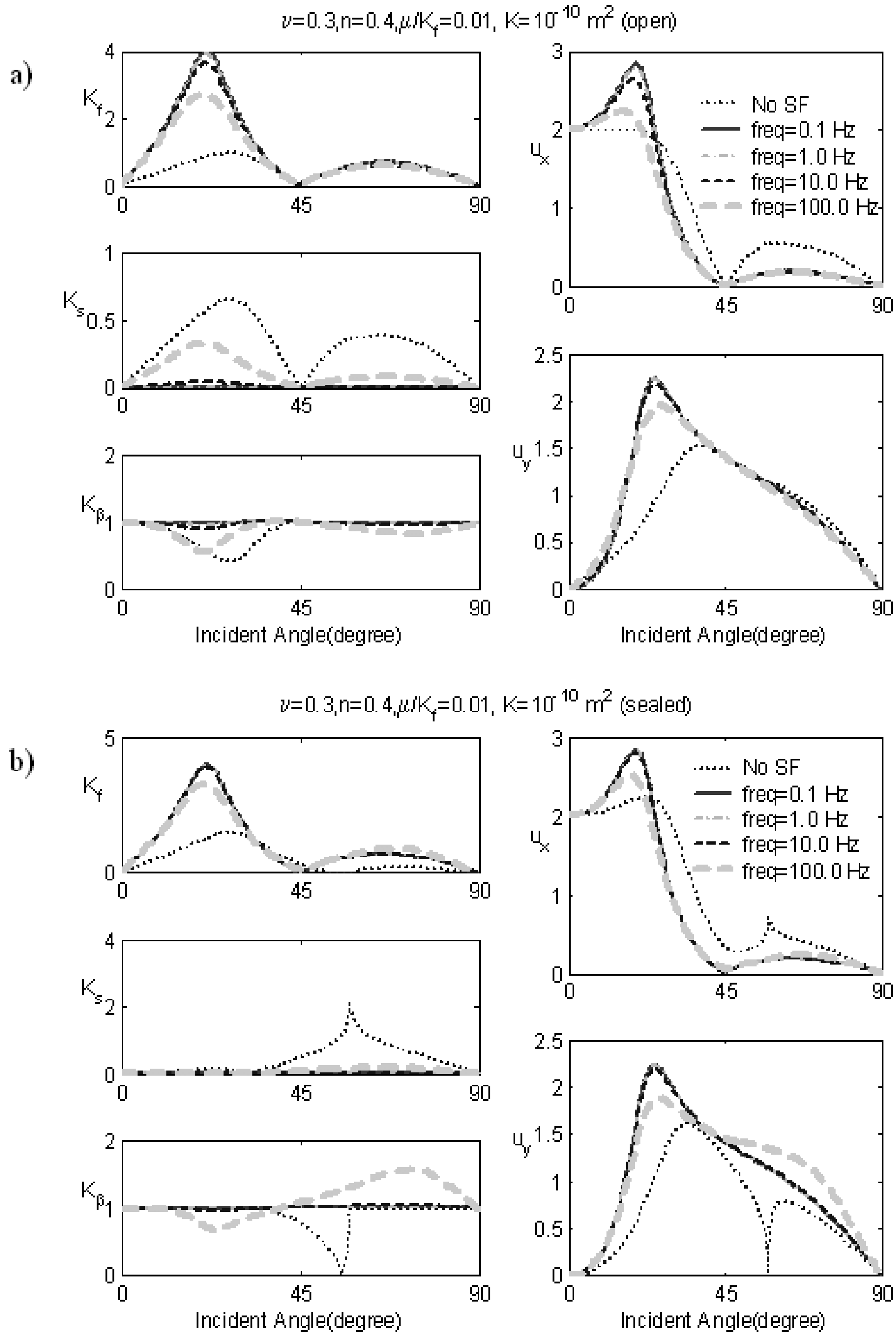

Fig. 3.3.2.4 Same as Fig. 3.3.2.3 but for permeability $\hat{k} = 10^{-10}\mathrm{m}^2$.

3.3.2.2 Incident SV-wave and Partially Saturated Soil

Figs 3.3.2.5 and 3.3.2.6 show results for the free-field motion due to an incident SV-wave for partial saturation, also for the same soil properties as in Figs 3.3.1.5 and 3.3.1.6. It can be seen from these results that the vertical displacements are not very sensitive to the degree of saturation, but the maximum (over all incident angles) horizontal amplitudes are much larger for the partially saturated soils than for the fully saturated soil.

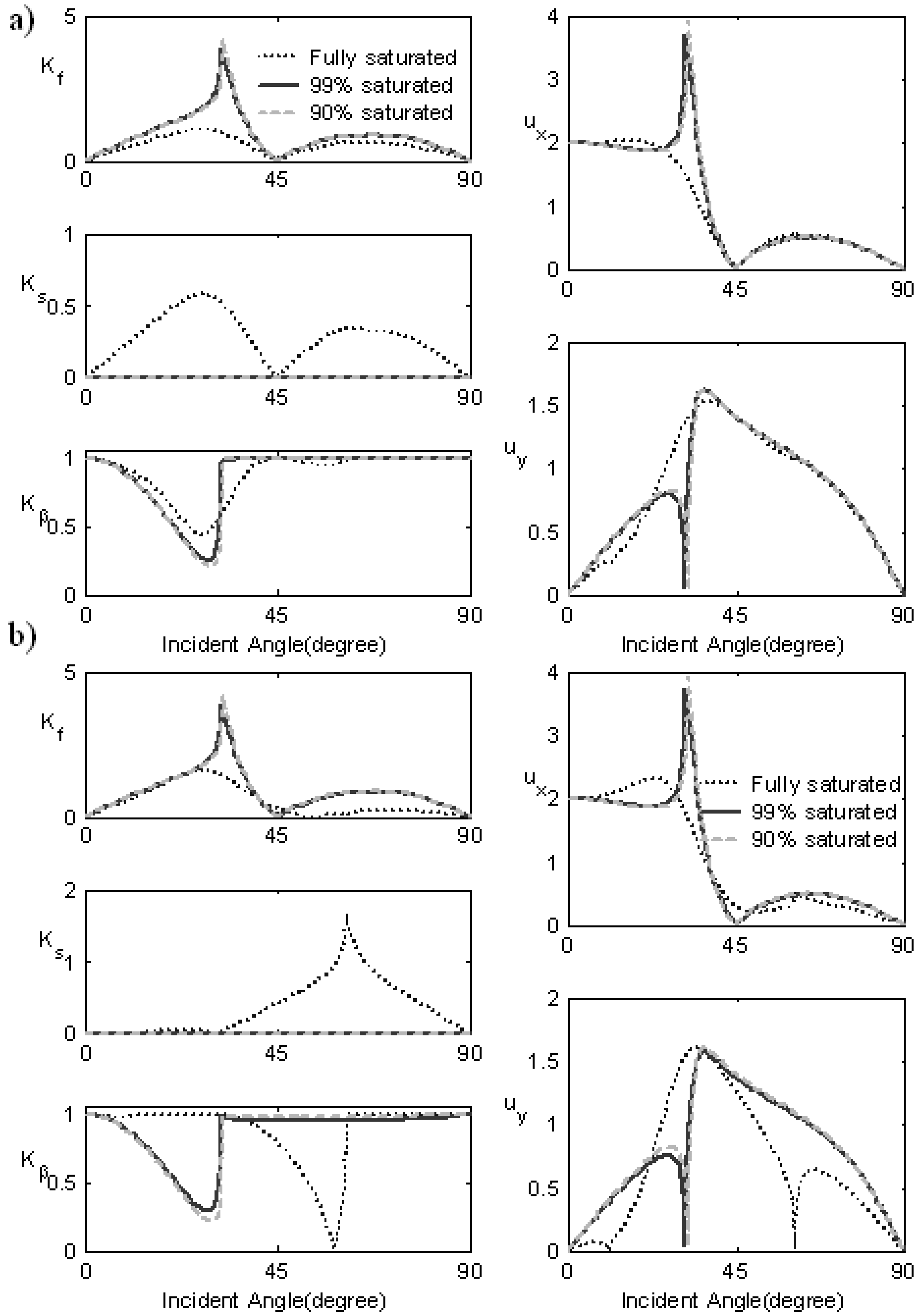

Fig. 3.3.2.5 Free-field motion due to unit displacement plane SV-wave versus incident angle, for different levels of saturation. a) Permeable, b) impermeable half-space. The input parameters are: porosity $\hat{n}=0.4$, $\mu/K_f=0.1$, permeability $\hat{k}=10^{-7}\mathrm{m}^2$, and frequency $f=1$ Hz.

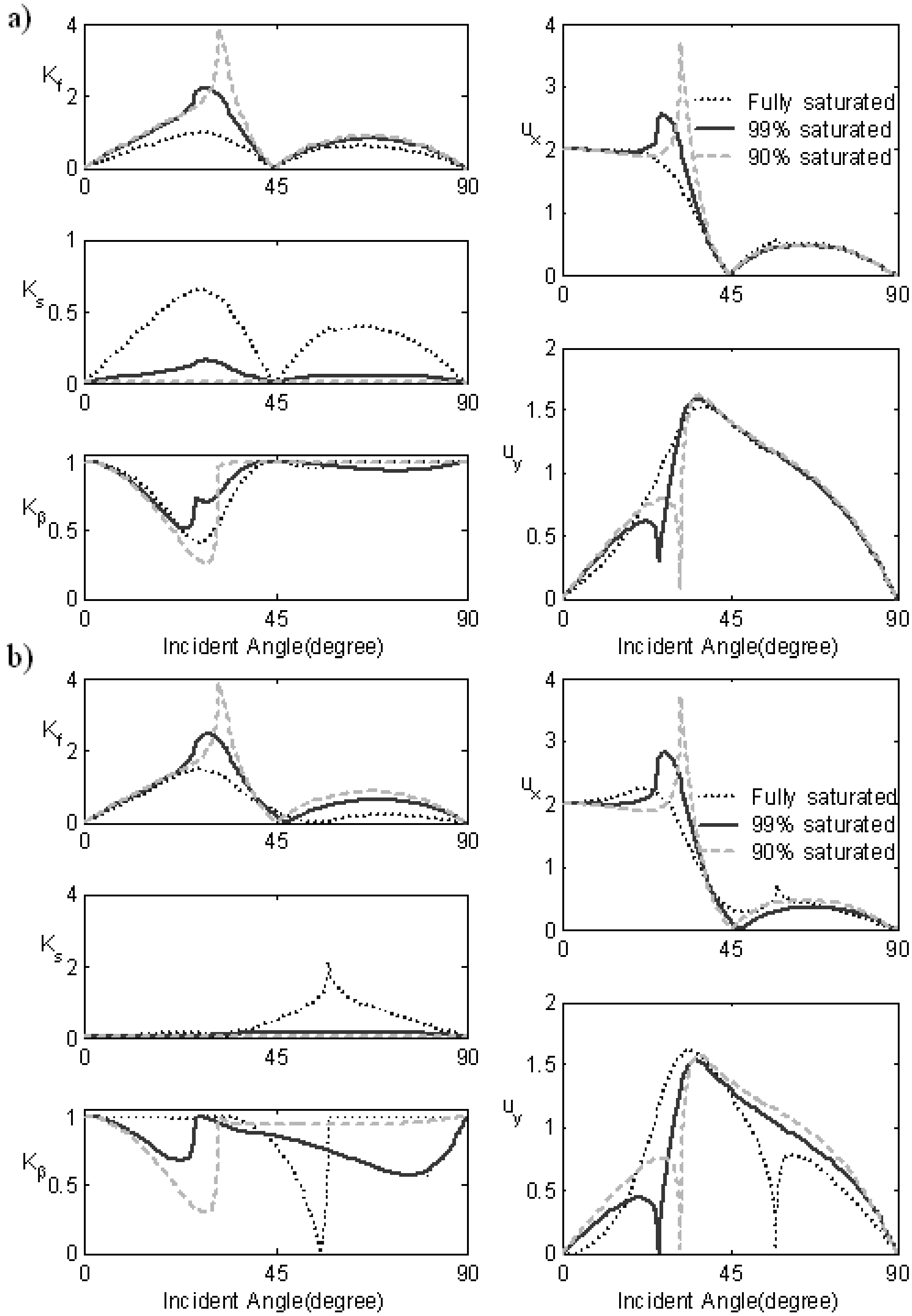

Fig. 3.3.2.6 Same as Fig. 3.3.2.5 but for $\mu / K_f = 0.01$.

3.4 Foundation Input Motion

Foundation input motion is, by definition, the response of a massless foundation to the incident waves. The interaction of the incident waves with the massless foundation is also referred to as kinematic interaction. Hence, the foundation input motion is essentially the free-field motion plus some perturbation due to scattering of the waves from the foundation. This perturbation is very small for very long incident waves compared to the size of the foundation. While the free-field motion was studied in detail in Section 3.3, this section focuses on the effect of the saturation as function of dimensionless frequency η, showing results only for one incident angle and for stiff soil.

Figure 3.4.1 and 3.4.2 show the amplitudes of the vertical displacements $|V|$, horizontal displacements $|\Delta|$ and rocking amplitudes $|\varphi a|$, versus dimensionless frequency $\eta = \dfrac{\omega a}{\pi V_{\mathrm{S,dry}}}$, respectively for an incident fast P- and an incident SV-wave, both at 30° incidence. The results are for stiff soil, with $\mu / K_f = 0.1$, porosity $\hat{n} = 0.4$, and full saturation. Results for dry soil are also shown. In part a), the half-space is permeable, and in part b) it is impermeable. In both parts a) and b), the pots on the left correspond to permeable soil-foundation interface, and the plots on the right to impermeable interface. It can be seen that the nature of the variation of the amplitudes of the three components of the foundation input motion with frequency is similar for saturated soil as for dry soil, which has been studies previously in detail.

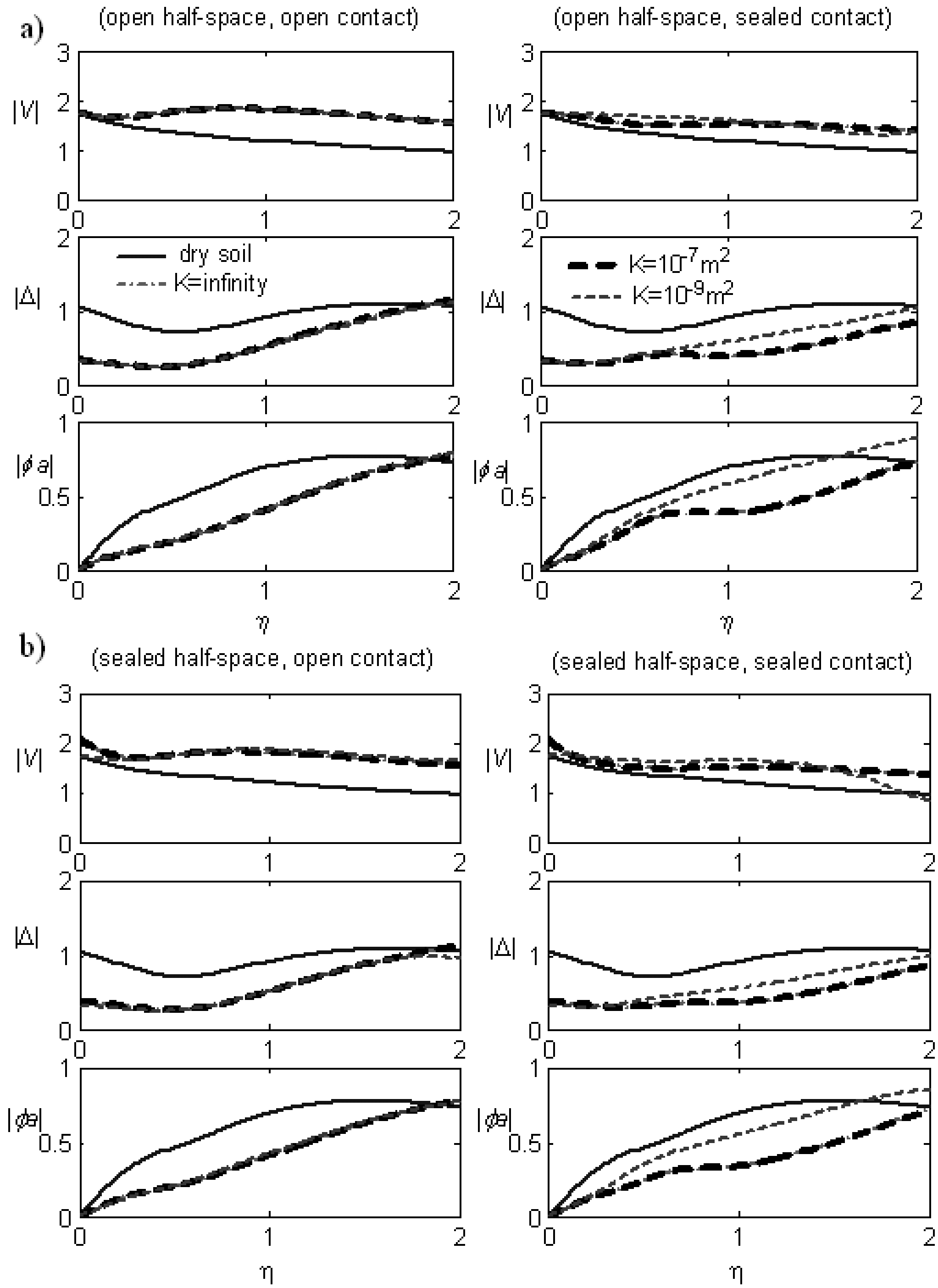

Fig. 3.4.1 Foundation input motion amplitudes due to an incident plane fast P-wave at 30° incidence, for $\mu / K_f = 0.1$, porosity $\hat{n} = 0.4$. Part a): permeable half-space. Part b) impermeable half-space. Left: permeable foundation. Right: impermeable foundation.

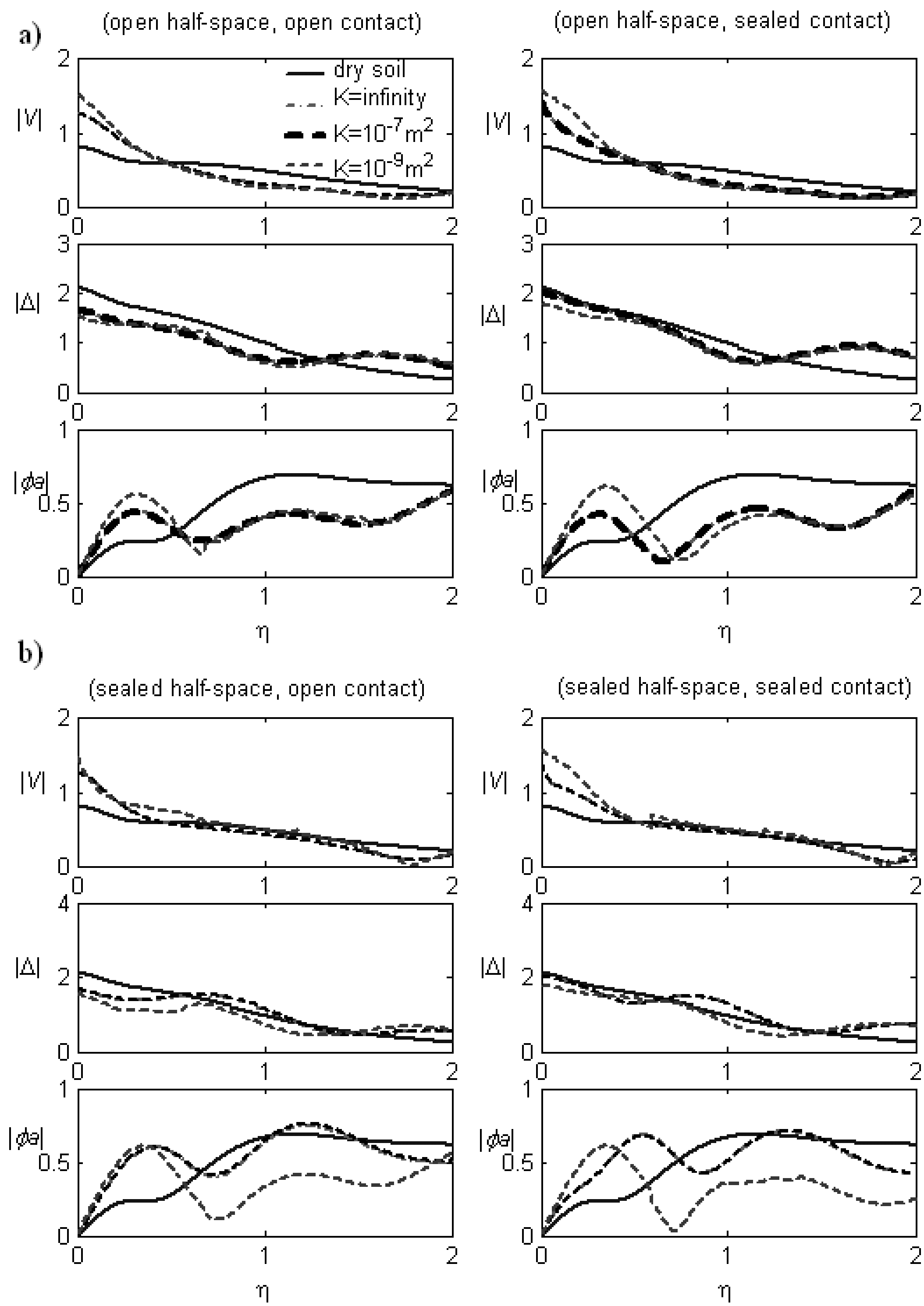

Fig. 3.4.2 Same as Fig. 3.4.1 but for an incident plane SV-wave at 30° incidence.

3.5 Building-Foundation-Soil Response

This section shows results for the amplitudes of the foundation displacements and building relative displacement (due to elastic deformation of the building only), for stiff soil with $\mu / K_f = 0.1$ and porosity $\hat{n} = 0.4$, and for a building with height $H = 2a$, width $W = a$, and mass ratios $m_b / m_f = 2$ and $m_f / m_s = 0.2$. The excitation is an incident plane fast P-wave or a plane SV-wave, both at 30° incidence, and with unit displacement of the incident wave.

3.5.1 Building-Foundation-Soil Response for Incident P-wave

Figures 3.5.1.1 through 3.5.1.4 show results for incident P-wave at 30° incidence. In all figures, $|V|$ is the amplitudes of the vertical displacements, $|\Delta|$ is the amplitudes of the horizontal displacements, $|\varphi a|$ is the rocking angle multiplied by the characteristic length a, $|u_{\mathrm{b}}^{\mathrm{rel}}|$ is the relative building response at the top, and the dimensionless frequency is $\eta = \dfrac{\omega a}{\pi V_{\mathrm{S,dry}}}$. In each figure, part a) corresponds to permeable half-space, and part b) to impermeable half-space.

Figures 3.5.1.1 and 3.5.1.2 show the variation of the system response with η for fully saturated soil with different permeability, respectively for permeable and for impermeable foundation. The response for dry soil is also shown. Figures 3.5.1.3 and 3.5.1.4 show the variation of the system response with η for different levels of saturation. These figures show that both the foundation and the building relative response exhibit large variations near the building fixed-base frequencies. The "backbone" curve of the foundation displacement amplitudes is governed by the foundation input motion, shown in Section 3.4, which also affects the amplitudes of the peaks of the building relative response. The building relative response has peaks at the system frequencies. Due to the interaction with the foil, the first system frequency is lower than the fundamental fixed-base frequency, and the amplitude of the peak is generally reduced due to the radiation of energy in the soil. It is well known that the amount of the shift and the reduction of amplitude depend on the relative flexibility of the soil, which in case of porous soil depends on the water content, soil permeability, and also frequency. The effect of the flexibility of the soil is described through the foundation complex stiffness matrix (See Section 3.2). In the "coarse" resolution plots in these figures, no significant shift of the peaks can be seen as function of the water content and permeability. Hence, if there is a change, it is small. Investigation of such changes for one case study building is presented in the following section.

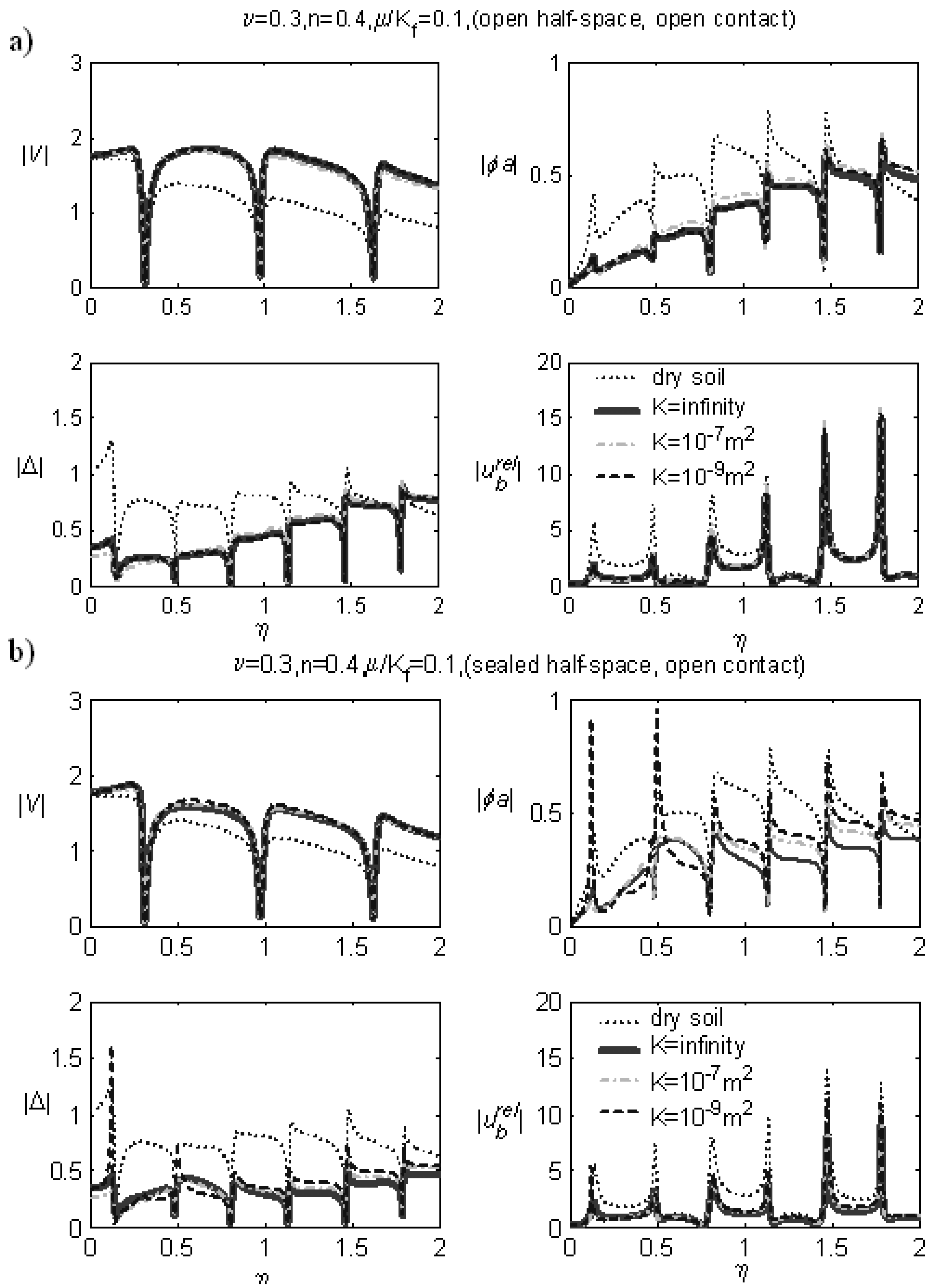

Fig. 3.5.1.1 System response due to an incident plane fast P-wave at 30° incidence, for $\mu / K_f = 0.1$, porosity $\hat{n} = 0.4$, $H = 2a$, width $W = a$, and mass ratios $m_b / m_f = 2$, $m_f / m_s = 0.2$, and for a permeable foundation. Part a): permeable half-space. Part b) impermeable half-space. The different curves correspond to different soil permeability.

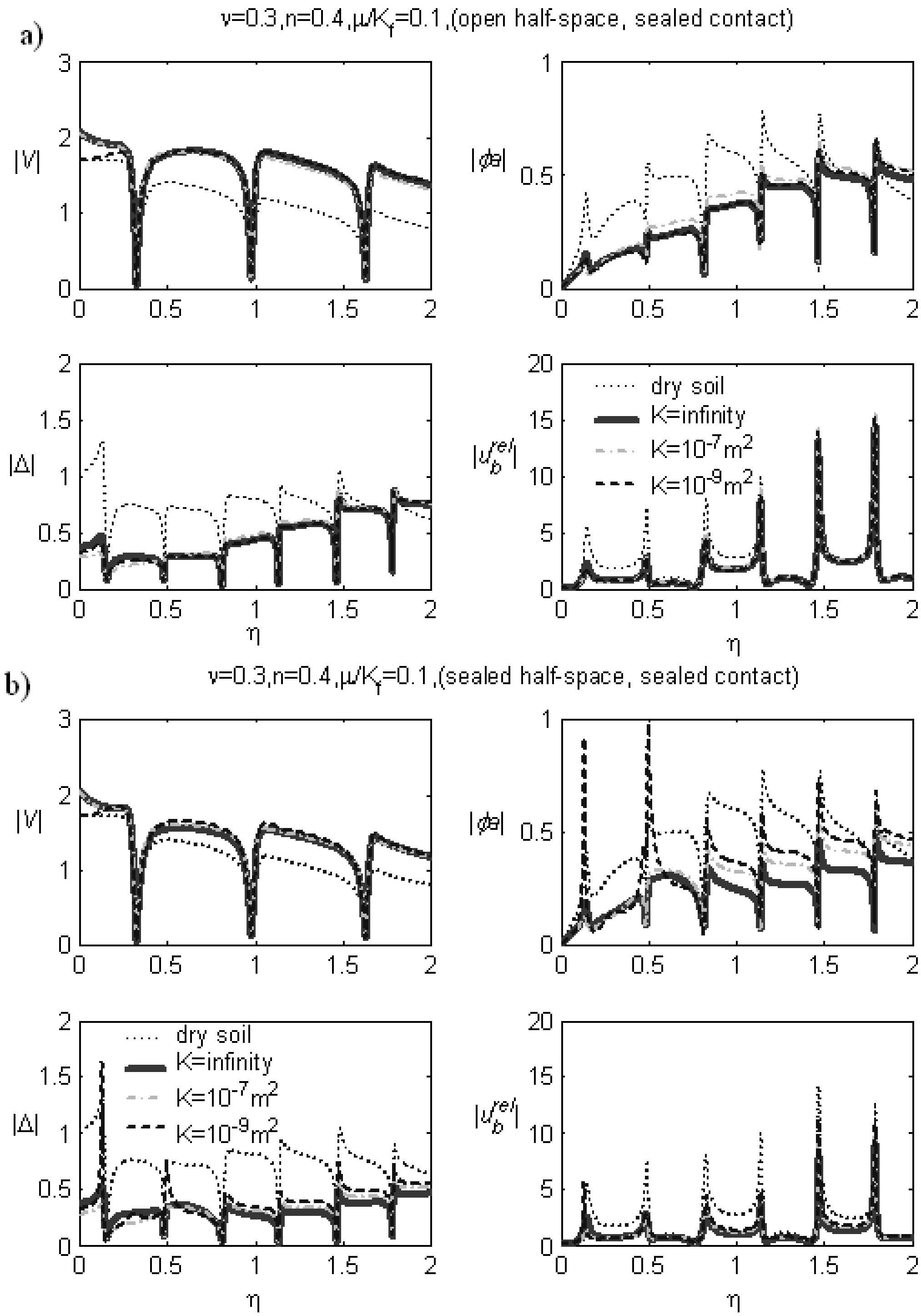

Fig. 3.5.1.2 Same as Fig. 3.5.1.1, but for impermeable foundation.

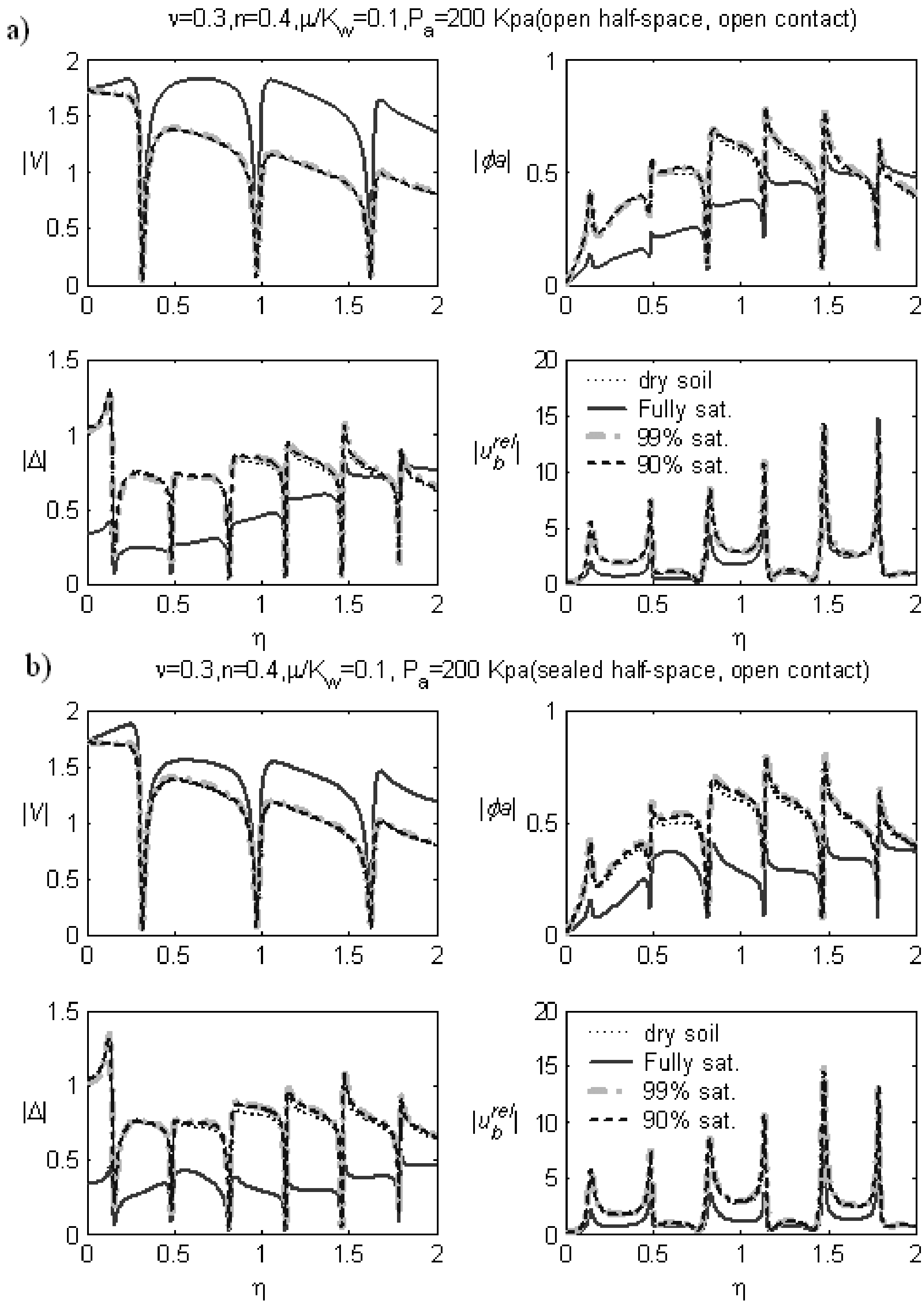

Fig. 3.5.1.3 Same as Fig. 3.5.1.1, but the different curves correspond to different levels of saturation.

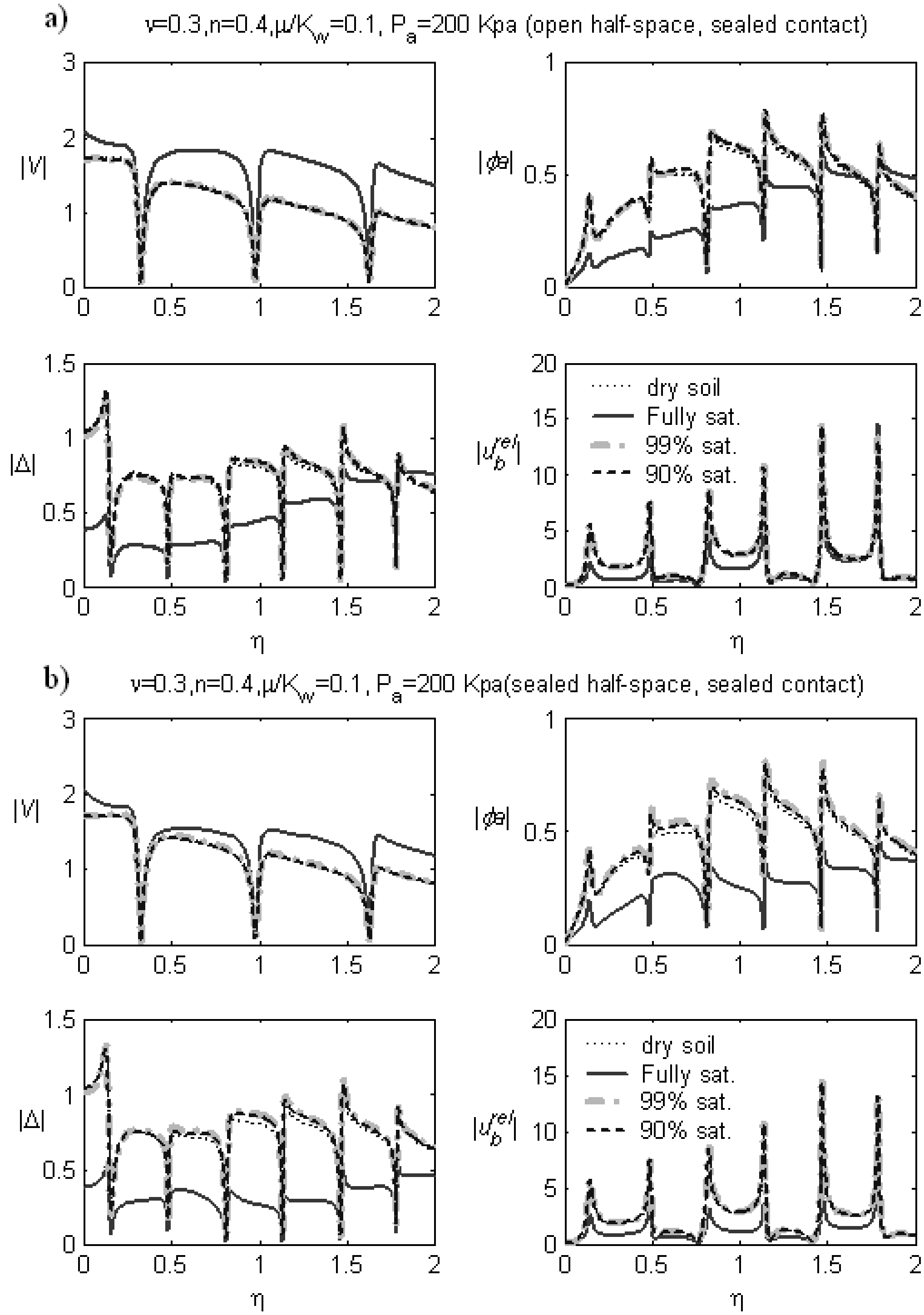

Fig. 3.5.1.4 Same as Fig. 3.5.1.1, but the different curves correspond to different levels of saturation, and the foundation is impermeable.

3.5.2 Building-Foundation-Soil Response for Incident SV-wave

Similarly as in Section 3.5.1, Figures 3.5.2.1 through 3.5.2.4 show results for incident SV-wave at 30° incidence. In all figures, $|V|$ is the amplitudes of the vertical displacements, $|\Delta|$ is the amplitudes of the horizontal displacements, $|\varphi a|$ is the rocking angle multiplied by the characteristic length a, $\left|u_{\mathrm{b}}^{\mathrm{rel}}\right|$ is the relative building response at the top, and the dimensionless frequency is $\eta = \dfrac{\omega a}{\pi V_{\mathrm{S,dry}}}$. In each figure, part a) corresponds to permeable half-space, and part b) to impermeable half-space. The observations in these figures are the same as in Section 3.5.1 for incident P-wave.

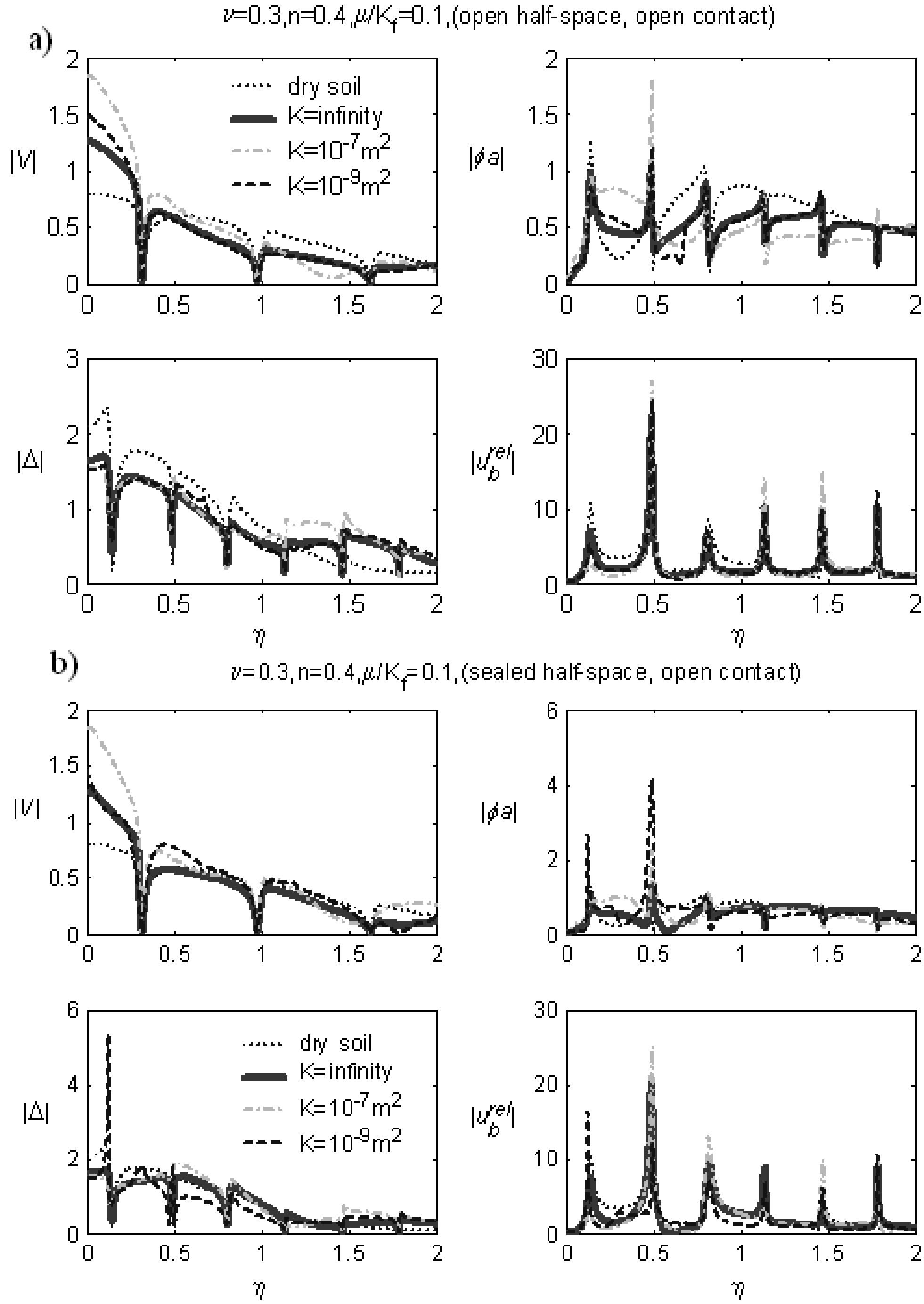

Fig. 3.5.2.1 System response due to an incident plane SV-wave at 30° incidence, for $\mu / K_f = 0.1$, porosity $\hat{n} = 0.4$, $H = 2a$, width $W = a$, and mass ratios $m_b / m_f = 2$, $m_f / m_s = 0.2$, and for a permeable foundation. Part a): permeable half-space. Part b) impermeable half-space. The different curves correspond to different soil permeability.

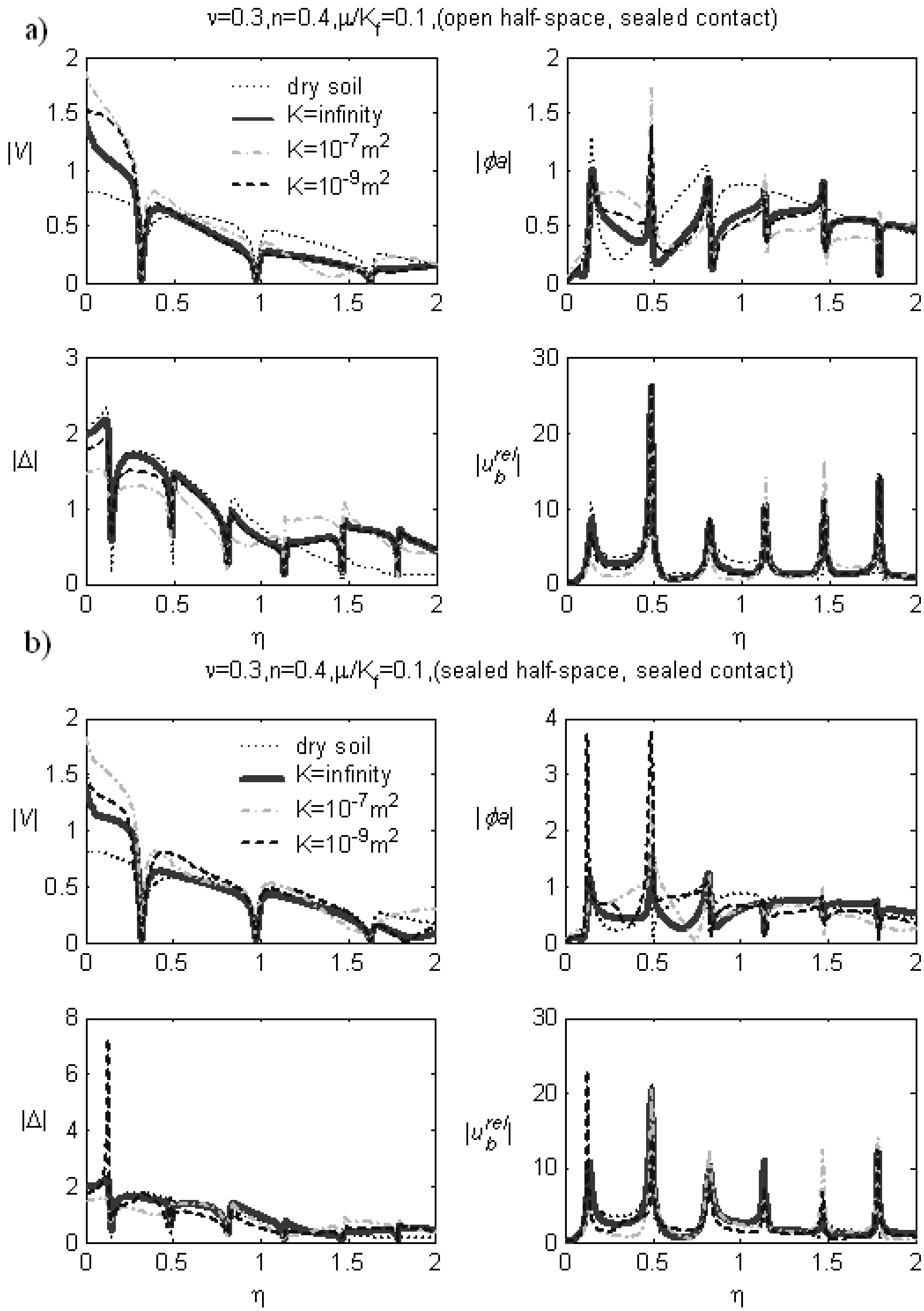

Fig. 3.5.2.2 Same as Fig. 3.5.2.1, but for impermeable foundation.

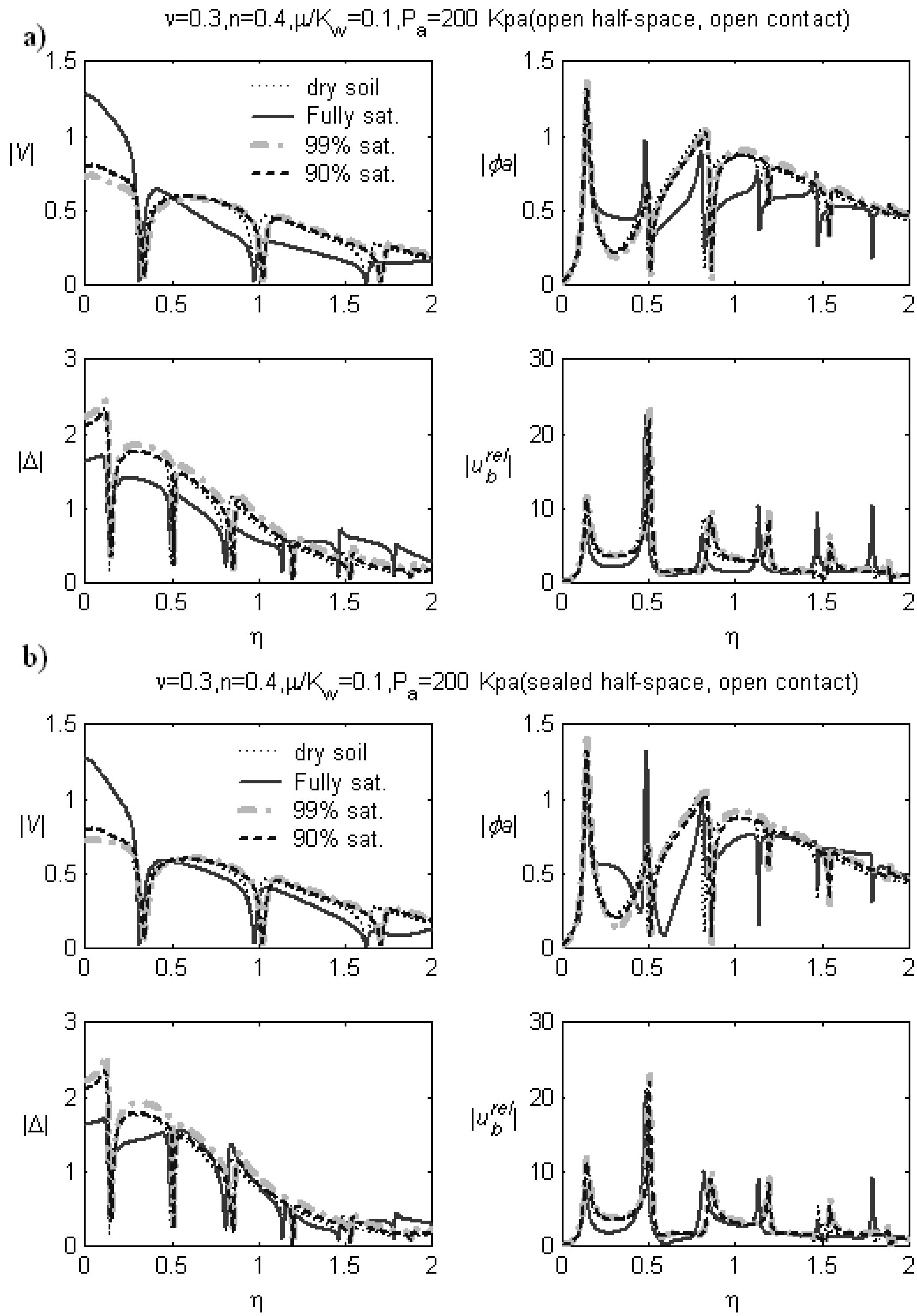

Fig. 3.5.2.3 Same as Fig. 3.5.2.1, but the different curves correspond to different levels of saturation.

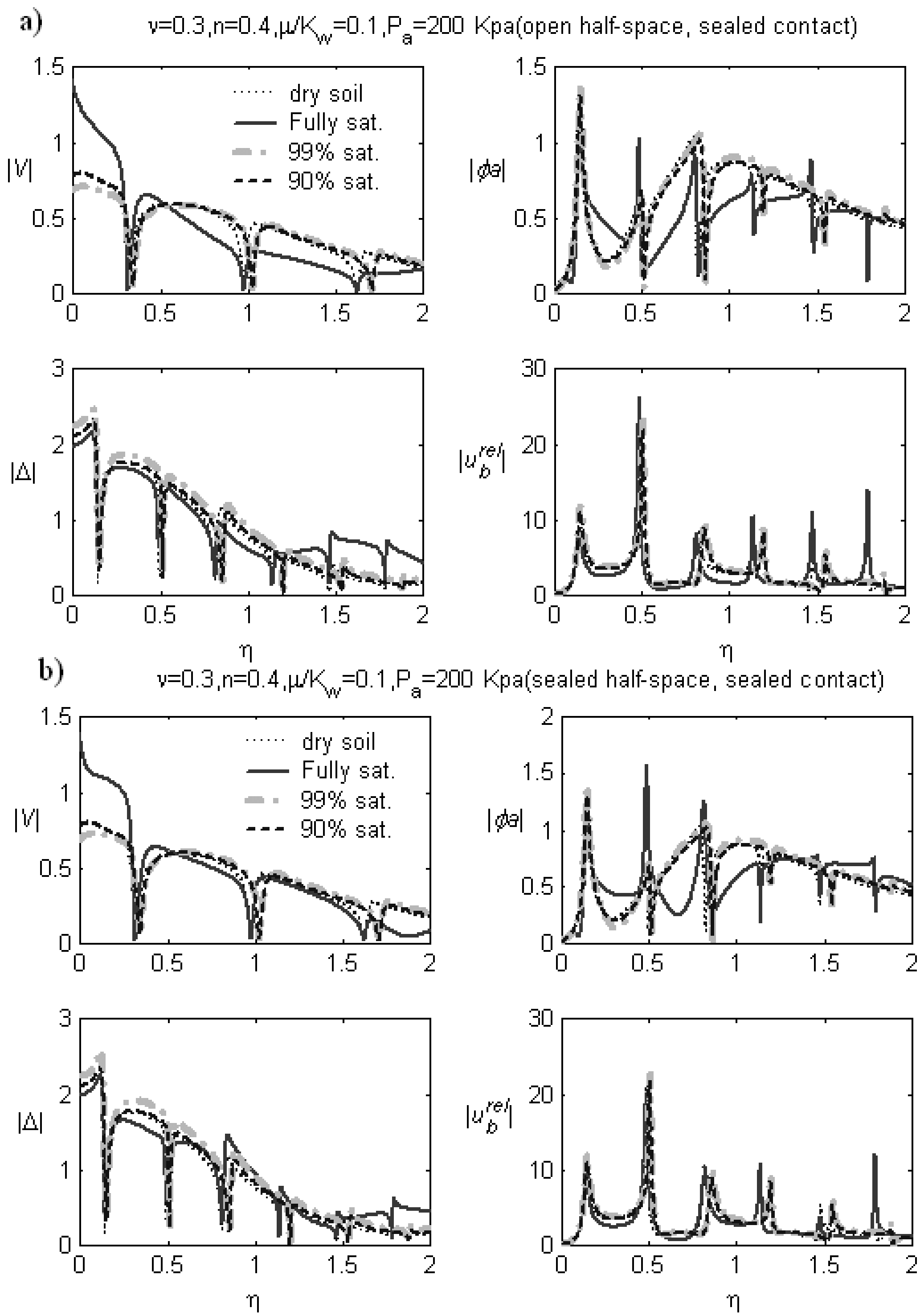

Fig. 3.5.2.4 Same as Fig. 3.5.2.1, but the different curves correspond to different levels of saturation, and the foundation is impermeable.

3.6 Frequency Shift due to Saturation – Millikan Library Case

This section shows results for the model response for parameters chosen so that it corresponds approximately to the NS response of Millikan Library in Pasadena, California. This building has been chosen because changes of its frequencies of vibration have been reported such that can be correlated with heavy rainfall (Clinton et al., 2006). Todorovska and Al Rjoub (2006b) attempted to explain these changes as resulting from changes in the soil due to saturation. They used a soil-structure interaction model in poroelastic soils, presented in Todorovska and Al Rjoub (2006a), and showed that changes in the soil due to saturation produced the same trend and order of magnitude of the shift as observed. The model of Todorovska and Al Rjoub (2006a) is an earlier version of the model analyzed in this thesis that did not include the effects of the seepage force. Hence, this section focuses on how different assumptions on the soil permeability would affect the frequency shift. For the purpose of completeness of the analysis in this thesis work, a summary of the full-scale observations, as well as of the choice of model parameters in Todorovska and Al Rjoub (2006b) is included.

3.6.1 Full-scale Observations

The frequencies of vibration of Millikan Library have been monitored since 1967 using different excitations such as ambient noise, forced vibrations, and earthquakes. Permanent and temporary changes in its frequencies have been observed, most recently summarized in Clinton et al. (2006). The permanent change is decrease with time, from 1.45 to 1.19 Hz for EW vibrations, and from 1.9 to 1.72 Hz for NS vibrations, as measured during small amplitude vibrations. The lowest measured values occurred during the strong earthquake shaking from the 1971 San Fernando earthquake (Udwadia and Trifunac, 1974), and 1994 Northridge earthquake (0.94 Hz for EW vibrations, and 1.33 Hz for NS vibrations; Cinton et al., 2006). Since February of 2001, continuous data steams of the 9th floor response have been recorded by a tri-axial 24-bit accelerometer, which is one of the stations of the California Integrated Seismic Network. This has enabled monitoring of changes of the building apparent frequencies on different time scales (Clinton et al., 2006). Further, weather data from the nearby JPL Weather station, located about 8.5 km north of the building, has been available for a period of about 2.5 years following the installation of this sensor, which enabled to study possible correlations of the changes of its frequencies with weather (temperature, wind and rain).

The reported observation of the changes of the building frequencies with rainfall is as follows. The building first and second apparent frequencies for EW and NS motions, and the first frequency for torsional motions *increase* during heavy rainfall (above 40 mm per day) in a matter of hours, and recover in about a week following the rain (Clinton, 2004; Clinton et al., 2006). For example, in early February of 2003, when over 100 mm rain fell over a period of two days, an increase of about 3% was measured for the EW and the torsional frequencies, followed by a slow decay over a period of about 10 days (see Fig. 9 in Clinton et al., 2006). The measured change of the NS frequency was smaller (slightly less than 1%). Clinton et al. (2006) note that this increase in frequencies occurred in spite of the fact that strong winds that often accompany heavy rainfall tend to decrease the system frequencies by exciting larger amplitudes of response (by up to 3% in dry weather). Further, they note an increase of the system frequencies with temperature (about 1−2 % on very hot days with temperature near 40°C). For wind and temperature, the recovery is practically instantaneous, while for rainfall it is slow, and can take about a week.

3.6.2 Model Parameters for NS Response

Todorovska and Al Rjoub (2006b) chose the system parameters guided by the information provided in Luco et al. (1986), who specified: building weight = 1.05×10^{8} N, foundation weight = 0.14×10^{8} N, building height 44 m, foundation depth 4 m, and building in plan dimensions $21\,\mathrm{m}\times23\,\mathrm{m}$. Further, they classify the local soil as alluvium with depth to "bedrock" about 275 m, and mention apparent frequencies of vibration measured during forced vibration tests that are about $f_1 = 1.8$ Hz for NS vibrations, and $f_1 = 1.4$ Hz for EW vibrations. Clinton et al. (2005) provided further history on the variations of these frequencies, which shows strong correlation with amplitudes of response, and overall trend of decrease with time, from initial values $f_1 = 1.9$ Hz for NS vibrations, and $f_1 = 1.45$ Hz for EW vibrations during forced vibrations in 1967, to $f_1 = 1.54$ Hz for NS vibrations, and $f_1 = 1.19$ Hz for EW vibrations during ambient vibrations. For the soil in their homogeneous half-space model, Todorovska and Al Rjoub (2006b) chose values that would correspond approximately to the soil at Millikan Library near the surface. They use soil porosity $\hat{n}$ = 0.4, Poisson's ratio ν_s = 0.3, $\rho_{\mathrm{gr}} = 2.7\times10^{3}$ kg/m^3, and μ_s that correspond to dry shear wave velocity $V_{S,\mathrm{dry}} = \sqrt{\mu_s/[(1-\hat{n})\rho_{\mathrm{gr}}]}$ = 300 m/s. For the water, $\rho_f = 10^{3}$ kg/m^3 and $K_f = 2.2\times10^{9}$

Pa (which gives bulk wave velocity 1,483 m/s). For dry soil, they set $\rho_f / \rho_{\mathrm{gr}}$=0.001, and K_f / μ_s=0.001. These parameters imply K_f / μ_s= 15.089. For the building, they assumed fundamental *fixed-base* frequency $f_1 = 2.5\,\mathrm{Hz}$. Further, based on the foundation plan dimensions of $23.3\,\mathrm{m} \times 25.1\,\mathrm{m}$, they chose reference length a = 12 m. They also choose $b/a = 1$, i.e. a semi-circular. They noted that a rigid foundation model might be acceptable for the NS vibrations, for which experiments have shown that the base moves as a rigid body (Foutch et al., 1975), and as much as 30% of the roof response is due to rigid body rocking (Luco et al., 1986). In contrast, in the EW direction, the building behaves as one on a flexible foundation with a stiff central core (Foutch et al., 1975).

Table 3.6.2.1 shows the model wave velocities for dry and fully saturated soil with no seepage force. It can be seen that the saturated soil has slightly smaller shear wave velocity than the dry solid and more than 3 times larger velocity of the fast P-wave velocity.

Table 3.6.1 Wave velocities for fully saturated soil for the model of Millikan library assuming no seepage force

	K_f / μ_s	ρ_f / ρ_{gr}	V_S	V_{P1}	V_{P2}
Dry	0.001	0.001	300	561.3	175.6
Saturated	15.089	0.371	285.3	1,805.3	331.5

The variation of the wave velocities with permeability and degree of saturation is shown in Fig. 3.6.1 Part a) shows the variations of the normalized wave velocities versus inverse permeability at frequency $\eta = 1$ ($f = 12.5$ Hz). As in Section 3.1, the velocities are normalized by their values for zero seepage force. It can be seen that the wave velocities decrease for permeability smaller than 10^{-7}. Part b) shows variation of the velocities of the fast P-wave (when there is no seepage force) versus the amount fraction of air in the pores for different values of the pore pressure. It can be seen that both velocities decrease rapidly with increasing air content, with the velocity of the fast P-wave approaching the value for "dry" soil even for very small percentage of air such as 1%. This implies that to observe any significant changes in the system response due to rainfall, the level of saturation has to be very high.

a)

b)

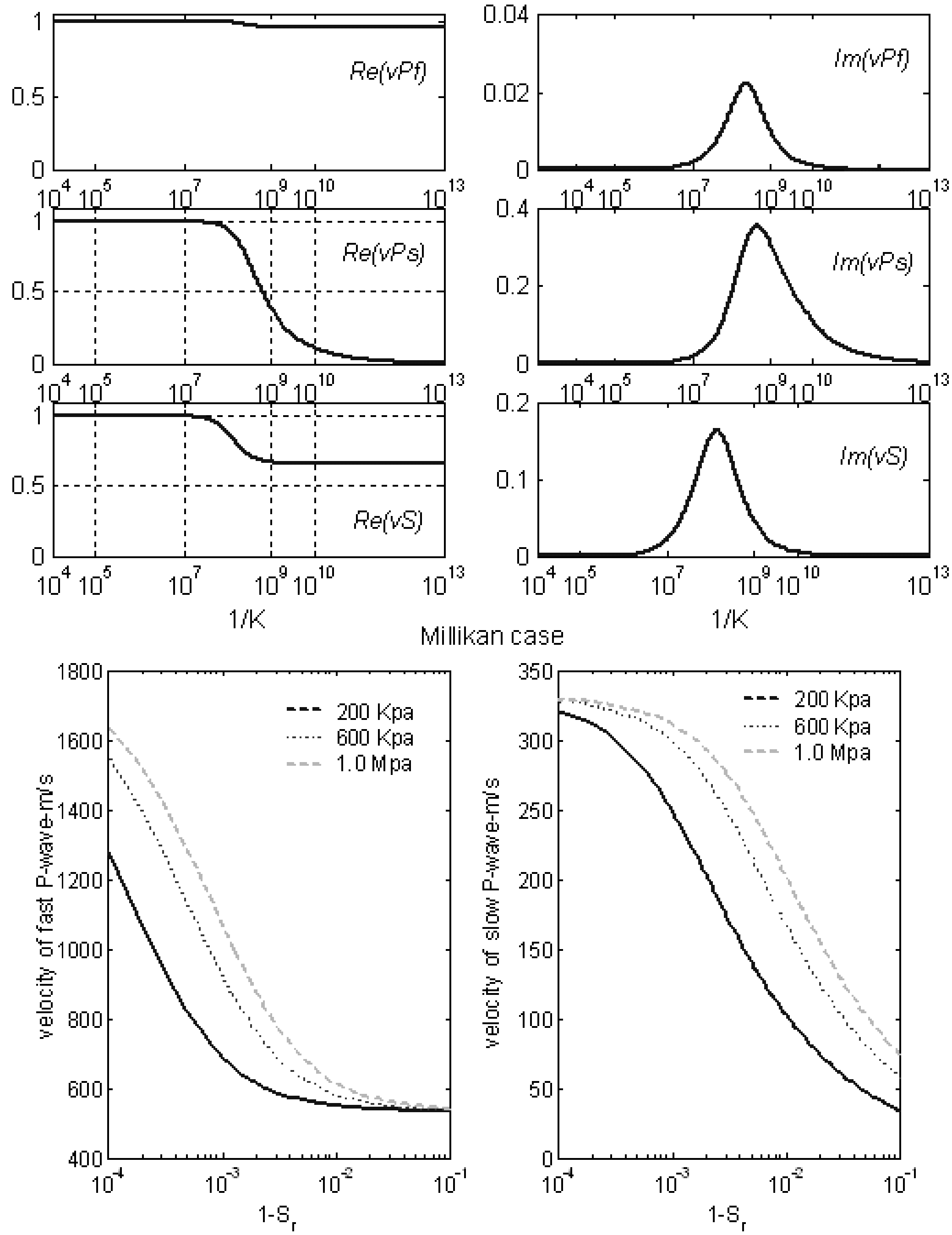

Fig. 3.6.1Wave velocities for the Millikan case. a) Normalized wave velocities for fully saturated soil as function of inverse permeability. b) Wave velocities of P-waves as function of the air content in the pores.

3.6.3 Foundation Complex Stiffness and System Response

Fig. 4.6.2 shows plots of the foundation complex stiffness matrix versus frequency between $f = 0$ and 60 Hz. Part a) shows results for a permeable foundation, and part b) for an impermeable foundation, and the real parts are shown of the left and the imaginary parts are shown on the right. The different types of lines correspond to dry soil and to fully saturated soil with different permeability. Similarly, Fig. 4.6.3 shows results of the system response (foundation translations, foundation rotation, and building relative response at the top), for vertically incident SV wave with unit displacement amplitude.

To help measure and understand the shifts of the first system frequency, enlarged plots of the horizontal/vertical stiffness coefficients and of the amplitudes of the first peak in the relative response are shown respectively in Figs. 3.6.4 and 3.6.5. Similarly as in the previous two figures, parts a) show results for a permeable foundation, and parts b) for an impermeable foundation. Figs. 3.6.4 shows that for small frequencies (i.e. near the frequency of the first mode of vibration of the building), the foundation stiffness is larger for saturated soil than for dry soil, and this effect is more significant for impermeable foundation. Also, it is larger for smaller permeability but only up to some value beyond which the effect reverses.

As it can be seen from Fig. 3.6.5, the shift in frequency for a permeable foundation is insignificant. For an impermeable foundation, Todorovska and Al Rjoub (2006b) reported increase of about by 2% (from 1.44 to 1.47 Hz) for fully saturated soil relative to dry, using their model which neglected the effects of the seepage force, which agreed

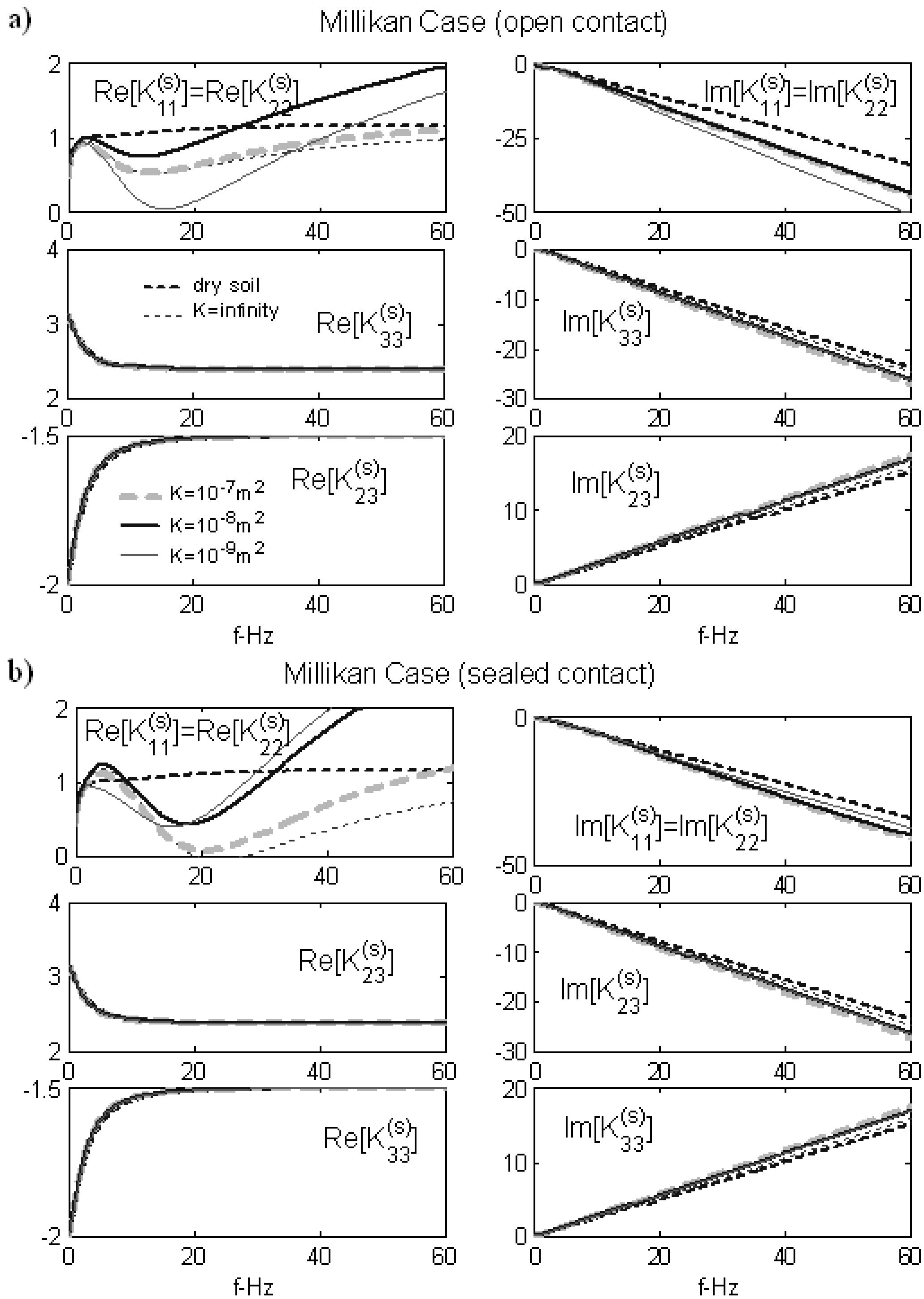

Fig. 3.6.2 Foundation complex stiffness matrix coefficients for the model corresponding to Millikan library. a) Permeable foundation. b) Impermeable foundation.

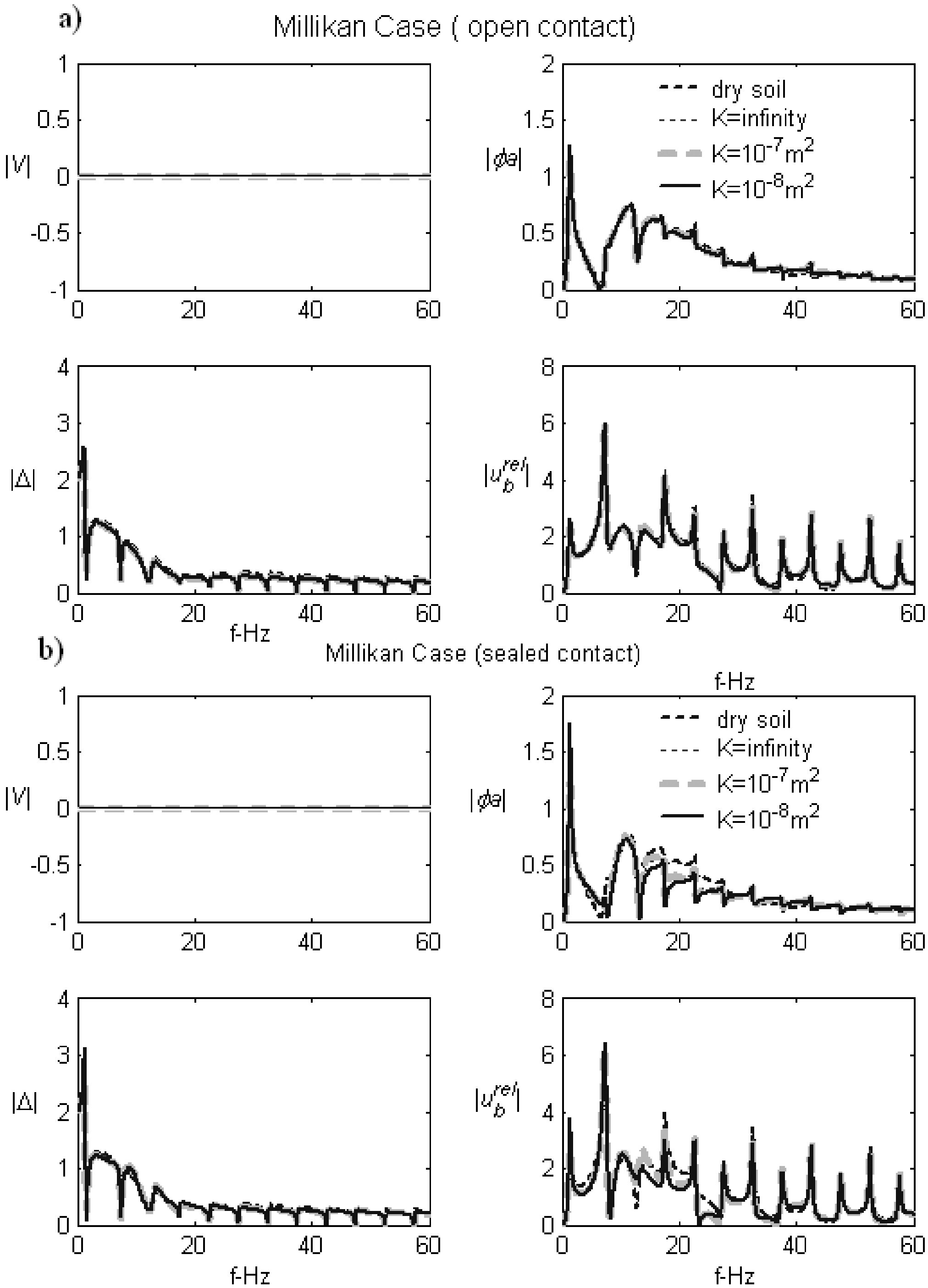

Fig. 3.6.3 System response for the model corresponding to Millikan library. a) Permeable foundation. b) Impermeable foundation.

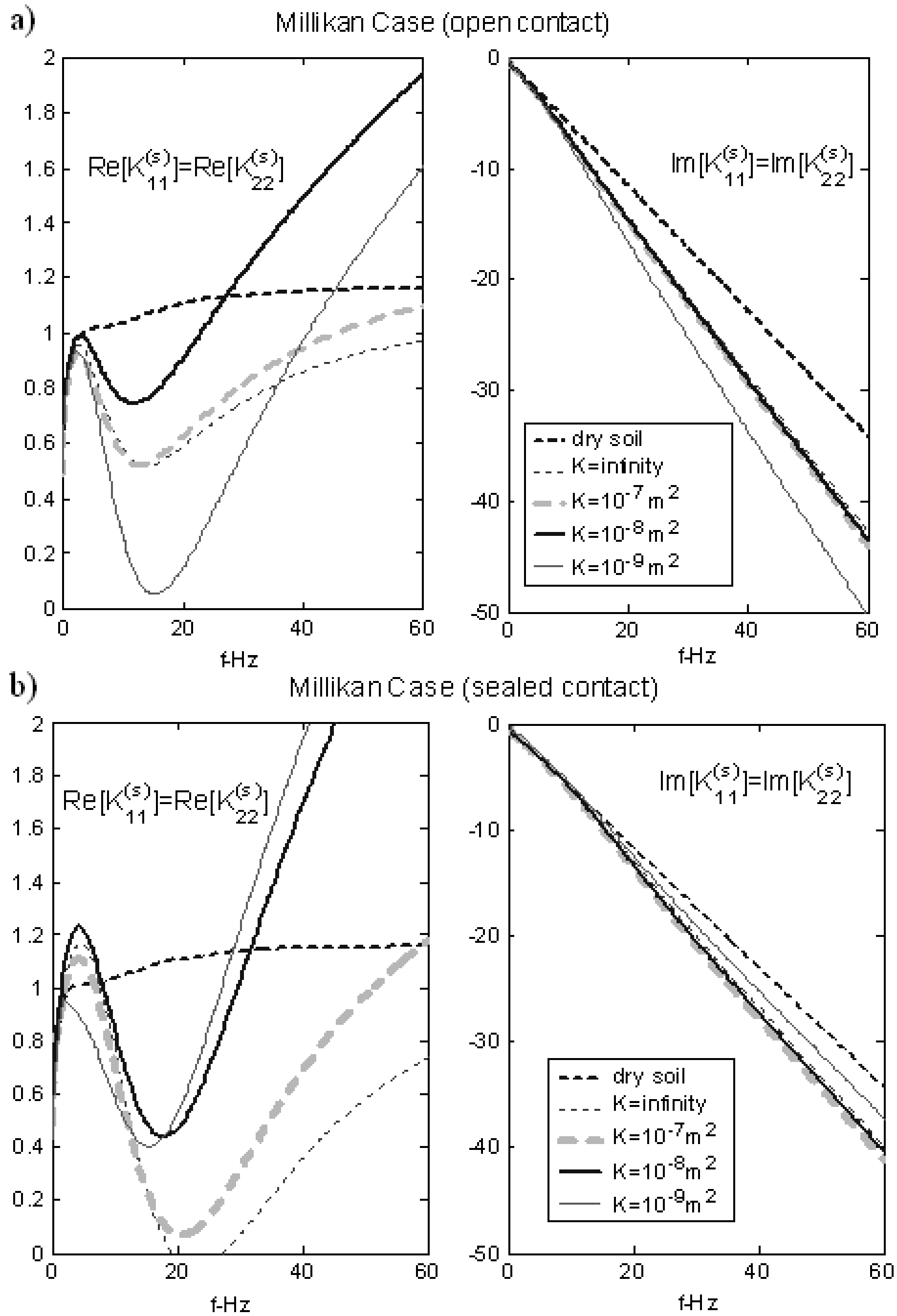

Fig. 3.6.4 Enlarged view of the horizontal/vertical foundation complex stiffness coefficients for the model corresponding to Millikan library. a) Permeable foundation. b) Impermeable foundation.

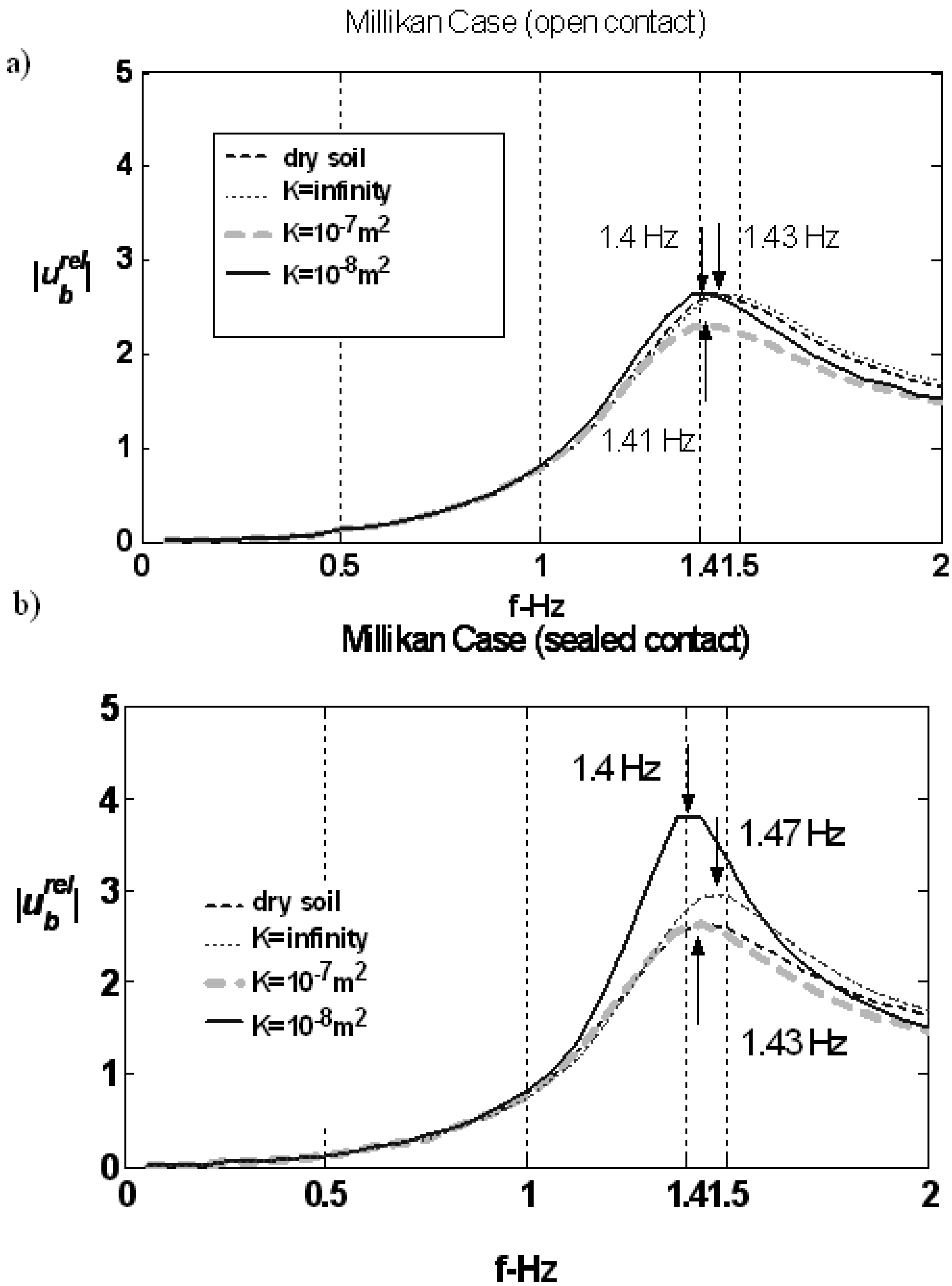

Fig. 3.6.5 Enlarged view of the first peak in the building relative roof response of the model corresponding to Millikan library. a) Permeable foundation. b) Impermeable foundation.

approximately with the observations. Fig. 3.6.5 (part b)) shows that this effect is smaller for less permeable soils and may reverse for small enough permeability of the soil.

It is noted here that the observed effect of finite permeability on the shift of frequency predicted by the model is due to the strong dependency of the wave velocities in Biot's original theory (Biot, 1956a) on permeability and frequency, i.e. for large enough $\frac{1}{\omega}\frac{\hat{n}\hat{\mu}}{\hat{k}}$. This dependency is most significant for the shear wave velocity, which can be reduces to up to 60-70% of its value for zero seepage force. This reduction is due to increased effective mass (due to the seepage force) in the computation of the wave velocities. It is also noted that Biot's theory does not consider the molecular forces between the different phases (solid, water and air in the case of partial saturation).

Chapter 4: Summary and Conclusions

This thesis presented an investigation of the effects of water saturation on the effective input motion and system response during building-foundation-soil interaction using a simple two-dimensional model. In this model, the building is represented as a shear wall supported by a semi-cylindrical foundation imbedded in a homogeneous and isotropic poroelastic half-space, and the excitation is a plane P, plane SV or a Rayleigh wave. Biot's theory of wave propagation in fully saturated poroelastic medium was used to describe the motion in the soil. By relaxing the zero stress condition at the free surface for the scattered waves, a closed form solution was derived using the wave function expansion method. The boundary conditions along the contact surface between the soil and the foundation are perfect bond for the skeleton, and either drained or undrained hydraulic condition for the fluid (i.e. permeable or impermeable boundary). The effect of partial saturation, versus full saturation for which the Biot's theory has been derived, is accounted for approximately, by changing the effective bulk modulus of the fluid.

Numerical results are shown for variations of the wave velocities, free-field motion amplitudes, foundation input motion amplitudes, foundation complex stiffness, and the system response in the frequency domain for different values of the model parameters, and for incident plane P- and SV-waves. Also, the effects of the saturation on the building apparent frequency are analyzed for a model that approximately corresponds to the NS response Millikan library in Pasadena, California, for which shift in frequency and recovery have been observed due to heavy rainfall. The numerical results were computed using a computer program written in Fortran. The following summarizes the results of the analysis and the conclusions.

The solution of the problem was expressed entirely in terms of dimensionless parameters, which were defined using reference: length a (half with of the foundation), material modulus μ_s (the shear modulus of the skeleton), and mass density ρ_{gr} (the density of the material of the grains without pores). The dimensionless parameters that control the system response are the following: stiffness of the skeleton relative to the bulk modulus of the fluid, through the ratio μ_s / K_f and the Poisson's ratio ν_s; mass density of the skeleton relative to the fluid, defined through the ratio $\rho_{\mathrm{gr}} / \rho_f$ and the porosity $\hat{n}$; mass of the building relative to the mass of the foundation, and mass of the foundation relative to the mass of the replaced soil, through the ratios $m_{\mathrm{b}} / m_{\mathrm{fnd}}$ and $m_{\mathrm{fnd}} / m_{\mathrm{gr}}$, where, $m_{\mathrm{gr}} = A_{\mathrm{fnd}} \rho_{\mathrm{gr}}$ is the mass of the excavated soil (per unit length) if there were no voids, and A_{fnd} is the area of the foundation; the flexibility of the building relative to that of the soil, through the ratio $\varepsilon = (V_{\mathrm{ref}} H)/(V_{S,\mathrm{b}} a) = \left[(\omega H)/V_{S,\mathrm{b}}\right] / \left[(\omega a)/V_{\mathrm{ref}}\right]$ = ratio of the number of wavelength in the shear beam in length H and the number of reference wavelengths in the soil in length a; dimensionless frequency $\eta = \omega a/(\pi V_{\mathrm{ref}})$, where $V_{\mathrm{ref}} = \sqrt{\mu_s / \rho_{\mathrm{gr}}}$ is a reference velocity; foundation shape, through the ratio h/a; and on the type, amplitude and angle of the incident waves. An additional parameter for viscous fluids and finite permeability is the coefficient of dissipation $\hat{b} = \hat{n}^2 \hat{\mu} / \hat{k}$, were $\hat{\mu}$ is the absolute viscosity, and $\hat{k}$ is the coefficient of permeability.

The wave velocities in the soil medium are the most fundamental quantities that affect the system response. Therefore, the effects of the model parameters on the wave velocities were first analyzed. Biot's theory predicts the existence of two P-waves (one fast and the other one slow) and one S-wave in poroelastic soil medium. The results show that, when the seepage force is considered, the velocities of these waves are frequency dependent. The wave velocities in the soil decrease with increasing seepage force, the effects of which are more pronounced for smaller frequency of motion, larger fluid viscosity, larger porosity and smaller skeleton permeability, i.e. for larger $\frac{1}{\omega}\frac{\hat{n}\hat{\mu}}{\hat{k}}$. For large enough $\frac{1}{\omega}\frac{\hat{n}\hat{\mu}}{\hat{k}}$, the velocities of the SV and fast P-wave approach their asymptotic value, which is real valued, and the velocity of the slow P-wave approaches zero. The variation is very small for the fast P-waves (about 5%), is about up to 40% for the S-wave, and is up to 100% for the slow P-wave. The percentage change depends very little on the relative stiffness of the skeleton (i.e. μ_s / K_f). Both P-wave velocities decrease with increasing air content in the pores. The velocity of the fast P-wave approaches the P-wave velocity of the dry soil, and that of the slow P-wave approaches zero.

The results show that the amplitudes of the free-field motion, which excites the structure, depend strongly on the angle of incidence, and also on the properties of the soil model: relative stiffness of the skeleton (i.e. μ_s / K_f), porosity and permeability (for given viscosity and Poisson's ratio), and are frequency dependent when $\frac{1}{\omega}\frac{\hat{n}\hat{\mu}}{\hat{k}}$ is not small. The effect of the water is more significant for mixtures with softer skeleton (i.e. smaller μ_s / K_f), e.g. soft soils, as compared to porous rock. For incident P-wave, the amplitudes of the horizontal motion at the surface are larger for dry soil than for saturated soil, but the amplitudes of the vertical motion are larger for saturated soil and impermeable boundary. For incident SV wave, the peak horizontal amplitude is also larger for dry soil, and but the vertical amplitudes are smaller regardless of the hydraulic boundary condition on the surface.

The amplitudes of the free-field displacements at the ground surface depend most on the incident angle. For incident P waves, the amplitude of the horizontal displacement is zero for vertically and horizontally incident waves, and is the largest near 45 degrees incidence. The amplitudes of the vertical displacement is the maximum for vertical incidence, and it decreases monotonically to zero for horizontal incidence. For incident SV waves and Poison ratio $\nu = 0.3$, the horizontal amplitude equals 2 for vertical incidence, is zero at 45 degrees incidence, exhibiting a sharp peak for incidence below 45 degrees, beyond which it increases a little and decreases again to zero for horizontal incidence. The amplitudes for the vertical motion are zero for vertical and horizontal incidence, and exhibit a peak near 30 degrees incidence. The frequency dependence is more significant for incident SV waves, but it is still small. The amplitudes decrease with increasing frequency, approaching those for zero seepage force.

The foundation input motion is the effective input motion exciting the structure. It is defined as the response of a massless foundation, without the structure, to the incident waves, and represents the free field motion that has been modified by the scattering of waves from the foundation. As the dimensionless frequency $\eta \to 0$ (i.e. for very long incident waves compared to the size of the foundation), the horizontal and vertical amplitudes of the foundation input motion approach those of the free-field motion, and the rotation approaches zero. For very short incident wavelengths, the amplitudes approach zero, due to the ironing effect of the foundation.

The building response is affected by the dynamic soil-structure interaction through the foundation complex stiffness matrix. The real part of this matrix is referred to as "foundation stiffness", and the imaginary part is related to the loss of energy due to radiation which effect is related to the "radiation damping". The results show that the presence of water in the pores affects significantly the foundation impedance matrix for soft and stiff soils. The rocking impedance is affected negligibly by the presence of water, which can be explained by the fact that the rocking motions produce mostly a shearing deformation of the soil near the contact surface. The conclusion is similar for the coupling term. The horizontal impedance is significantly affected by the hydraulic condition along the contact surface, which permits or stops the flow of water through the contact surface. As it can be expected, the foundation stiffness is larger when the pores are filled with water and the contact surface is impermeable (sealed contact). The imaginary part, however, i.e. the radiation damping, is larger for permeable foundation. For relatively small seepage force, the foundation stiffness increases with increasing seepage force, but for large enough seepage force the effect becomes the opposite. In that case, the decreasing foundation stiffness with increasing seepage force can be explained by the smaller wave velocities for larger seepage force.

For the case corresponding to NS response of Millikan library, the apparent frequency increases by about 2% for fully saturated soil, impermeable foundation, and negligible seepage force (very high permeability). For decreasing permeability, however, the increase becomes smaller and the trend reverses for small enough permeability. Because of this, and the fact that the wave velocities as well as foundation stiffness are strongly dependent on frequency, conclusions from analysis of one model or particular observation for a specific soil site and structure cannot be automatically generalized to any structure and type of soil.

References

[1] Berryman JG (1980). Confirmation of Biot's theory, Appl. Physics Letter, 34(4), 382-384.

[2] Biot MA (1956a). Theory of propagation of elastic waves in a fluid-saturated porous solid: I low-frequency range, J. of Acoustical Society of America, 28(2), 168-178.

[3] Biot MA (1956b). Theory of propagation of elastic waves in a fluid-saturated porous solid: II higher-frequency range, J. of Acoustical Society of America, 28(2), 179-191.

[4] Biot MA (1962). Mechanics of deformation and acoustic propagation in porous media, J. of Applied Physics, 33(4), 1482-1498.

[5] Biot MA, Willis DG (1957). The elastic coefficients of a theory of consolidation", Journal of Applied Mechanics, ASME, 29**,** 594-601.

[6] Bo J, Hua L (1999). Vertical dynamic response of a disk on a saturated poroelastic half-space, Soil Dynamics and Earthquake Engineering, 18, 437–443.

[7] Bougacha S, Tassoulas JL (1991a). Seismic analysis of gravity dams. I: modeling of sediments, J. of Engineering Mechanics, ASCE, 117(8), 1826-1837.

[8] Bougacha S, Tassoulas JL (1991b). Seismic response of gravity dams. II: effects of sediments, J. of Engineering Mechanics, ASCE, 117(8), 1839-1850.

[9] Bougacha S, Tassoulas JL, Roesset JM (1993a). Analysis of foundations on fluid-filled poroelastic stratum**,** J. of Engineering Mechanics, ASCE, 119(8), 1632-1648.

[10] Bougacha S, Roesset JM, Tassoulas JL (1993b). Dynamic stiffness of foundations on fluid filled poroelastic stratum, J. of Engineering Mechanics, ASCE, 119(8), 1649-1662.

[11] Carcione JM, Cavallini F, Santos JE, Ravazzoli CL, Gauzellino PM (2004). Wave propagation in partially saturated porous media: simulation of a second slow wave, Wave Motion, 39(3), 227-240.

[12] Ciarletta M, Sumbatyan MA (2003). Reflection of plane waves by the free boundary of a porous elastic half-space, J. of Sound and Vibration, 259(2), 253-264.

[13] Clinton JF, Bradford SK, Heaton TH, Favela J (2006). The observed wander of the natural frequencies in a structure, Bull. Seismological Society of America, 96 (1), 237-257.

[14] Dargush GF, Chopra MB (1996). Dynamic analysis of axisymmetric foundations on poroelastic media, J. of Engineering Mechanics, ASCE, 122(7), 623-632.

[15] Degrande G, De Roeck G, Broeck PVD, Smeulders D (1998). Wave propagation in layered dry, saturated and unsaturated poroelastic media, Int.l J. of Solids and Structures, 35(34-35), 4753-4778.

[16] Deresiewicz H (1960). The effect of boundaries on wave propagation in a liquid-filled porous solid: I. reflection of plane waves at a free plane boundary (non-dissipative case), Bull. Seismological Society of America, 50(4), 599-607.

[17] Deresiewicz H (1961). The effect of boundaries on wave propagation in a liquid-filled porous solid: II. Love waves in a porous layer, Bull. Seismological Society of America, 51(1), 51-59.

[18] Deresiewicz H, Rice JT (1962). The effect of boundaries on wave propagation in a liquid-filled porous solid: III. Reflection of plane waves at a free plane boundary (general case), Bull. Seismological Society of America, 52(3), 595-625.

[19] Edelman I (2004a). On the existence of the low-frequency surface waves in a porous medium, Comptes Rendus Mecanique, 332(1), 43-49.

[20] Edelman I (2004b). Surface waves at vacuum/porous medium interface: low frequency range, Wave Motion, 39(2), 111-127.

[21] Halpern MR, Christiano P (1986). Steady-state harmonic response of a rigid plate bearing on a liquid-saturated poroelastic half space, Earthquake Engineering and Structural Dynamics, 14, 439-454.

[22] Japon BR, Gallego R, Dominguez J (1997). Dynamic stiffness of foundations on saturated poroelastic soils, J. Engineering Mechanics, ASCE, 123(11), 1121-1129.

[23] Jin B, Liu H (2000a). Horizontal vibrations of a disk on a poroelastic half-space, Soil Dynamics and Earthquake Engineering, 19, 269–275

[24] Jin B, Liu H (2000b). Rocking vibrations of rigid disk on saturated poroelastic medium, Soil Dynamics and Earthquake Engineering, 19, 469-472.

[25] Jinting W, Chuhan Z, Feng J (2004). Analytical solutions for dynamic pressures of coupling fluid-solid-porous medium due to P wave incidence, Earthquake Engineering and Engineering Vibration, 3(2), 263-273.

[26] Kassir MK, Xu JM (1988). Interaction functions of a rigid strip bonded to saturated elastic half-space, Int. J. of Solids and Structures, 24(9), 915-936.

[27] Kassir MK, Bandyopadhyay KK, Xu J (1989). Vertical vibration of a circular footing on a saturated half-space, Int. J. Engineering Science, 27(4), 353-361.

[28] Kassir MK, Xu J, Bandyopadyay KK (1996). Rotary and horizontal vibrations of a circular surface footing on a saturated elastic half-space, Int. J. of Solids and Structures, 33(2), 265-281.

[29] Lin C-H, Lee VW, Trifunac MD (2001). On the reflection of elastic waves in a poroelastic half-space saturated with non-viscous fluid. Report CE 01-04, Dept. of Civil Eng, Univ. of Southern California.

[30] Lin C-H, Lee VW, Trifunac MD (2005). The reflection of plane waves in a poroelastic half-space saturated with inviscid fluid, Soil Dynamics and Earthquake Engineering, 25, 205–223.

[31] Liu K, Liu Y (2004). Propagation characteristic of Rayleigh waves in orthotropic fluid-saturated porous media, Journal of Sound and Vibration, 271(1-2), 1-13.

[32] Liu Y, Liu K, Tanimura S (2002). Wave propagation in tansversley isotropic fluid-saturated poroelastic media, JSME International Journal, Series A, 45(3), 348-355.

[33] Liu Y, Liu K, Gao L, Yu TX (2005). Characteristic analysis of wave propagation in anisotropic fluid-saturated porous media, Journal of Sound and Vibration, 282(3-5), 863-880.

[34] Luco JE (1969). Dynamic interaction of a shear wall with the soil, J. Engineering mechanics, ASCE, **95**:333-346.

[35] Philippacopoulos AJ (1989). Axisymmetric vibration of disk resting on saturated layered half space. J. Eng. Mech. Div. ASCE, 115(10), 2301-2322.

[36] Rajapakse RKND, Senjuntichai T (1995). Dynamic response of a multi-layered poroelastic medium, Earthquake Engineering and Structural Dynamics, 24, 703-722.

[37] Senjuntichai T, Mani S, Rajapakse RKND (2006). Vertical vibration of an embedded rigid foundation in a poroelastic soil, Soil Dynamics and Earthquake Engineering, 26, (Special issue on Biot Centennial – Earthquake Engineering).

[38] Sharma MD, Gogna ML (1991). Seismic wave propagation in a viscoelastic porous solid saturated by viscous liquid, Pure and Applied Geophysics, 35(3), 383-400.

[39] Sharma MD (2004). 3-D Wave Propagation in a general anisotropic poroelastic medium: reflection and refraction at an interface with fluid, Geophysics J. Int. 157, 947-958.

[40] Todorovska MI, Trifunac MD (1990). Analytical Model for in Plane Building-Foundation-Soil Interaction: Incident P-, SV- and Raleigh Waves, Report No. 90-01, Dept. of Civil Engrg, Univ. of Southern California. pp.122.

[41] Todorovska MI (1993a). Effects of the wave passage and the embedment depth during building-soil interaction, *Soil Dynamics and Earthquake Engineering* 12(6):343-355.

[42] Todorovska MI (1993b). In-plane foundation-soil interaction for embedded circular foundations, *Soil Dynamics and Earthquake Engineering* 12(5):283-297.

[43] Todorovska, M.I. & Y. Al Rjoub (2006a). Effects of rainfall on soil-structure system frequency: examples based on poroelasticity and a comparison with full-scale measurements, Soil Dynamics and Earthquake Engrg, 26(6-7), 708-717. (Special issue on Biot Centennial – Earthquake Engineering).

[44] Todorovska, M.I. & Y. Al Rjoub (2006b). Plain strain soil-structure interaction model for a building supported by a circular foundation embedded in a poroelastic half-space, Soil Dynamics and Earthquake Engrg, 26(6-7), 694-707. (Special issue on Biot Centennial – Earthquake Engineering).

[45] Trifunac MD (1972). Interaction of a shear wall with the soil for incident plane SH-waves. Bull. Seismological Society America, 62, 63-83.

[46] Vashishth K, Khurana P (2004). Waves in stratified anisotropic poroelastic media: a transfer matrix approach, J. Sound and Vibration, 277(1-2), 239-275.

[47] Wong HL, Trifunac MD (1974). Interaction of shear wall with the soil for incident plane SH waves: elliptical rigid foundation, Bulletin of Seismological Society of America, 64, 1825-1842.

[48] Yang J (1999). Importance of flow condition on seismic waves at a saturated porous solid boundary, Journal of Sound and Vibration, 221(2), 391-413.

[49] Yang J (2000). Influence of water saturation on horizontal and vertical motion at a porous soil interface induced by incident P wave, Soil Dynamics and Earthquake Engineering, 19(8), 575–581.

[50] Yang J (2001). Saturation effects on horizontal and vertical motions in a layered soil–bedrock system due to inclined SV waves, Soil Dynamics and Earthquake Engineering, 21(6), 527–536.

[51] Yang J (2002). Saturation effects of soils on ground motion at free surface due to incident SV waves, Journal of Engineering Mechanics, 128(12), 1295-1303.

[52] Yang J and Sato T. (1998). Influence of viscous coupling on seismic reflection and transmission in saturated porous media, Bulletin of the Seismological Society of America, 88 (5), 1289-1299.

[53] Yang J and Sato T. (2000a). Effects of Pore-Water Saturation on Seismic Reflection and Transmission from a Boundary of Porous Soils, Bulletin of the Seismological Society of America, 90 (5), 1313-1317.

[54] Yang J and Sato T. (2000b). Influence of water saturation on horizontal and vertical motion at a porous soil interface induced by incident SV wave, Soil Dynamics and Earthquake Engineering, 19(5), 339–346.

[55] Yang J and Sato T. (2000c). Interpretation of Seismic Vertical Amplification Observed at an Array Site, Bulletin of the Seismological Society of America, 90 (2), 275-285.

[56] Zeng X, Rajapakse RKND. (1999). Vertical vibrations of a rigid disk embedded in a poroelastic medium. Int. J. Numerical and Analytical Methods in Geomechanics, 23, 2075-2095.

Appendix

$$I_1(n) = \int_{-\theta_0}^{\theta_0} \cos\theta_1 \cos n\theta_1 d\theta_1 = \begin{cases} \dfrac{\sin(n+1)\theta_0}{n+1} + \dfrac{\sin(n-1)\theta_0}{n-1}, \ldots\ldots n \neq 1 \\ \dfrac{\sin 2\theta_0}{2} + \theta_0, \ldots\ldots\ldots\ldots\ldots\ldots\ldots\ldots\ldots n = 1 \end{cases} \tag{1}$$

$$I_4(n) = \int_{-\theta_0}^{\theta_0} \sin\theta_1 \sin n\theta_1 d\theta_1 = \begin{cases} \dfrac{-\sin(n+1)\theta_0}{n+1} + \dfrac{\sin(n-1)\theta_0}{n-1}, \ldots\ldots n \neq 1 \\ \dfrac{-\sin 2\theta_0}{2} + \theta_0, \ldots\ldots\ldots\ldots\ldots\ldots\ldots\ldots\ldots n = 1 \end{cases} \tag{2}$$

$$I_5(n) = \int_{-\theta_0}^{\theta_0} \cos n\theta_1 d\theta_1 = \begin{cases} \dfrac{2\sin n\theta_0}{n}, \ldots\ldots\ldots\ldots\ldots\ldots n \neq 1 \\ 2\theta_0, \ldots\ldots\ldots\ldots\ldots\ldots\ldots\ldots\ldots n = 0 \end{cases} \tag{3}$$